Computational Models of the Heart for Planning and Treatment of Outflow Tract Ventricular Arrhythmias

Rubén Doste Beltrán

DOCTORAL THESIS UPF / 2019

Directors of the thesis

Dr. Oscar Camara and Dr. Rafael Sebastian
Department of Information and Communication Technologies

Directors

Dr. Oscar Camara	Associate Professor Universitat Pompeu Fabra Barcelona, Spain
Dr. Rafael Sebastian	Associate Professor Universitat de Valencia Valencia, Spain

Review Committee (Main):

Jose Maria Ferrero de Loma Osorio	Universidad Politecnica de Valencia
Esther Pueyo Paules	Universidad de Zaragoza
Hermenegild Arevalo	Simula Research Lab

Review Committee (Reserve):

Bart Bijnens	Universitat Pompeu Fabra
Jazmin Aguado Sierra	Barcelona Supercomputing Center

This work was carried out in the research group *Sensing in Physiology and Biomedicine (PhySense)*, at the Departament de Tecnologies de la Informació i les Comunicacions at the Universitat Pompeu Fabra, Barcelona, Spain. This thesis was supported by a scholarship from the Department of Information and Communication Technologies at Universitat Pompeu Fabra (DTIC-UPF).

Abstract / Resumen

Abstract Nowadays, cardiac arrhythmias are among the leading causes of mortality in the world and impose a huge healthcare burden on society. Ventricular tachy-arrhythmias are responsible for 80% of the 350 000 sudden cardiac deaths occurring each year in Europe. Over the last years, new technologies are facilitating the patient-specific management of cardiac arrhythmias such as high resolution clinical imaging (MRI, CT) that allows to characterize the heart substrate in pathological regions; electro-anatomical mapping (EAM), that provides invasive electrical information of the patient's heart and enables real-time intracardiac navigation using catheters; or radiofrequency ablation (RFA), which allows to eliminate pathological tissue in the heart that is triggering or sustaining an arrhythmia.

However, due to the complexity of the disease, long-term treatment success rates remain low (success rates in the range of 60 to 65%), even though well-developed clinical guidelines for management of ventricular tachycardia have been developed. Therefore, there is a compelling need to improve clinical outcomes for the benefit of the patients and the healthcare system.

Computational models that reproduce the heart electrical behaviour have proved to be a valuable instrument for better understanding the biophysics of cardiac electrophysiology, and have the potential to improve patient management, therapy planning and delivery. Those models permit to integrate disparate information from several clinical sources (MRI, EAM, ECGs) into a single reference system to build a patient-specific model, that combined with multi-scale biophysical models of the heart can produce realistic simulations of cardiac electrophysiology from cell to body level.

To date, computer-based personalised approaches have not penetrated into clinical practice, which can be attributed to several reasons. One of the major drawbacks that have prevented simulation-based technology to reach

clinical environments has been the complexity inherent in the patient-specific model building, which requires expertise in several areas such as imaging, mathematics or computer science. In addition, running detailed simulations of the heart is computationally demanding, and usually needs high performance computing facilities. To overcome these limitations while integrating all possible afore-mentioned imaging and signal information, we propose to use advanced biophysical models and disparate clinical data as training tools that can be used as an input to artificial intelligence systems. In that way simulations can be carried out by engineers, off-line in specialized facilities, with the supervision of medical doctors that have to check their accuracy. This novel approach can take into account a large variety of scenarios, that can help decision support systems to provide recommendations on therapy planning of interventions such as RFA.

The main purpose of this thesis was to develop personalised cardiovascular therapy guided by multimodal noninvasive imaging and simulations combined with artificial intelligence tools for the management of idiopathic ventricular tachycardias with origin in the ventricular outflow tracts. In summary, the main contributions of this thesis are twofold:

- Pipeline for the simulation of cardiac arrhythmias: we propose a pipeline to build computational models of the heart for simulation of ventricular tachycardias, that incorporates a new specific rule-base method to calculate the myocardial fiber orientation of the ventricles. This method includes specific fiber orientation of the right ventricle, the inter-ventricular septum and both outflow tracts. The pipeline allows to carry out simulations from cell to body level, and therefore obtain the virtual ECG of each patient for different scenarios. In addition, the methodology permits to perform *in silico* pace mapping in patient-specific models in order to train machine learning based tools.

- System for predicting the site of origin of ventricular tachycardias: we have developed a tool to exploit the results from *in silico* pace mapping in the ventricles in two different ways. First, we can analyse the patient's ECG pre-operatively and compare it with the results of our simulated data to analyse the most probable site of origin of the tachycardia. In cases in which we do not have imaging data from the patient, we classify the patient ECG by machine learning techniques to predict the site of origin. The artificial intelligence models are trained with all the previous available information which are mainly simulations, but also previous clinical data from interventions.

Resumen Las arritmias cardíacas son unas de las principales causas de mortalidad en el mundo y suponen un reto para el sistema sanitario actual. Particularmente, las taquicardias ventriculares son responsables del 80% de los 350000 casos de muerte súbita que se registran cada año en Europa. En los últimos años el tratamiento de las arritmias se ha visto facilitado con la aparición de nuevas tecnologías que usan datos específicos del paciente como pueden ser las imágenes clínicas de alta resolución (MRI,CT) que nos permiten caracterizar el sustrato en regiones patológicas; los mapas electro-anatómicos (EAM), que proporcionan información sobre la activación eléctrica obtenida de manera invasiva y permiten la navegacíon intracardíaca usando catéteres o la ablación por radiofrecuencia (RFA) que nos permite eliminar el sustrato patológico del corazón que desencadena o mantiene la arritmia. Sin embargo, debido a la complejidad de la enfermedad, las tasas de éxito del tratamiento a largo plazo siguen siendo bajas (tasas de éxito en el rango de 60 a 65 %), a pesar del desarrollo de guías clínicas detalladas para el tratamiento de la taquicardia ventricular. Por lo tanto, existe una alta necesidad de mejorar los resultados clínicos en beneficio de los pacientes y el sistema sanitario.

Los modelos computacionales de electrofisiología cardíaca han demostrado ser una herramienta útil para comprender mejor los principios biofísicos de la electrofisiología cardíaca y tienen el potencial de mejorar el manejo del paciente y la planificación y optimización de la terapia. Estos modelos permiten integrar información diversa de varias fuentes clínicas (MRI, EAM, ECG) en un solo sistema de referencia para construir un modelo específico para el paciente, que combinado con modelos biofísicos del corazón a múltiples escalas permiten realizar simulaciones realistas de la electrofisiología cardíaca teniendo en cuenta la fisiología desde el nivel celular a nivel de órgano y cuerpo completo.

Hasta la fecha, los enfoques basados en modelos personalizados basados por computador no han penetrado en la práctica clínica, lo cual puede atribuirse a varias razones. Uno de los principales inconvenientes que ha impedido que la tecnología basada en simulación llegue a entornos clínicos ha sido la complejidad inherente a la construcción de modelos específicos del paciente, que requiere experiencia en varias áreas de conocimiento, como la imagen médica, las matemáticas o la informática. Además, ejecutar simulaciones detalladas del corazón es computacionalmente costoso y, por lo general, requiere instalaciones informáticas de alto rendimiento. Para superar estas limitaciones e integrar todas las posibles modalidades de imágenes e información de señales mencionadas anteriormente, proponemos utilizar modelos

biofísicos avanzados y datos clínicos multimodales como datos de entrada en sistemas de inteligencia artificial. De este modo, los ingenieros pueden realizar simulaciones en instalaciones especializadas, con la supervisión de médicos que deben verificar su precisión y desempeño. Este novedoso enfoque tiene en cuenta una gran variedad de escenarios, que pueden servir para ayudar a los sistemas de apoyo a la decisión a proporcionar recomendaciones sobre la planificación del tratamiento de distintas intervenciones como la ablación por radiofrecuencia.

El objetivo principal de esta tesis es desarrollar una terapia cardiovascular personalizada guiada por información multimodal no invasiva y simulaciones, combinadas con herramientas de inteligencia artificial, para el manejo de taquicardias ventriculares idiopáticas originadas en los tractos de salida del ventrículo. En resumen, las principales contribuciones de esta tesis son dos:

- Un flujo de trabajo para la simulación de arritmias cardíacas: proponemos un procedimiento para construir modelos computacionales del corazón con el fin de simular taquicardias ventriculares, que incluye un nuevo modelo específico (basado en reglas) para calcular la orientación de fibras en el miocardio y en los tractos de salida de los ventrículos. Este flujo de trabajo permite realizar simulaciones desde la escala celular hasta la escala de cuerpo completo y, por lo tanto, obtener el ECG virtual de cada paciente en diferentes escenarios. Además, la metodología permite realizar mapas de estimulación *in silico* en modelos cardíacos personalizados a paciente para poder entrenar herramientas basadas en aprendizaje automático.

- Un sistema para predecir el lugar de origen de las taquicardias ventriculares: hemos desarrollado una herramienta para explotar los resultados de los mapas de estimulación *in silico* en los ventrículos de dos maneras diferentes. Primero, analizando el ECG del paciente antes de la operación y comparándolo con los resultados de nuestros datos simulados para estudiar el sitio de origen más probable de la taquicardia. En los casos en los que no tenemos datos de imágenes del paciente, clasificamos el ECG del paciente mediante técnicas de aprendizaje automático para predecir el sitio de origen. Los modelos de inteligencia artificial están entrenados con toda la información previa disponible, que son principalmente ECGs simulados, pero también datos clínicos previos de las intervenciones.

Preface

This thesis would not have been possible without the encouragement and support received from many people. First, I would like to thank my supervisors Oscar Camara and Rafael Sebastian. I am very thankful to Oscar, for giving me the opportunity of joining PhySense and for his trust and advice during all this process. I also would like to express my deepest gratitude to Rafael Sebastian for his constant guidance throughout this thesis and for giving me the chance to be part of his research group during my stay in Universitat de Valencia.

Thanks to all the people I had a chance to closely work with, especially to my colleagues from Physense and SIMBIOsys research groups. Thank you for your support and for all the good moments.

Thanks to the colleagues from Universitat de Valencia for making my stay such a wonderful and productive experience, especially to Miguel Lozano, whose ideas and help were very valuable.

I am grateful to Maxime Sermesant for giving me the opportunity to visit his research group at Inria. I also would like to express my gratitude to all the people I have worked with from the Barcelona Supercomputer Center.

I would like to thank Damian Sanchez Quintana, for sharing his knowledge and wisdom about the heart anatomy. It was a pleasure to work with him. I am also very grateful to Dr. Antonio Berruezo and Dr. Diego Penela for all the discussions that have enriched the clinical aspects of my research.

I sincerely thank all my family for their endless love support and influence in my life. Thank you for believing in me.

Finally, I would like to thank Carola for her unconditional help during this time that has been extremely important to me. I would have never gotten this far without your support and love.

Contents

List of Figures

List of Tables

Acronyms

AF	Atrial fibrillation
AMC	Aorto-mitral continuity
APD	Action potential duration
AV	Aortic valve
BSPM	Body surface potential map
CCS	Cardiac conduction system
CNN	Convolutional neural network
CT	Computed tomography
DL	Deep learning
DT-MRI	Diffusion tensor magnetic resonance imaging
EAM	Electroanatomical mapping
ECG	Electrocardiogram
k-NN	k-nearest neighbors
LA	Left atria
LAT	Local activation time
LCAS	Left coronary aortic sinus
LCC	Left coronary cusp
LV	Left ventricle
LVOT	Left ventricular outflow tract
MKL	Multiple kernel learning
ML	Machine learning
MRI	Magnetic resonance imaging
NCAS	Non coronary aortic sinus
NCC	Non coronary cusp
OT	Outflow tract
OTVA	Outflow tract ventricular arrhythmia

PV	Pulmonary valve
PVC	Premature ventricular contractions
QE	Quantization error
RBM	Rule-based method
RCAS	Right coronary aortic sinus
RCC	Right coronary cusp
RF	Random forest
RFA	Radiofrequency ablation
RV	Right ventricle
RVOT	Right ventricular outflow tract
SOM	Self organizing maps
SOO	Site of origin
SVM	Support vector machine
VT	Ventricular tachycardia

1

Introduction

1.1 The heart

1.1.1 Anatomy and function

The heart is a muscular organ located in the central region of the thorax, in the middle and lower mediastinum, between the two lungs. The primary function of the heart is to pump a continuous flow of blood through the blood vessels to provide the body with oxygen and nutrients. The pump rate is determined by the pacemaking cells located at the sinoatrial node, that generate autonomously the initial impulse that travels at fast speeds across the cardiac conduction system. From there the electrical impulse spreads through the heart triggering and coordinating the contraction of the cardiac cells that pump blood to the body. The heart is a complex organ in which three main different physics interact: electrophysiology, mechanics and hemodynamics. Any alteration of those physics that hampers the pumping efficiency of the heart will have large negative effects for the whole body, which eventually can lead to death.

As depicted in Figure 1.1, the heart is divided into four chambers or cavities: two superior, called the right atrium (RA) and left atrium (LA); and two lower, called right ventricle (RV) and left ventricle (LV). The atria receive blood from the venous system and transfer it to the ventricles, from where it is propelled into the arterial circulation.

The RA and the RV form the right heart. The RA receives the blood that comes from the entire body through the superior vena cava and inferior vena cava. The RV drives non-oxygenated blood into the lungs through the pulmonary artery. The LA and the LV form the left heart, that receive oxygenated blood from the lungs that flows through the four pulmonary veins in the left atrium. The LV drives oxygenated blood through the aortic artery to distribute throughout the body.

The ventricles present a more regular and simpler morphology than the atria in general terms. The RV anatomy is considerable different from that of the LV, although both ventricles share the same pumping principles. The LV has the shape of a cone with the RV hugging it. The wall that separates the ventricles is called the interventricular septum, while the wall opposing the septum is the so-called lateral or free wall. The lowest area of the ventricles is named the apex, and the area that is in contact to the atria is the base. When the heart is viewed from the anterior view, most of the LV is hidden by the RV. The atria and the ventricles are separated by the atrioventricular

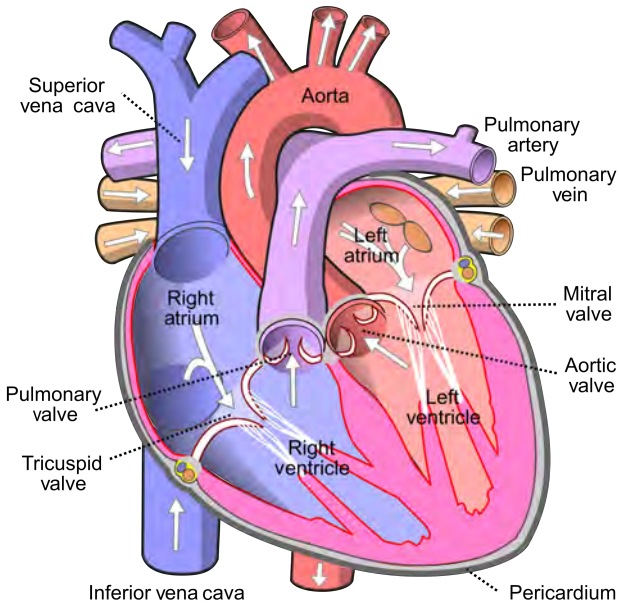

Figure 1.1: Schematic representation of the heart anatomy that shows the valves, arteries and veins distribution. The white arrows represent the normal direction of blood flow. Source: https://commons.wikimedia.org/

septum, which is formed by fibrous rings that serve as bases for the four heart valves. Valves are passive structures that prevent the circulation of blood in the opposite direction. There are four main valves in the human heart. Two atrioventricular valves that connect the atria and ventricles (mitral valve in the LV and tricuspid valve in the RV) and two semilunar valves that connect the ventricles with the arteries (aortic valve in the LV and pulmonary valve in the RV).

The RV can be divided into three anatomically different components: an inflow tract, which extends from the atrioventricular junction to the insertion in the ventricular wall of the papillary muscles of the tricuspid valve; an apical component, which occupies the region of the apex; and finally, an outflow tract, also called pulmonary infundibulum or arterial cone, which extends up to the pulmonary trunk. The RV is characterized by an irregular endocardium with abundant trabeculae carneae. Trabeculae carneae are irregular muscular tissue blocks with tubular shape which project from the ventricular inner surfaces. The trabeculae, together with the grooves that exist between them, provide a great variability to the wall thickness of

the RV, which usually ranges between 3 and 5 mm. Other muscular protuberance existing on the walls of the RV are the papillary muscles, which are inserted at one end into the ventricular wall and continue with the so-called chordae tendineae, which are cordons of connective tissue that are inserted into the veils of the triscupid valve. A protrusion especially prominent present in the RV is the septomarginal trabecula, a muscle that has a body that divides into anterior and posterior branches. One of them is the anterior papillary muscle, and the other crosses the ventricular cavity, forming the moderator band.

The RV outflow tract (RVOT) or infundibulum shows a smooth wall that ascends to the left, superiorly to the trabeculae and above the arch of the supraventricular crest to the pulmonary orifice. An important morphological characteristic that differentiates the ventricles is that in the LV there is a continuity between the input and output components (mitral-aortic continuity), however, in the RV there is a muscle flange, which separates both components, called supraventricular ridge [1].

The LV receives blood from the left atrium and pumps it through the aortic artery to all the tissues of the body. As the RV, it can be divided into an inflow region that comprises the mitral valve, an outflow region that includes the aortic valve, and an apical portion composed by the trabeculated endocardium. LV walls are thicker than those of the RV. This is due to the fact that LV must generate enough pressure to overcome the systemic vascular resistance, which is greater than the pulmonary vascular resistance. In addition, the lateral wall of the LV (opposing the septal wall) is more muscular at the base than at the apex of the ventricle. The muscular septal wall is curved, which gives the LV an ellipsoidal shape.

The LV endocardium is characterized by a complex network of thin trabeculae, that includes in more than 50% of cases strands (false tendons) that connect the septum and the papillary muscles.

1.1.2 Cardiac tissue organization

The cardiomyocyte is the working unit of the myocardium. These individual muscle cells are connected together in chains, supported by a matrix of connective tissue, to create a complex three-dimensional and cross-linked network [2].

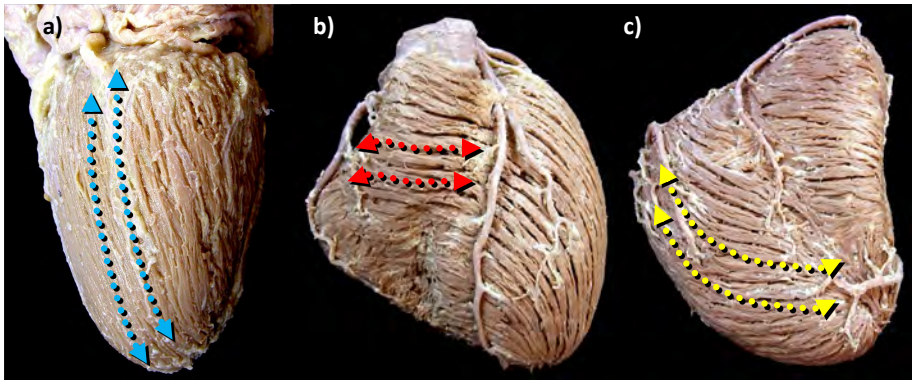

Figure 1.2: Fibres parallel to the long axis of the ventricular mass are described as longitudinal (a), whereas fibres parallel to the short axis are described as circumferential (b). Fibres at an angle to these major axes are described as oblique (c). Image courtesy of Damián Sánchez-Quintana.

The cardiomyocytes that make up the heart walls show a complex organization, that is far from homogeneous along its structures or regions. The term fibers describes the macroscopic appearance of strands of cardiomyocytes. Their alignment defines the longitudinal axis along which the electrical impulse is favored, since depolarization signals travel faster in some preferential directions than others. Only histological techniques can reveal with enough detail the arrangement of those cardiomyocytes, although some promising imaging techniques such as diffusion-tensor magnetic resonance imaging (MRI) or micro Computed Tomography (CT) can provide very good approximations from *ex vivo* atria and ventricles. Modelers that want to take into account the myofiber architecture need to analyse *ex vivo* samples and impose those fiber orientations learn from a few cases into their three-dimensional models.

In general, the macroscopic appearance of muscle bundles in the ventricles is described by anatomists using three main orientations: longitudinal (parallel to the long axis of the heart), circumferential (parallel to the sort axis) and oblique (any other angle)[1]. These orientations are shown in Figure 1.2.

The LV wall comprises three transmural layers or regions if we attend to the longitudinal orientation of the myocardial strands: subepicardial, mid-myocardial, and subendocardial. In the RV, the mid-myocardial region is not present. In each layer, the arrangement of the muscle fibers is different, what allows to distinguish one layer from the other. Therefore, the orienta-

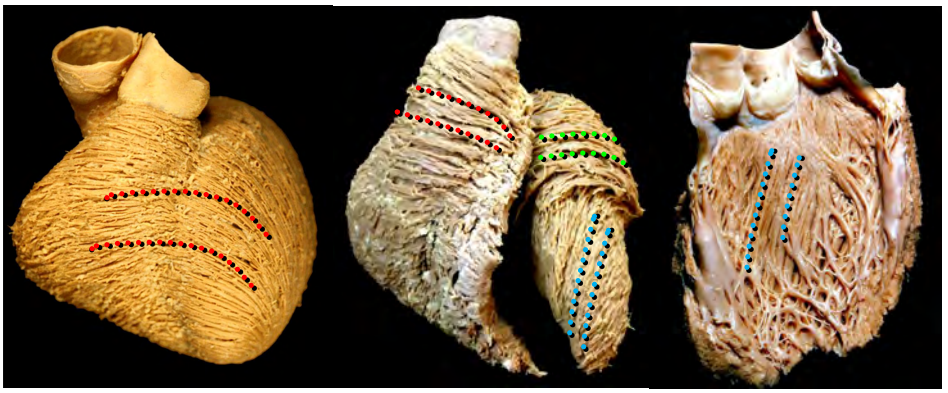

Figure 1.3: Different myofiber layers found in the ventricles. Subepicardial (red points), mid-myocardial (green points) and subendocardial (blue points) layers are shown. Note the continuity of the subepicardial layers between ventricles and the nonexistence of the mid-myocardial layer in the RV. Image courtesy of Damián Sanchez-Quintana.

tion of the myocardial strands varies transmurally in a continuous fashion, since there are not cleavage planes or sheets of fibrous tissue between layers. The subepicardial layer of the ventricles can be observed simply removing the visceral epicardium. Strands originate at the base of the heart and direct towards the apex, extending from one ventricle to the other. In the RV, the muscle fibers run more horizontally than in the LV. The subendocardial or deep layer consists mainly of longitudinal fibers that follow three different directions, towards the papillary muscles, toward the atrioventricular and arterial orifices, and towards the interventricular septum. This layer is very thin in the LV, although it is reinforced at the level of the papillary muscles [3]. The fibers that form the trabeculae run longitudinally, that is along the long axis of the trabeculae. The middle layer, only present in the LV, shows strands arranged in circular orientation. This is the layer that generates the necessary force to pump blood through the aorta artery. All these layers can be visualized in Figure 1.3.

Although there are small variations in the arrangement of fibers between individuals, the organization of the myocardium in three layers depending on the orientation of myocytes is a widely accepted theory and has been also corroborated by means of MRI [2]. It has been observed that the orientation of the major axis of the muscle fibers changes from an organization parallel to the equator in the surface, to a longitudinal orientation in deeper layers, with the myocytes mostly oriented parallel to the endocardial surfaces and epicardial. Streeter et al. [4] in several studies that involved hearts from

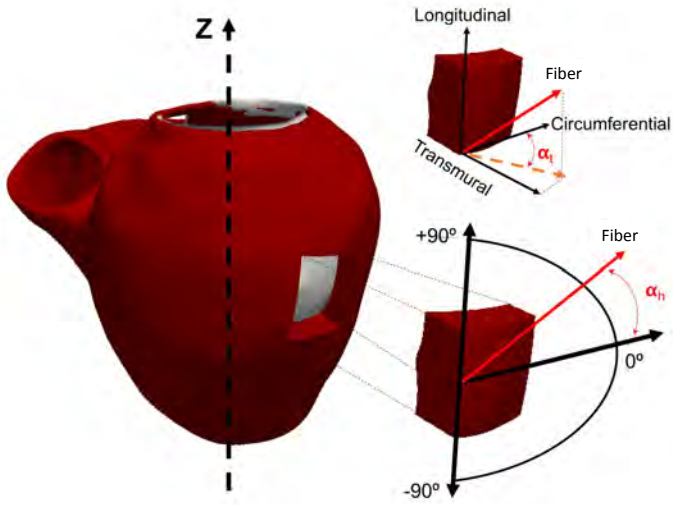

Figure 1.4: Definition of the helix angle (α_h) and the imbrication angle (α_t) in a 3D slab of tissue from a human heart model.

different species, measured the changing angles of the longitudinal axis of the strands of myocytes across the LV wall. The measured angle, known as helical angle, was defined by the long axis of the fiber relative to the ventricular equator plane. This angle presents a continuous gradual change in all the walls of the left and right ventricles. In addition to the helical angle, it has also been described a second angle that is the oblique or imbrication angle. This angle defines the deviation of the longitudinal axis direction with respect to the endocardial-epicardial plane. Therefore, the helical angle defines the deviation in the longitudinal axis of the ventricle, that is apex-base, and the imbrication angle the deviation endocardium-epicardium. While the helical angle can range between +90 to -90, the imbrication angle shows a little deviation. A graphic definition of these angles can be seen in Figure 1.4

1.1.3 Cardiac electrophysiology

Cardiac electrophysiology is the science of elucidating, diagnosing, and treating the electrical activities of the heart. One of its clinical goals is to study complex arrhythmias, analyse abnormal electrocardiograms, elucidate symptoms, evaluate the risk of developing future arrhythmic events and plan the patient treatment.

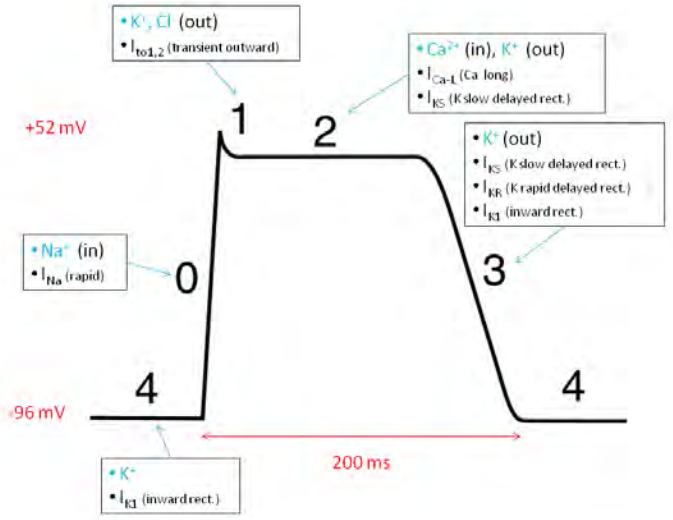

Figure 1.5: Action potential of a cardiomyocyte, showing the main ion currents of each phase.

Cardiac cells can build an electrical potential difference, known as the resting membrane potential, between the inside and outside of the cell through the action of ion pumps and ion channels (sodium (Na^+), potassium (K^+), and calcium (Ca^{2+})), see Figure 1.5. When the cell is at a resting state, the cell maintains a resting potential (Figure 1.5, phase 4). During the resting potential phase, the interior of the cell has a negative charge compared to the exterior of the cell. A current movement through the gap junctions that increases the transmembrane potential above a critical point known as threshold potential will trigger the action potential initiation (voltage-dependent Na^+ channels open), which starts the depolarization of the cell (Figure 1.5, phase 0). Action potential initiation will affect other cell ion channels, in particular it will activate voltage-gated Ca^{2+} and K^+ channels (Figure 1.5, phase 1). An important channel is the voltage-gated L-type calcium channel that allows calcium to enter the cell, sustaining the depolarized state when sodium channels close (Figure 1.5, phase 2). Finally, the voltage-gated K^+ channels open after some delay to move potassium ions down its concentration gradient, that is from intracellular to extracellular space. This drives the cell again toward the negative resting state, and is called repolarization (Figure 1.5, phase 3). From the initiation of the action potential through approximately half of the repolarization, the cell is considered refractory, and cannot respond to a new depolarization signal [5].

There have been described different spatial variations of the action potential waveform in the ventricles. Measurements performed in isolated cells, sometime in animals, are difficult to measure *in vivo*, where the electrotonic currents exchanged between neighboring cells tend to mask the individual differences in action potential. All these differences in action potential duration (APD) can be arrhythmogenic, since spatial dispersion of the APD can lead to temporal dispersion of repolarization, and a premature stimulus (ectopic focus) can result in a functional block initiating electrical reentry [5, 6] .

The contraction of the atria and the ventricles is carefully regulated by the transmission of electrical impulses that result from the propagation of the action potential throughout the heart. The cardiac conduction system synchronizes the activation of remote areas, and ensures the proper timing of the transfer of activity between the atrial and ventricular chambers. After pacemaker cells (sino-atrial node) trigger the initial depolarization, the electrical impulse travels very fast within the cardiac conduction system in a coordinated fashion. In the ventricles, following atrioventricular nodal excitation, impulses continue down to the His bundle. The His bundle conducts the electrical impulse and branches off into the left and right bundle branches that spread the impulse in the left and right ventricles by means of the Purkinje network. All the specialized conduction tissues in the ventricles are insulated electrically from the surrounding myocardial tissue, with exception of the terminal connection points. From those points the electrical impulse reaches the myocardium depolarizing the whole ventricles [7].

1.1.4 The electrocardiogram

Despite the great technological advances that allow to monitor with a great level of detail the heart, the electrocardiogram (ECG) remains the most widely used tool to assess patients cardiovascular status. The electrical currents generated in the heart are also spread to other tissues in the body. This electrical activity can be recorded on the torso surface, which provides noninvasive information about cardiac electrical function. Basically, the electrocardiogram measures the changes in the resultant electrical field during the electrical activation and repolarization of the heart in each cardiac cycle by means of electrodes placed on the torso. Therefore, the ECG can be seen as a global measurement of the cardiac electrical activity in each time point along the cardiac cycle, since the signal recorded is the sum of

the contribution of all the cardiac cells at a given instant. Although the ECG is a very useful tool, it is also imprecise, since many different internal heart events can give rise to the same recordings.

There are different configurations used to study the electrical activity of the heart, being one of the most standard the 12-lead electrocardiogram. The leads are: 3 bipolar limb leads (I, II, III), 3 augmented unipolar leads (aVR, aVL, aVF) and 6 precordial unipolar leads (V1, V2, V3, V4, V5, V6).

Electrode placement is chosen according to specific anatomical guidelines, in that way information about the magnitude and direction of the heart electrical activity can be recorded and replicated between recordings. The standard electrode placement is shown in Figure 1.6. Limb leads and augmented leads are calculated from three electrodes attached to the left arm, right arm and left leg. Sometimes a fourth lead is placed in the right leg as a ground. All of them provide information of the heart activity in the vertical plane, describing the direction of the depolarization and repolarization (leftwards, rightwards, superior or inferior) Precordial leads give information in the horizontal plane (anterior, posterior, leftwards, rightwards), and can describe more accurately the electrical activity in different regions of the heart [8]. A correct placement of the electrode positioning is crucial in order not to obtain false interpretations of the ECG, since minor variations of the electrodes position can considerably modify the recorded wave [9, 10]. As the ECG is recorded, signals of voltage (mV) over time (seconds) are produced and usually displayed in the electrocardiograph. The signal waveform at each lead has a typical known signature, with peaks and waves that correspond to depolarization and repolarization phases.

Currently, the 12-lead ECG is the main tool for the diagnosis of most arrhythmia.

1.2 Cardiac arrhythmias

Cardiac arrhythmias are alterations of the normal cardiac rhythm, and the sequence of activation. During an arrhythmia episode, the heart rate can increase (tachycardia, above 100 beats/min), decrease (bradycardia, below 60 beats/min) or became irregular. Of particular interest for this thesis are idiopathic ventricular tachycardias (VTs) which are tachycardias originated in ventricles with the absence of any significant structural disease. The most common way to diagnose an arrhythmia is by evaluating the patients ECG,

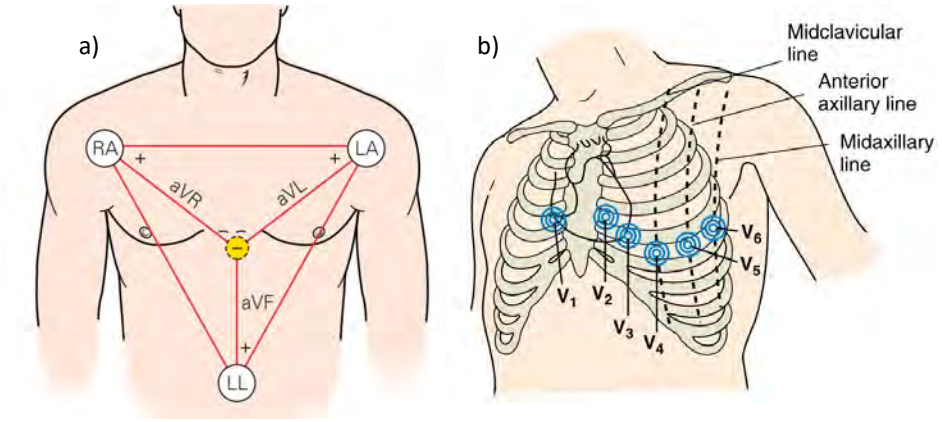

Figure 1.6: a) Bipolar limb leads and augmented unipolar leads. Electrode location is also shown. b) Precordial leads electrode placement. Reproduced, adapted an modified from [11].

which can be complemented by an echocardiographic study, and in specific cases by the use of electro-anatomical mapping (EAM).

The most common treatments for arrhythmia include, the use of drugs (beta blockers, blood thinners), implantation of pacemakers and intracardiac defibrillators (cardiac resynchronization therapy), and surgery (radiofrequency ablation) [12].

Apart from the classification as a function of the heart rate in tachycardia and bradycardia, arrhythmia can be analysed by mechanism: automaticity, re-entry, triggered; duration: paroxysmal, sustained, permanent; site of origin: atria, ventricles, conduction system.

There are three basic mechanisms that can elicit heart tachycardia: automaticity produced by ectopic focus, re-entrant activity produced by rotors and spiral waves, and triggered activity produced by cell afterdepolarizations [5]. All these mechanisms happen in both atria and ventricles. Tachycardia might degrade into fibrillation due to the electrical changes at ionic level produced by sustained fast heart rhythms. Heart tachycardia can be classified as non-sustained, if the fast rhythm self-terminates within 30 seconds, or sustained if it lasts more than 30 second.

The most common type of idiopathic ventricular tachycardias are the ones originating from the LV and RV outflow tracts (OT). OTVAs manifest in 3 forms: as isolated premature ventricular contractions, repetitive non-

sustained VT and sustained VT and can be treated by drugs or using radiofrequency ablation (RFA) [13].

1.2.1 Outflow tract ventricular arrhythmias (OTVAs)

Although RVOT has been considered as the most probable focus of OTVAs (80%) [14, 15] recent studies show that a LV outflow tract (LVOT) site of origin (SOO) can be identified in 50% of cases [16, 17]. Therefore, a thorough analysis of OTVA characteristics and the current diagnosis tools, like ECG, are essential for identifying the SOO and applying a proper treatment.

The cause of OTVA origin remains unclear, although the main mechanisms for the initiation are related with the calcium-dependent triggered activity in delayed afterdepolarizations [18]. As a results, OTVAs are always focal arrhythmias that can be effectively ablated using RFA. This approach is the recommended due to its success rate an low complication risk in the procedure [12]. Nonetheless, OTs present a particular 3D structure with complex anatomical relationships between the two ventricles, that makes it difficult to identify the SOO. An image of the OT region is shown in Figure 1.7. Since RVOT presents a different embryonic development than the LVOT, their structure presents significant differences [19]. RVOT is formed by a tubular structure, the infundibulum, and is located anteriorly and at the left of the LVOT. The infundibulum is divided from the rest of the RV by the supraventricular crest and ends in the pulmonary valve (PV). LVOT has less size than the RVOT and is located anteriorly at the aortic valve (AV) level. It contains the aortic root, which is divided in the left coronary aortic sinus (LCAS), right coronary aortic sinus (RCAS) and the noncoronary aortic sinus (NCAS). Each of these sinuses respectively support a leaflet or cusp: the left coronary cups (LCC), the right coronary cusp (RCC) and the noncoronary cups (NCC). These names of the cusps are also commonly used by electrophysiologist to describe the different aortic sinuses. The LCAS and RCAS are located next to the RVOT while the NCAS lies next to the interventricular septum. Between the aortic valve and the mitral valve there is a fibrous region named the aorto-mitral continuity (AMC) [20]. PV and AV are perpendicular to each other, being the level of the PV superior to the AV.

A great number of RVOT arrhythmias are originated in the septal, anterior and superior areas of the infundibulum, just inferior to the PV. Less common origins can be found in the RV free wall, or in the septum [13, 21]. In

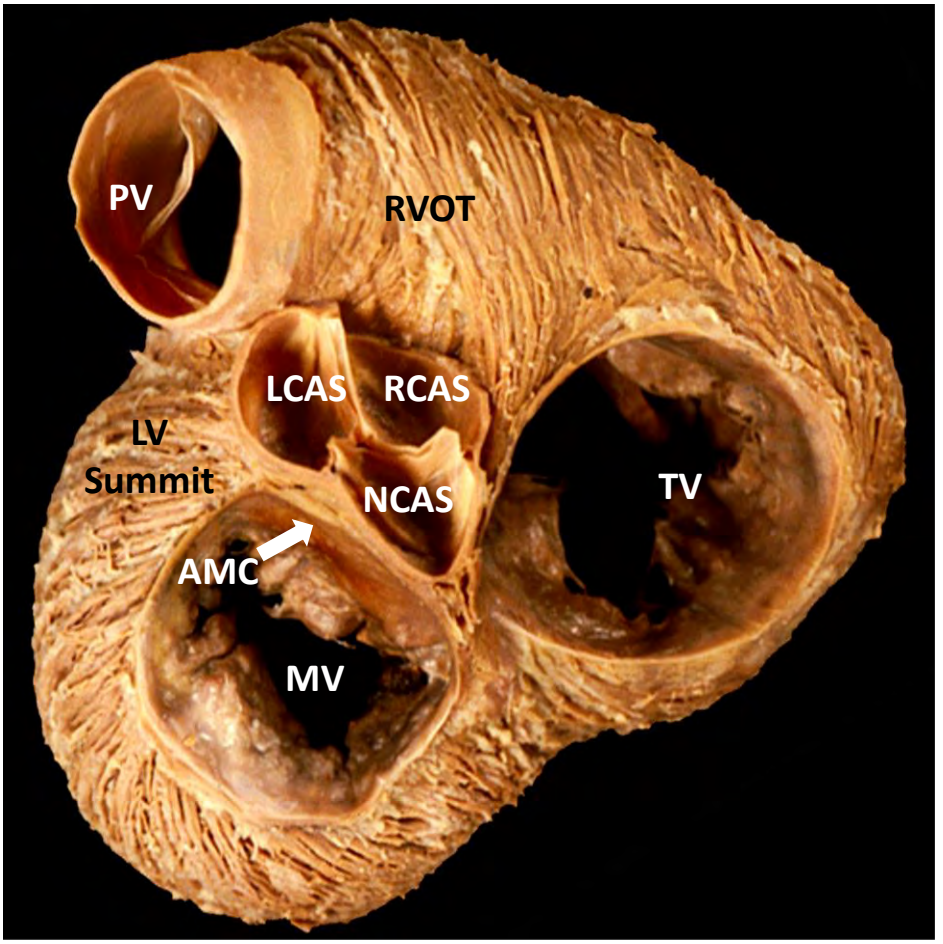

Figure 1.7: Image shows a sagital section of the ventricles viewed posteriorly. Note the central location of the aortic valve and its position in relation to the pulmonary valve and the RVOT. LCAS and RCAS lie adjacent to the septal part of the RVOT whereas the NCAS has a more posterior location. AMC: Aortic-Mitral continuity, MV: Mitral Valve, NCAS: Noncoronary aortic sinus, LCAS: left coronary aortic sinus, RCAS: right coronary aortic sinus, TV: tricuspid valve, PV: pulmonary valve, RVOT:right ventricle outflow tract ; LV:left ventricle

LVOT, arrhytmias commonly emanate from the LCAS and RCAS. NCAS is rarely a source of tachycardias, [22]. OTVAs can also have an epicardial origin. It is estimated that 15 % of OTVAs have their origin in the left ventricular summit [22]. This region correspond to a triangular region in the highest part of the LVOT epicardium, bounded by the bifurcation between the left anterior descending and left circumflex coronary arteries.

1.2.2 Diagnosis of OTVAs

OTVAs have a focal origin, therefore characteristic ECG patterns can be observed among patients and used for determining the SOO [13, 15, 23]. As a general observations, wide QRS complexes in the inferior leads (II, III and aVF) that present notching are an indicator of SOO in the anterior wall of the RV. When the activation is in the septal wall (RV or LV) QRS are narrower. Lead I is generally used for determining if the SOO has an anterior or posterior location (negative or positive polarity of lead I, respectivley). An essential indicator for determining the origin is the precordial transition, which is the lead where the QRS changes from predominately negative to predominately positive, i.e. with a R/S ratio >1. Late precordial transition (V3 and V4) is characteristic of RVOT arrhythmias. On the other hand, early precordial transition (V1 and V2) is mainly seen in LVOT tachycardias. Note that the 12-lead ECG can also be used as a template in pace-mapping procedures, in cases where the VT is not inducible during the ablation procedure.

Unfortunately, in a large number of patients the ECGs do not allow to predict accurately the SOO. This is due to the complex geometry and the close proximity of the OTs that complicates the diagnosis and the location of the SOO [15]. Although during the ablation intervention electrophysiologists will apply more effective and accurate techniques to find the SOO, it is necessary to have an estimation of the SOO previously to the ablation intervention since it affects the planning and timing of the ablation, the risk evaluation and the catheter approach. Depending the estimation of the SOO, electrophysiologist will have to map complex structures such as the distal coronary sinus, the aortic root or the epicardium. Moreover, when the SOO is estimated at the RVOT, the intracardiac catheter is introduced via the right femoral vein whereas in the LVOT cases, the catheter reaches the LV through the femoral artery. Finally, in cases where there is a LV epicardial SOO the region is accessed through the coronary venous system [13]. Several studies have proposed algorithms to predict the SOO based on the standard ECG recordings of the patient, which are mainly based on the existence of transitions in the precordial leads and the amplitude of the QRS [23]. Some of these algorithms derived indices such as the R-wave duration index and R/S amplitude ratio index [24], V2 transitional ratio [14], the V2S/V3R index [25] and the transition zone index [26]. Other studies [9, 27, 28] proposed to modify some of the standard precordial lead positions to improve the accuracy of the ECG-based predictions. In

particular, moving leads V5 and V6 to more posterior locations (V7, V8, V9) [27, 28], or modifying leads V1 and V2 [9], which seems to provide more information of the wave propagation and increase the effectiveness of the prediction. Finally, some not ECG-based approaches have also shown relatively good accuracy in differentiating RVOT vs LVOT origin using indices such as the aorto-pulmonary valvular planar angulation [17] or the area and ratio of the 10 ms isochronal activation pattern [29, 30].

All these ECG-based algorithms present good results in their original publication, but their accuracy decrease when tested with different populations, especially when they are applied to patients with V3 transition which are approximately the 40 % of OTVA patients [16]. In addition, measurement of the parameters highly depends on the clinician ECG analysis skills and presents high inter-observer dependence/variability. Furthermore, application is restricted in patients with paced rhythms or intraventricular conduction disorders [17]. Therefore, new approaches capable of predicting the SOO and further study the OTVAs are still needed.

1.2.3 Radiofrequency ablation treatment of OTVAs

Radiofrequency ablation technique applies to the cardiac tissue high temperatures resulting from high-frequency alternating currents. Heat is generated at the tip of a catheter that is introduced to the heart and monitored using fluoroscopic imaging. Once heat is applied to an arrhythmic SOO, it destroys the cells responsible to generate the undesired electrical activity and ends the arrhythmia. However, before applying RFA, SOO needs to be located with precision.

EAMs and pace mapping are the two principal methods for determining the SOO. Before the ablation is performed the electrophysiologist constructs a chamber EAM, that guides him towards the regions that need to be ablated. EAM measures the intracardiac electrical activation that is related to a certain anatomical location of the heart. It provides information used in different approaches such us activation mapping and/or the voltage mapping. In addition to that, EAM systems monitor the position of the ablation catheter without using fluoroscopic imaging and integrate all this information in 3D images [31]. Activation mapping consist in the analysis of the electrical activation sequence during a certain rhythm. This is the most reliable method for finding the earliest activation site and therefore the SOO of the VT. Voltage mapping evaluates the amplitude (voltage) of the

electrogram signal and allows to identify heart structures involved in the generation of OTVAs such as the PV [29, 31]. On the other hand, pace-mapping is used in non inducible tachycardia and in rare cases of ectopic foci. The method consists in pacing different points of the heart and recording the morphology of the obtained ECG. If the pacing reproduces the same ECG morphology observed in the 12-lead ECG during the clinical VT, the SOO of the arrhythmia is supposed to be in that location [21, 32]. This technique requires no induction of the VT, and has a better performance in the localization of focal tachycardias like OTVAs. Their main disadvantages are the resolution, which is lower than the provided by activation mapping and the subjectivity in the 12-lead ECG comparison, although some studies have shown different methods for an objective comparison [21, 33, 34].

1.3 Biophysical models of the heart

Over the last years, new medical imaging technologies have allowed obtaining clinical information with a high level of detail, and specific to each patient. The amount of data currently available represents an important opportunity to transform the diagnostic model of cardiovascular diseases through a greater degree of personalization of therapies. However, to improve the understanding of cardiovascular diseases, not only geometric and mechanical information is required, but also a thorough knowledge of the different physics present in the heart (electrophysiology, mechanics, haemodynamics) and physiological information. In this context, a huge amount of information has been generated in recent years at different levels: subcellular, cellular, tissue, organs and systems [35]. Nonetheless, knowledge of each element is not enough to understand its behavior as an organ. An integrative approach is therefore necessary, which must consider all the element interactions in order to study the origin and maintenance of cardiac arrhythmias and improve its prevention [36, 37]. For all these reasons, to continue improving our knowledge about the origin and maintenance of cardiac arrhythmias, and to advance therapeutic methods, it is of great importance to develop predictive models that integrate information from different levels or spatial scales. These personalized electrophysiological simulations have already shown promising results to support clinical decisions in cardiology [38, 39].

In the last years, an extensive number of mathematical models have been built to reproduce the electrical (cardiac electrophysiology) and mechanical

(tissue deformation) dynamics of cardiac cells and tissues. Although models are by definition simplifications of a real object or phenomenon, they can serve the important purpose of helping researchers in gaining knowledge about a given process or function, and avoid at the same time unnecessary animal experiments.

The biophysical models of the heart are also starting to be embraced in clinical research environments to assess their predictive capacity for treatment delivery and optimization. The applications are countless, and although they will require a long validation process and acceptance from the clinical community, the initial results are promising. Some of the therapies that could potentially benefit from biophysical models are cardiac resynchronization therapy or radiofrequency ablation, among others.

In addition, last years advances in computing resources and imaging technologies, have led to the development of patient-specific models. These models, generated using *in vivo* imaging, accurately represent the cardiac anatomy of the subject and incorporate material properties and cardiac features of the patient.

A cardiac 3D model is composed of a 3D geometry, myocardial structure, electrophysiology models at different scales (cell to whole organ models), and specialized structures (e.g. the cardiac conduction system). Depending on the final application of the model, modelling a particular pathology (mutation, alteration of tissue properties, ...) might be also required.

1.3.1 Cardiac and thoracic anatomical representations

The geometry of a patient heart is usually represented by a 3D mesh made up of tetrahedral or hexahedral elements. The mesh is generated after the segmentation (manual or automatic) of medical images, being the most common MRI [38, 40, 41, 42] and CT [43, 44, 45].

The 3D cardiac models and, especially, the methods and sources of information used in its construction, have evolved greatly since its inception. The first models, created using geometric figures (ellipsoids), CAD models, or constructed by observations, have nothing to do with current detailed models updated by merging different modalities of high resolution medical imaging or modern atlas statistics for cardiac medical image segmentation [46, 47, 48]. The specific geometry of the patient's atria and ventricles can be accurately reconstructed from a wide variety of image se-

quences using advanced segmentation tools [49, 50]. For example, radiological imaging sequences can be processed and segmented using semi-automatic storytelling techniques such as active appearance models or active shape models [46, 47, 51]. This allows the construction of personalized geometric models to the patient that describes the anatomy of the heart and, in some cases, if data is available, include scar regions or the patient's coronary tree. In addition to the geometry of the organ, the relevance of characterizing and delimiting the pathological substrates of the myocardium has been highlighted, in particular, regions with fibrosis in the atrium or areas of scar and edge in the ventricle [52]. These substrates are highly pro-arrhythmic, and therefore are the target of radio-frequency ablation complications in clinical practice [53, 54].

In order to properly simulate OTVAs, a biventricular geometry that includes the OTs up to the PV and AV level is needed. It can be obtained using either MRI or CT image sequences. There is no need to have information above the PV and the AV since there are no myofibers located in these areas and therefore no electrical conduction [1].

Three-dimensional models of the heart can be incorporated into an electrical model of the human torso in order to reconstruct the changes in the electric field generated by the surface electrocardiogram (BSPM and ECG). The first anatomical models of the thorax were very simplified [55, 56], and considered the thorax as a homogeneous isotropic medium, without taking into account the effect of the different organs. Later studies began to include some of the electrical conduction properties of tissues such as skin, bones, muscles and lungs [57, 58]. The model developed by [59] was among the first to take into account the electrical properties of organs and tissues. It included the heterogeneity of some tissues such as skin, fat, muscle, bone or blood vessels, as well as organs such as the lungs and the heart, each of these regions presenting a different electrical conductivity value. The model of [58] also presented anatomical detail and was designed to validate the influence of the different organs of the thorax in the formation of the ECG. Recent torso models developed for the study of atrial arrhythmias [60] and arrhythmia generating foci still show unrealistic geometries and a limited number of organs. More recently, the heterogeneous models proposed by [61] and [62] were personalized to the patient. These models were developed manually by segmentation by an expert. The final objective of these models is to numerically address the direct problem and the inverse problem of electrophysiology and, to determine what is the mechanism associated with changes in pathological heart rate and activation.

1.3.2 Myocardial structure

Acquisition of medical imaging sequences is not sufficient for the construction of detailed biophysical computational models due to the importance of cardiac microstructure, which can only be obtained from invasive invasive studies (for example, histological data or DTI diffusion tensor image DT-MRI). The heart shows a high degree of organization and specialization of the different tissues at the structural level and at the cellular level [4, 63]. The *in vivo* data of a patient is very valuable, however they must be complemented with *ex vivo* population data in order to build complete multi-scale models [64]. These population-based data refer to common known characteristics that are not directly observable in the individual through clinical imaging techniques, but that are present and should be considered. Microstructural level data is essential for a correct representation and simulation of cardiac electrophysiology. Given the need to include this information, mathematical models have been developed that allow modeling the structures according to average observations in a given population [7, 65, 66]. For example, the arrangement of myocardial fibers in the ventricles and atria can be characterized by histological techniques for each region of the heart [67, 68]. These descriptions are then adapted to a segmented cardiac model of a specific patient, using rule-based mathematical models. Another common approach is based on the creation of statistical atlases constructed from exuberant information of the microstructure of the heart that can be adjusted to subsequently segmented models [48]. Recently, mathematical approaches to modeling tissue orientation in ventricle have been published [69, 70].

As described in previous works [71, 72, 73, 74, 75, 76, 77], cardiomyocyte orientation determines the preferential electrical wave propagation and tissue contraction in the heart. Hence, a proper orientation of the myofibers (aggregations of cardiomyocytes) is crucial for having accurate simulations results. There are two main options for incorporating myocyte orientation into 3D computational models of the heart: fitting of a map of fibers extracted from ex-vivo data; or using rule-based methods (RBM). RBMs are based on mathematical descriptions of myofiber data acquired from experimental observations and have become the most common strategy to incorporate fiber information in cardiac computational models. More detailed description of these methods will be explained in Chapter 3.

The cardiac conduction system (CCS) is the specialized cardiac tissue responsible for the fast transmission of the electrical impulse. The distribution

of the CCS in the ventricles will affect the depolarization of the wave [7]. CCS structure is mainly obtained from histological data and is incorporated to cardiac models either by automatic methods that build the Purkinje trees [78] or by estimating the Purkinje-myocardial junctions (connections between the CCS and the myocardium) from EAMs [40]. The involvement of the CCS in OTVAs is very marginal, and therefore, it is not a critical component in biophysical models aimed to study the origin of arrhythmia in those patients.

1.3.3 Electrophysiological simulations

The application of different experimental methodologies has allowed us to understand and quantify the biophysical and biochemical properties of the cardiac cells and the architecture of the heart both at the cellular and tissue levels. This knowledge has allowed the development of a considerable number of computational models of individual myocytes, myocardial tissue or the entire heart. The use of these electrophysiological models has contributed to establish new methods of studying the mechanisms that are behind cardiac arrhythmias. In general, myocyte models are based on the mathematical formalism of Hodgkin-Huxley [79, 80], and have increased their degree of complexity in parallel with the improvements in experimental techniques that allow measuring and characterizing the ionic currents responsible for the action potential [81]. Several computational models of cellular cardiac electrical activity have been developed, including ventricular myocytes [81, 82], atrial myocytes [83, 84], of the sinus node [85] and Purkinje fibers [86, 87].

At this point it is important to differentiate between the so-called phenomenological models and the predictive models. Phenomenological models are often macroscopic representations of a given phenomenon that can reproduce experimental results but do not have a reference to the physical system. On the other hand, predictive models can provide new findings, allowing insights into underlying mechanisms, outside the set of experimental conditions used to fit the model. Those latter models rely on anatomical and biophysical definitions of the phenomena under study.

- **Biophysical models** [88, 89]. These models include formulation for each transmembrane ionic channel and the ionic concentrations at the cellular level. Although they precisely describe the electrical activ-

ity of the cell, these models are computational demanding and often require the use of high performance computing.

- **Phenomenological models** [90, 91]. Models that are able to reproduce the action potential behaviour with simpler equations. However, they struggle to accurately reproduce complex physiological patterns such as rapid pacing or reentrant activities.

The propagation of the action potential in the heart, responsible for the contraction, has been studied both in normal situations and in arrhythmias through the use of finite element-based models that represent discrete tissues. These tissue models (1-D, 2-D or 3-D) can include the heterogeneous structure of cardiac tissue and heterogeneous expression at the cellular level, giving them a high level of realism [92]. Commonly used tissue propagation models are the two-domain model and the monodomain model [93], which are coupled to cellular models to form a multi-scale model. The mathematical problem associated with the resolution of the differential equations that govern the propagation of the electrical signal in a three-dimensional heart model is highly non-linear and has no analytical solution. Therefore, these models must be solved using numerical methods, such as the finite difference method or the finite element method. A 15 cm^3 tissue block (approximate volume of a rabbit heart) will have more than 15 million elements. In the problem of the electrical modeling of the heart each of these elements must be associated with a system of about 20-30 differential equations that must be solved with order time steps of milliseconds. Thus, the dimensions of the matrix for a human heart are enormous. Under these conditions, it is clear that the complexity of cardiac models implies the use of high performance computers (HPC, High Performance Computing) or GPU (Graphics Processing Unit) systems and software specifically designed to solve them [94, 95]. An alternative is the use of Eikonal models [44], where propagation and activation time are modelled by simple non-linear partial differential equations. However, they are not able to reproduce complex physiological states.

Since there is no presence of pathological tissue reported in OTVAs, all the electrophysiology models used in this Thesis will describe healthy tissue. Nonetheless, tissue heterogeneity (e.g endocardial cell vs epicardial cells) will be incorporated.

1.3.4 Electrocardiogram simulations

ECG is still the most widely used diagnostic technique in cardiology. However, it is an unreliable indicator of the potential for arrhythmogenesis, since the changes observed in the QT interval and the T wave of the electrocardiogram can be induced by very different molecular and cellular effects, both benign and malignant. The use of torso computational models in electrophysiology commonly attempts to solve the direct problem [96], that is, resolution of the equations of electrical propagation from the heart to the torso modeling certain pathologies such as ischemia [97, 98, 99, 100], re-incoming electrical circuits [101, 100], or ectopic beats [102]. The application of the torso models is twofold, since they can be used to solve the direct problem in electrophysiology and become validation tools for the biophysical models of the heart, since much information is available on the associated external ECG signals [103]. By having a 3D model it is possible to obtain the potential at all points that form the outer surface of the torso, giving rise to the BSPM, or Body Surface Potential Map. Some studies [104] already developed torso models to assess the influence of the conductivities of the different organs on the ECG.

Since we need to compare simulation results with patient non-invasive data (ECG) to validate our results, we have to include a framework to simulate body surface potential maps and ECGs. Work will be oriented to study the relationship between the OTVA electrophysiological activity and the electrocardiogram. Previous studies have shown successful results in using high detailed multi-scale heart-torso model to analyse the activation patterns [40, 45, 97, 105, 106].

In order to have a proper ECG simulation, a detailed generic torso model is required. The effect of torso organs and structures (lungs, liver, bones, ...) should be taken into account. Heart orientation respect to the torso has to be considered. BSPM can be calculated after a passive propagation of the extracellular potentials through all these regions. Finally, 12-lead ECG can be extracted from the torso surface by calculating the potential in the recommended points.

1.4 Machine Learning in Healthcare

In the last years, artificial intelligence has become one of the most extraordinary breakthroughs in medical research, thanks to the irruption of machine

learning (ML) and deep learning (DL). ML is a field of artificial intelligence whose aim is the generation of algorithms that are able to learn directly from observations in order to make predictions about future ones. The use of ML in healthcare applications has been increased due to the increment of the available digitalized medical data, the advances in software techniques and the generalized use of high performance computers [107]. ML can be applied to different task such as segmentation, registration or pattern recognition. However, the main application where ML techniques are used is data classification, usually after applying feature extraction and dimensionality reduction to the input data [108, 109, 110, 111].

ML algorithms can be categorized into supervised and unsupervised approaches. Supervised ML techniques are trained using labelled data and are used mainly in classification and regression tasks. On the other and, unsupervised ML techniques are used to find unknown patterns in the input dataset and are applied mainly in classification problems.

DL is a branch of ML that imitates how the human brain works and how the neurons are connected. DL uses multiple layers of nodes (neurons) to automatically extract features and patterns that will be used in different task such as classification or regression, although they require a large amount of input data. It is important to point out, that systems based on DL have as a limitation the complexity to explain how they arrive to particular predictions. Therefore, they become a black-box, that even though can be correct in their predictions, are difficult to be trusted by doctors that might not want to make life-and-death decisions based on systems that they do not understand.

However, machine recommendations, based on understandable machine learning algorithms might help physicians make the right choices in diagnosis and treatment, acting as an extension of medical knowledge. The idea is to be able to advance in the direction of personalized medicine in which everyones health recommendations and disease treatments can be tailored based on their medical history, anatomical constitution or environment conditions.

ECG is one of the most used clinical signals, and the application of ML to ECG can expand our knowledge about different pathologies. However, ECG databases are still not large enough to cover all the possible medical conditions with enough detail. Generation of ground truth is one of the principal limitations, since it requires electrophysiologists to annotate a big number of the recorded ECGs. Computer simulations can arise as an alternative to increase the number of ECG signals available for different patholo-

gies, enabling the training of ML systems. In addition, simulated signals will remove the errors associated with bad annotation of data or excessive noise. Some studies have already used simulated ECG signals [105, 112] for training a ML-based system. Among the most used techniques in ML for learning and classification are: support vector machines (SVM), random forest (RF). More sophisticated techniques include recent developments on Self-Organizing Maps (SOM) and Multiple Kernel Learning (MKL).

2

Motivation and Objectives

2.1 Motivation

Cardiac arrhythmias are one of the leading causes of mortality in Europe and impose a huge healthcare burden on society. Despite well-developed clinical guidelines for management of atrial fibrillation (AF) or ventricular tachycardia (VT), long-term treatment success rates remain unacceptably low due to complexity of the disease [12]. This economical and epidemiological burden demands new methodologies and tools that can improve patient management, therapy planning and delivery. Most of previous research on arrhythmias has been devoted to genetic, vascular, metabolic or myocardial function, since it has been only recently when more advanced systems have allowed to explore cardiac electrical function *in vivo*. Among them, electroanatomical mapping systems, introduced over the last decade, have become a primary tool to treat complex arrhythmias. These tools can be complemented with non-invasive advanced imaging techniques such as computed tomography (CT), magnetic resonance imaging (MRI) or 3D echocardiography, which can help to characterize cardiac diseases. The anatomy of the heart can be precisely reconstructed in 3D from computed tomography scans with high accuracy, and the cardiac function can be assessed by specific magnetic resonance imaging protocols. When these imaging techniques are combined with contrast agents, they can provide more detailed information about tissue status, such as amount of fibrosis present in a given heart region. Therefore, advanced information on disease and its evolution is within clinicians reach, who could apply novel therapeutic strategies to treat patients. All these tools and novel electrical therapies have proved to be cost effective and are now part of medical recommendations. However, the amount of data that has to be considered by electrophysiologists is overwhelming, and very difficult to integrate to stratify patients or optimize therapy planning and delivery. As a consequence, the overall clinical outcome in such therapies is still perceived as sub-optimal, with success rates in the range of 60 to 65%. It is necessary to develop novel methodologies and tools that help us to gain understanding in the pathophysiology of the heart, and at the same time serve to improve patient treatment. Computational models that simulate the electrical activity of the heart have proved to be a useful tool for better understanding the mechanisms that are behind the cardiac electrophysiology, and therefore are beginning to be used to evaluate and improve cardiac arrhythmia treatment.

2.2 Objectives

In current clinical practice, the measures adopted for the treatment of a large number of cardiac arrhythmias are decided mainly within the surgery, which prevents carrying out a detailed and personalized planning tailored to the patient. Usually the available data for the electrophysiologist are: the electrocardiogram, intra-cavitary electrical measurements of the patient (during the intervention), the experience of the doctor and the reference values for a normal population. Radio-frequency ablation (RFA) techniques are widely used in procedures for the treatment of arrhythmias, although they show a large number of "non-responders" for complex cases, that require recurrent interventions. A more robust pre-intervention evaluation of the patient would be of great benefit to the outcome of the procedure. The improvement could be achieved by incorporating new technologies from the area of computational physiology, combined with machine learning techniques to help infer the location of pro-arrhythmic electrical substrates and rotors. Having such information pre-operatively can have an impact in RFA techniques, improving the success of the intervention and reducing the total time. Nowadays, simulations are much faster, more cost-effective and less invasive than building and testing physical prototypes, or carrying large clinical trials, which makes this technology an interesting alternative.

The global aim of this thesis is to develop personalized computational models for the *in silico* study of outflow tract ventricular arrhythmias (OTVAs) and the evaluation of new strategies for their treatment with RFA therapy. After applying this technology, we expect to reach a better understanding of the mechanisms that are involved in OTVAs and to support clinicians in the planning of the ablation intervention.

This overall objective can be divided in the following steps:

- To build patient-specific models for OTVA simulations. Study the OT myocyte orientation and develop a RBM to reproduce this information in patient-specific models.
- To replicate, using electrophysiological simulations, the 12-lead ECG behaviour that is described in the OTVA clinical guidelines.
- To use all the information derived from the simulations to support clinicians to predict the SOO of OTVAs prior to the ablation intervention.

The clinical problems tackled in this thesis are challenging and are of great interest among electrophysiologists. In the last years several works have proposed different solutions, mainly based on ECG analysis, but they still present various limitations [13, 15, 16, 23, 25]. This work will propose a different approach to predict the SOO using patient-specific simulations.

2.3 Contributions

The thesis presents the following contributions:

- **The OT-RBM**. A novel rule-based method for assigning myofiber orientation specific to the RV, interventricular septum, and both OT of the ventricles, to replicate histological observations. These parts of the heart anatomy are often ignored by other RBM or imaging techniques. Thanks to the OT-RBM new electrophysiological and mechanical cardiac simulations can be performed where these parts have a crucial role. Works studying the outflow tract ventricular arrhythmias or the effect of trabeculae in the electrophysiology have been done thanks to the fiber generated with the OT-RBM while other works investigating the mechanics of the RV or the role of complex structures such as the false tendons are in the process of being carried out.
- **Simulation of outflow tract ventricular arrhythmias.** A full pipeline for OTVAs electrophysiological simulations on complete patient-specific biventricular geometries was developed. Results were properly validated using EAM data. In addition, OTVA patients 12-lead ECGs were also modelled and validated. To the best of our knowledge this is the first study to simulate this type of arrhythmias.
- **Combination of simulated and real data in training machine learning models** The use of simulations to train ML algorithms achieved groundbreaking predictions of SOO compared to current state-of-the-art. In addition, the use of advanced interpretable ML techniques improved the understanding of the relation between electrophysiological models of the heart and real ECG and electrogram data.

- **Clinical contributions** The *in silico* pace-mapping method proposed in this thesis represent a valid tool for pre-procedural ablation planning with potential for clinical translation in the future.

2.4 Outline of the thesis

After this chapter, the rest of the thesis is organised as follows.

Chapter 3. In this chapter, we describe the OT-RBM. We show the resulting myofiber orientation and compare it with the results obtained from other RBM and imaging techniques.

Chapter 4. This chapter presents a clinical application of the simulations of OTVA. We develop a pipeline for simulating ECGs from patient-specific geometries and compare the results with real patients ECG. The described methodology tries to *in silico* reproduce the pace mapping technique used by electrophysiologist during ablation interventions.

Chapter 5. In this chapter, ML techniques are used to classify resulting ECGs obtained from OTVA simulations and to train different supervised and unsupervised ML algorithms to predict the OTVA origin using ECGs.

Chapter 6. This chapter summarizes the most important ideas and contributions of this thesis. We highlight the strengths and propose future research directions.

3

A rule-based method to model cardiomyocyte orientation in cardiac biventricular geometries with outflow tracts

Abstract – Rule-based methods are often used for assigning fiber orientation to cardiac anatomical models. However, existing methods have been developed using data mostly from the left ventricle (LV). As a consequence, fiber information obtained from rule-based methods often does not match histological data in other areas of the heart such as the right ventricle (RV), having a negative impact in cardiac simulations beyond the LV. In this work, we present a rule-based method where fiber orientation is separately modeled in each ventricle following observations from histology. This allows to create detailed fiber orientation in specific regions such as the endocardium of the RV, the interventricular septum and the outflow tracts. We also carried out electrophysiological simulations involving these structures and with different fiber configurations. In particular, we built a modelling pipeline for creating patient-specific volumetric meshes of biventricular geometries, including the outflow tracts, and subsequently simulate the electrical wavefront propagation in outflow tract ventricular arrhythmias with different origins for the ectopic focus. The resulting simulations with the proposed rule-based method showed a very good agreement with clinical parameters such as the 10 ms isochrone ratio in a cohort of nine patients suffering from this type of arrhythmia. The developed modelling pipeline confirms its potential for an *in silico* identification of the site of origin in outflow tract ventricular arrhythmias before clinical intervention.

This chapter is adapted from: Ruben Doste, David Soto-Iglesias, Gabriel Bernardino, Alejandro Alcaine, Rafael Sebastian, Sophie Giffard-Roisin, Maxime Sermesant, Antonio Berruezo, Damian Sanchez-Quintana, and Oscar Camara. A rule-based method to model myocardial fiber orientation in cardiac biventricular geometries with outflow tracts. International Journal for Numerical Methods in Biomedical Engineering, 2019; 35:e3185.

3.1 Introduction

Personalized electrophysiological simulations have shown promising results to support clinical decisions in cardiology [38, 39]. One important factor that affects these simulations is how myocardial fiber orientation is established in the heart model. As described in previous works [71, 72, 73, 74, 75, 76, 77], cardiomyocyte orientation determines the preferential electrical wave propagation and tissue contraction in the heart. Therefore, a proper orientation of the myofibers (aggregations of cardiomyocytes) is needed to obtain valid and accurate simulation results. However, determination of the 3D architecture of myofibers has been a challenge for anatomists among centuries. Only in the last 30 years, due to recent advances in microscopy and medical imaging, fully detailed descriptions have been obtained [113, 114, 115, 116, 117, 118]. Imaging techniques such as diffusion tensor magnetic resonance imaging (DT-MRI), micro-CT or X-ray phase-contrast imaging, make possible to acquire information about myofiber distribution. Unfortunately, most of these imaging techniques can only be applied on ex-vivo specimens since they need long acquisition and reconstruction times to collect accurate myofiber information. Researchers are currently developing *in vivo* DT-MRI sequences [119, 120, 121], showing very promising results. Yet these advanced imaging techniques cannot easily be applied to patients nowadays and are still limited to a reduced number of 2D slices followed by 3D interpolation techniques, providing coarse spatial resolution and low signal-to-noise ratios.

Due to the difficulties to acquire patient-specific data, there are two main options for incorporating myofiber orientation into 3D computational models of the heart: fitting of a map of fibers extracted from ex-vivo data; or using rule-based methods (RBM). Fitting of fiber maps can be achieved using atlas-based methods, which warp a template or an average atlas of fibers obtained by imaging techniques into a new heart geometry [122, 123, 124] or using statistics-based predictive techniques for assigning the fibers [125]. However, these methods require complex registration algorithms to establish correspondences between different heart geometries and are highly dependent on the quality of the original data. The second option involves rule-based methods. RBMs are based on mathematical descriptions of myofiber data acquired from experimental observations and have become the most common strategy to incorporate fiber information in cardiac computational models. Since the study by Streeter [4], where fiber orientation was studied in canine hearts, a high number of RBMs have been developed and

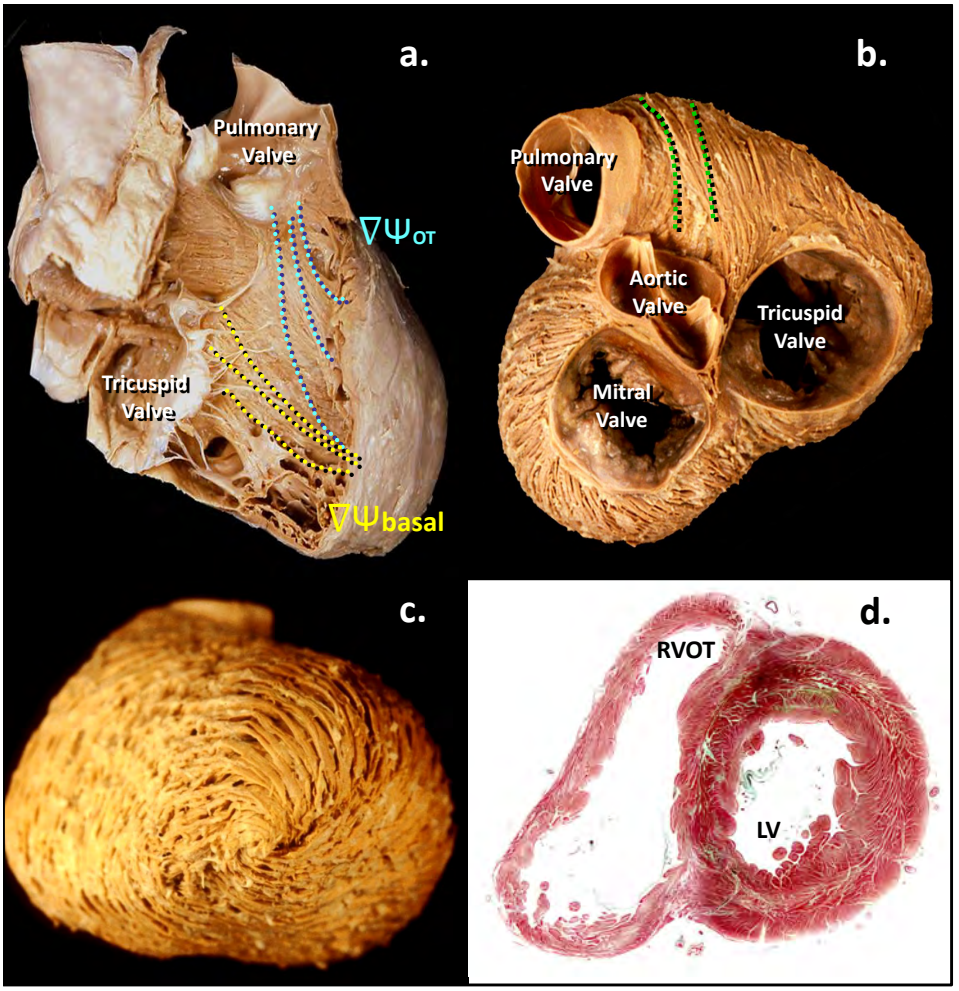

Figure 3.1: Histological data of the heart. a) Fiber configuration in the RV sub- endocardium, with longitudinal directions to the pulmonary and tricuspid valves (dashed blue and yellow lines, respectively). b) Epicardial fiber configuration of both ventricles (top view). The dashed green line represent circumferential fibers of the OT. c) Apical view of the fiber epicardial layer d) Short axis slice of the heart showing transmural fiber orientation. $\nabla\Psi_{basal}$: apico-basal direction; $\nabla\Psi_{OT}$: apico-OT direction; RVOT: Right Ventricle Outflow Tract; LV: Left Ventricle

used by the scientific community due to their relatively easy adaptation to any geometrical model [70, 126, 127, 128].

The two described strategies have the common issue of being mainly focused on the LV. This is due to the complexity of obtaining accurate data of the RV, especially on fiber orientation. For instance, according to histological

data, fiber orientation in the RV sub-endocardium has a longitudinal direction from apex towards pulmonary and tricuspid valves, as illustrated in Figure 3.1, which is not the case in LV-based RBM. The outflow tract (OT) of the ventricles is a structure that plays a key role in some pathologies like outflow tract ventricular arrhythmia (OTVA). It has a particular fiber configuration with longitudinal and circumferential directions in the sub-endocardium and sub-epicardium, respectively. Unfortunately, most biventricular computational models include an artificial basal plane well below the valves rather than a complete biventricular geometry, thus not including the outflow tracts.

To overcome these issues, we have developed a RBM that includes specific fiber orientation in different cardiac regions such as the RV endocardium, the interventricular septum, trabeculae and the outflow tracts, following observations from histological data. This outflow tract extended RBM (OT-RBM) allows running *in silico* simulations modelling pathologies where these regions are relevant such as OTVAs and Tetralogy of Fallot, among others. The OT-RBM processes both ventricles independently, which gives more flexibility to generate different fiber configurations. Therefore, septal fiber orientation can also be independently modified, allowing the study of its discontinuity, which is still under debate [129, 130, 131]. Furthermore, the OT-RBM can also be adapted to model myofiber orientation of complex structures such as trabeculae, papillary muscles, moderator band or false tendons. These structures have a crucial role in the mechanics and electrophysiology of the heart and present a fiber orientation different from the rest of the ventricular muscle [132]. In this work, the introduced RBM is compared with state-of-the-art fiber generation models such as the ones based on Streeter observations [4] and Bayer et al. [70], as well as with DT-MRI data. Additionally, electrophysiological simulations with fiber orientation provided by the OT-RBM are performed in a set of nine patient-specific OTVA biventricular geometries. Simulation results are then compared to clinical observations from EAMs of these patients for different sites of origin of the ectopic focus.

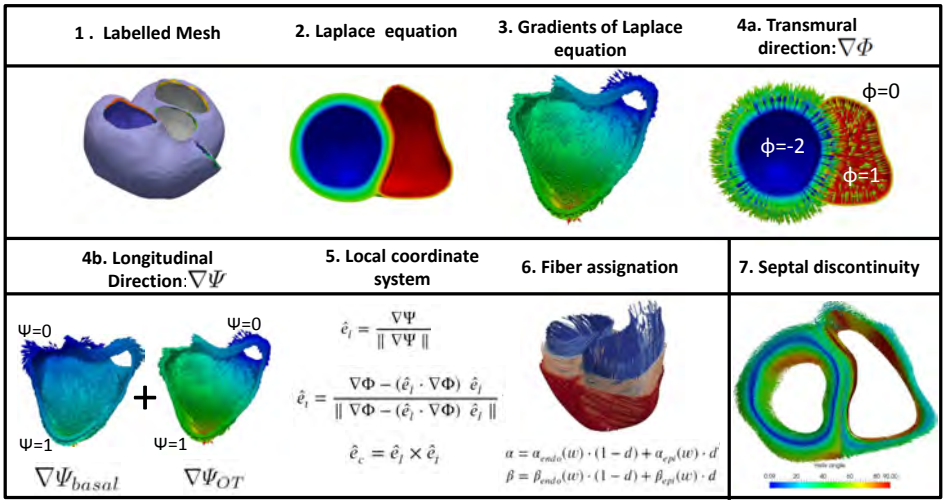

Figure 3.2: Scheme showing the different steps of the OT-RBM. $\nabla\Psi$: longitudinal gradient; $\nabla\Psi_{basal}$: apico-basal gradient; $\nabla\Psi_{OT}$: apico-OT gradient; $\nabla\Phi$: transmural gradient; $\hat{e}_l$: longitudinal axis; $\hat{e}_t$: transmural axis; $\hat{e}_c$: circumferential axis.

3.2 Methods

3.2.1 General overview

The OT-RBM uses the Laplace-Dirichlet method introduced in the work of Bayer et al. [70] (which is mainly based on LV fiber observations) to create a new local coordinate system in each point of the mesh. This coordinate system allows assigning specific fiber information in the RV according to histological data and extending it to the outflow tracts of both ventricles. Additionally, the proposed RBM allows, if necessary, septal fiber discontinuities between the LV and RV. The whole pipeline to develop the new RBM is summarized in Figure 3.2. It starts with the generation of volumetric labeled biventricular meshes, representing cardiac structures including outflow tracts from both ventricles up to the valve planes. Subsequently, the Laplace equation is solved with different boundary conditions to define the directions (i.e. transmural and longitudinal) required for the local coordinate system that will guide fiber assignment at each point of the mesh. The longitudinal direction in both ventricles is defined as a combination of the vector fields resulting from the Laplace equation between the apex and the two valves. Once the directions are computed, a local coordinate system is generated at each point of the mesh. Fiber orientation is finally estimated

for each cardiac structure after finding the most appropriate angles of the coordinate system to match histological observations.

3.2.2 Volumetric labeled mesh generation

Biventricular geometries used in this work were represented by patient-specific tetrahedral meshes built from the processing of computed tomography (CT) images. These images corresponded to nine patients with idiopathic OTVAs submitted for ablation procedure at Hospital Clínic de Barcelona. A multidetector CT ECG-gated study was performed on a 128 x 2 -slice CT scanner (Somatom Definition Flash, Siemens Healthcare, Erlangen, Germany). Images were acquired during an inspiratory breath-hold using retrospective ECG-gating technique with tube current modulation set between 50% and 100% of the cardiac cycle. The isotropic spatial resolution was 0.4 x 0.4 x 0.4 mm.

The biventricular geometries, including the outflow tracts and valve planes, were obtained from CT images using a semi-automatic segmentation procedure with region growing techniques available in the 3DSlicer [1] software. Subsequently, surface meshes were generated from the obtained binary segmentations applying the classical Marching Cubes method, which was followed by some post-processing steps (e.g. smoothing, labelling) performed in Blender [2]. Finally, tetrahedral meshes (∼80000 nodes and ∼400000 elements) were created using the iso2mesh [3] tool.

The next step of the methodology was mesh labelling, where different cardiac geometrical surfaces were identified to apply the Dirichlet conditions and construct the local reference system. These surfaces were the epicardium, the RV and LV endocardial walls, RV and LV apices and the four heart valves. These regions were easy to identify in the studied CT images, enabling the application of the OT-RBM in a wide variety of heart geometries. Mesh labelling is usually performed either manually, by tagging surfaces during the segmentation process [133], or using semi-automatic techniques [70, 134]. We used a semi-automatic approach where the apices and valve position were manually selected in CT images and endocardial and epicardial surfaces were automatically identified using ray/triangle intersection algorithms [135]. Rays were traced from the normal of every face of the surface mesh and intersections with other faces were computed. If intersections were found, the face was classified as endocardium; the rest

[1] https://www.slicer.org
[2] https://www.blender.org
[3] http://iso2mesh.sourceforge.net

were set as epicardium. Figure 3.2 (Step 1) shows the resulting mesh labelling for one of the processed biventricular geometries. Each mesh region is identified by a different color.

3.2.3 Local coordinate system

Cardiac fibers in finite-element meshes are represented in each node by an unitary 3D vector that is oriented in the preferential direction of the electrical propagation and mechanical contraction of the myofiber. Therefore, a local orthonormal coordinate system is needed to define the myofiber vector in all mesh nodes. The orthotropic axes of the reference system are the longitudinal ($\hat{e}_l$), transmural ($\hat{e}_t$) and local circumferential ($\hat{e}_c$) directions. Transmural and longitudinal directions can be defined by solving the Laplace equation using the corresponding surfaces as Dirichlet boundary conditions and computing the gradient of the solution, as in Bayer et al. [70]. In the OT-RBM these geometrical surfaces were the RV and LV endocardial walls, the whole biventricular epicardium, the RV and LV apices and the four cardiac valves (the tricuspid and pulmonary valves for the RV and the mitral and aortic valves for the LV). The local circumferential direction was defined as the cross product of transmural and longitudinal directions. Fiber orientation was then obtained by rotating the obtained vector $\hat{e}_c$ by a given angle α and β to match histological observations.

Transmural direction ($\nabla\Phi$) was obtained by solving the Laplace equation between the endocardium of each ventricle and the epicardium; subsequently the gradient of the Laplace solution (Figure 3.3a) was computed. Negative and positive values were correspondingly assigned to the LV and RV endocardium ($\Phi = -2$ and $\Phi = 1$, respectively) as Dirichlet boundary conditions. The epicardium was assigned to a zero value ($\Phi = 0$), thus allowing a discrimination between the two ventricles: positive and negative values were assigned to the RV and LV, respectively. These boundary conditions allowed to replicate findings from histological studies that affirm that two thirds of the septum belong to the LV and one third to the RV [1, 116, 130, 136]. Laplace equations and its gradients were solved using Elmer software [4].

The longitudinal direction ($\nabla\Psi$) was defined separately for each ventricle. This direction was the result of the weighted sum of the apico-basal ($\nabla\Psi_{basal}$) and apico-OT ($\nabla\Psi_{OT}$) gradients, defined individually in both

[4] https://www.csc.fi/web/elmer

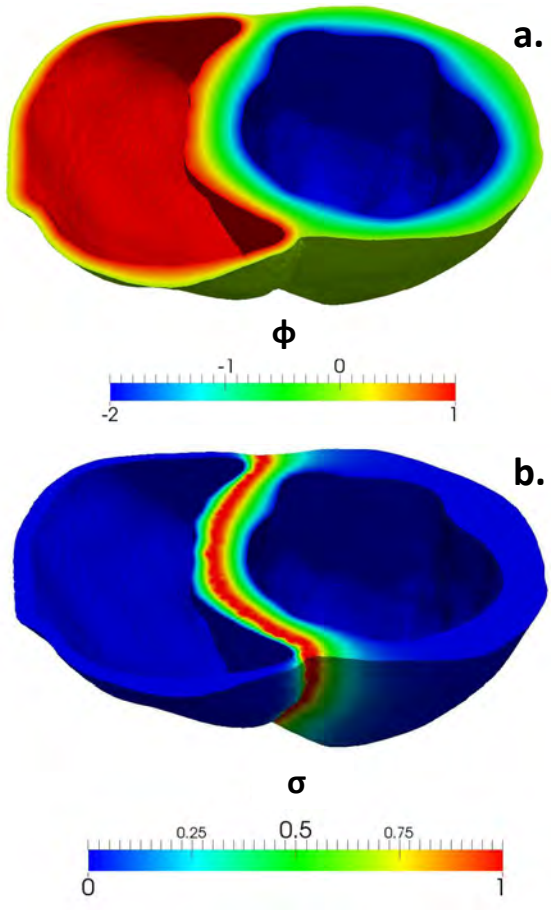

Figure 3.3: a) Example of a transmural map obtained by solving Laplace equation. b) Solution of solving the Laplace equation between the interventricular septal surface and the RV and LV endocardium

ventricles: $\nabla\Psi_{basal}$ considered the apex-mitral valve and the apex-tricuspid valve directions in the LV and the RV, respectively; $\nabla\Psi_{OT}$ followed the apex-aortic valve and the apex-pulmonary valve directions in the LV and RV, respectively. These directions were already described by Greenbaum et al. [3] and can be visualized in Figure 3.1 (dashed lines). The resulting longitudinal fiber direction for each ventricle was set as follows:

$$\nabla\Psi = \nabla\Psi_{basal} \cdot w + \nabla\Psi_{OT} \cdot (1 - w) \tag{3.1}$$

The sum of the apico-basal and apico-OT gradients was weighted by an intraventricular interpolation function w, which was computed in the RV by solving the Laplace equation between the apex ($w = 1$), tricuspid valve ($w = 1$) and pulmonary valve ($w = 0$), as shown in Figure 3.4. In the LV, the equation was solved involving the apex ($w = 1$), the mitral valve ($w = 1$) and the aortic valve ($w = 0$). In this way, we obtained a smooth distribution of values following the cardiac surface allowing to properly define the OTs and control the smoothness in fiber changes near the OT in different geometries.

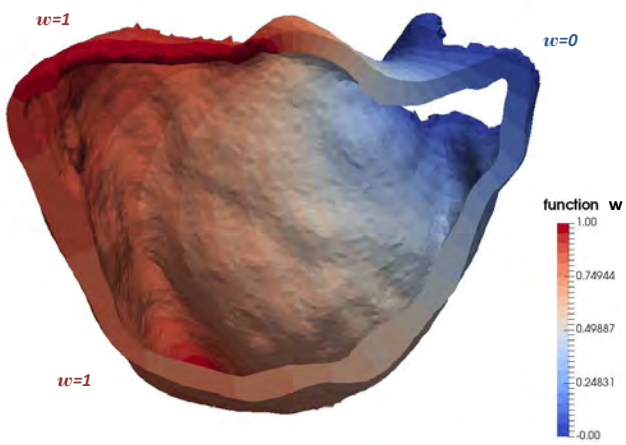

Figure 3.4: Example of intraventricular interpolation function w in the RV. The obtained values will guide the fiber interpolation between the apico-basal and apico-OT longitudinal directions within the ventricle.

Using the previously calculated gradients ($\nabla\Psi$,$\nabla\Phi$), the local coordinate system was set up for each mesh node, which is fully described with the

following vectors:

$$\hat{e}_l = \frac{\nabla\Psi}{\parallel \nabla\Psi \parallel} \qquad \hat{e}_t = \frac{\nabla\Phi - (\hat{e}_l \cdot \nabla\Phi)\ \hat{e}_l}{\parallel \nabla\Phi - (\hat{e}_l \cdot \nabla\Phi)\ \hat{e}_l \parallel} \quad \hat{e}_c = \hat{e}_l \times \hat{e}_t \tag{3.2}$$

3.2.3.1 Rotation of local coordinate system to match histological observations

Fiber orientation was finally obtained in every mesh node by rotating the local coordinate system to better match histological observations, as follows: 1) Vector $\hat{e}_c$ was rotated counterclockwise around $\hat{e}_t$ by an angle α; and 2) subsequently, vector $\hat{e}_c$ was again rotated counterclockwise around $\hat{e}_l$ by a transverse angle β . Note that the definition of angle α (angle with respect to the local circumferential direction) is not equivalent to the α helix angle defined in other histological studies or RBMs. The main reason is that our longitudinal direction is not always oriented in the apico-basal direction since it also has a component pointing in the apex-OT direction, which is the predominant one in the OTs. Far from the OTs, where the apex-OT component is negligible, the longitudinal direction only points towards the atrioventricular valves and therefore, our angle α and the helix angle match.

The first rotation was defined in each ventricle as a counterclockwise rotation of the vector $\hat{e}_c$ around $\hat{e}_t$ with an angle α:

$$\alpha = \alpha_{endo}(w) \cdot (1 - d) + \alpha_{epi}(w) \cdot d \tag{3.3}$$

where d is the transmural depth normalized from 0 to 1. The different values of α_{endo} and α_{epi} were chosen to replicate the following observations from several histological studies [1, 3, 113, 137]:

- Left ventricle (based on Greenbaum's observations [3]): $\alpha_{endo}(w = 1) = -60°$; $\alpha_{epi}(w = 1) = 60°$
- Right ventricle (based on Greenbaum [3], Ho [137] and Sanchez-Quintana [1]): $\alpha_{endo}(w = 1) = 90°$ (same as longitudinal direction); $\alpha_{epi}(w = 1) = -25°$
- Outflow tracts (based on Sanchez-Quintana [1]): $\alpha_{epi}(w = 0) = 0°$ (circumferential direction);$\alpha_{endo}(w = 0) = 90°$ (longitudinal direction)

The expression for the transverse angle, β, was the following:

$$\beta = \beta_{endo}(w) \cdot (1 - d) + \beta_{epi}(w) \cdot d \tag{3.4}$$

Values of the transverse angle were derived from several studies [2, 3, 138] as follows:

- Left ventricle:
  $\beta_{endo}(w = 1) = -20°$ and $\beta_{epi}(w = 1) = 20°$
- Right ventricle:
  $\beta_{endo}(w = 1) = 0°$ and $\beta_{epi}(w = 1) = 20°$
- Outflow tracts:
  $\beta_{endo}(w = 0) = 0°$ and $\beta_{epi}(w = 0) = 0°$

3.2.3.2 Septal configuration

The OT-RBM allowed to control fiber angles in the septum, since we previously divided our septal geometry into RV and LV using the transmural direction. Therefore, the intersection surface between both ventricles (i.e. interventricular septal surface) can be used to guide the interpolation of fiber angles in the septum. This is done by solving the Laplace equation between the interventricular septal surface and the RV and LV endocardium (Figure 3.3, b). The obtained values (σ) were used for forcing a smooth transition in both ventricles from the initial fibers in the septal surface (α_{septal}). Hence, the final expression for assigning the fiber angle in the septum, which could easily be modified to enforce continuity or a certain angle of discontinuity, was the following:

$$\alpha_{final} = \alpha \cdot (1 - \sigma) + \alpha_{septal} \cdot \sigma \tag{3.5}$$

3.2.3.3 Complex structures

The OT-RBM is capable of dealing with cumplex structures such as trabeculae, papillary muscles, moderator band or false tendons. Myofibers belonging to these structures present a longitudinal orientation along the long axis [3]. Since trabeculae information is not included in most of the

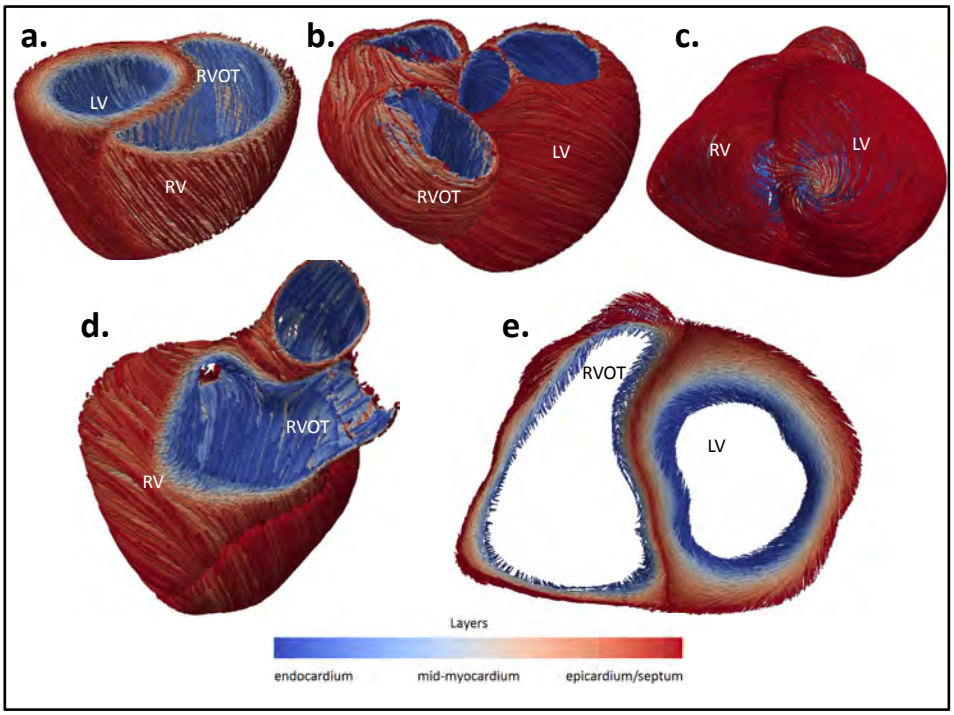

Figure 3.5: Fiber orientation obtained with the OT-RBM for different biventricular geometries and regions of the heart. LV: left ventricle; RV: right ventricle; RVOT: right ventricular outflow tract.

geometries obtained from CT or MRI imaging, we applied the OT-RBM to a detailed human heart geometry reconstructed from high-resolution MR images obtained by The Visible Heart® Lab. The volumetric mesh was created using an in-house mesher developed at the Barcelona Supercomputing Center (BSC). The OT-RBM assign the myofiber orientation to trabeculae by performing two extra steps. First, trabeculae are detected and then the specific fiber orientation is assigned in these structures. Trabeculae detection is done by calculating the parameter t using the previously obtained transmural gradient following the expression in Equation 3.6.

$$t = \begin{cases} \frac{\|\nabla\Phi\|}{T_{\|\nabla\Phi\|}}, & \text{if } \| \nabla\Phi \| < T_{\|\nabla\Phi\|} \\ 1, & \text{if } \| \nabla\Phi \| \geq T_{\|\nabla\Phi\|}. \end{cases} \tag{3.6}$$

Where $T_{\|\nabla\Phi\|}$ is a threshold value set as 0.1. An example of the detection of the trabeculae in two different patient geometries can be seen in Figure 3.6.

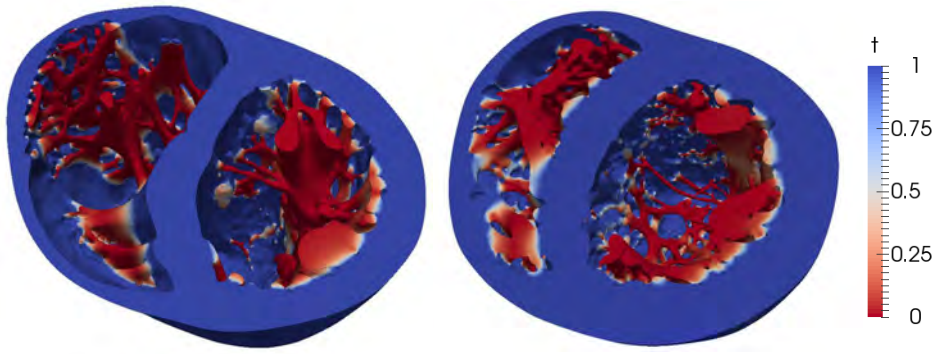

Figure 3.6: Example of trabeculae detection in two different geometries. Function t present low values in the trabeculae and a smooth transition towards the endocardium.

After detecting the trabeculae, fiber orientation is assigned to the trabeculation by means of the Equation 3.7. The expression guarantees a longitudinal direction of the fiber orientation along the trabecula and a smooth transition in the endocardium-trabeculation junction.

$$\alpha_{trab} = 90 \cdot (1 - t) + \alpha_{endo} \cdot t \tag{3.7}$$

$$\beta_{trab} = 0 \tag{3.8}$$

3.3 Experimental results

Results of applying the developed method to different geometries can be seen in Figure 3.5. They show a good agreement with histological data presented in Figure 3.1, especially in certain areas: RVOT fiber orientation (Figure 3.1a and Figure 3.5a, b, d); epicardial fiber configuration (Figure 3.1b, c and Figure 3.5b, c); and the transmural variation in LV fibers (Figure 3.1d and Figure 3.5e). The myofiber behaviour in trabeculae can be observed in Figure 3.7. The smooth transition between the trabeculae (red) and the endocardium (blue) can be appreciated in Figure 3.7a. Figure 3.7b shows a general view of the fibers in the LV trabeculae, especially in the false tendon. Figure Figure 3.7c compares the fiber generated in a high detailed geometry versus the obtained in a smooth one. A more exhaustive and quantitative evaluation of OT-RBM performance was conducted by means of three experiments, described below.

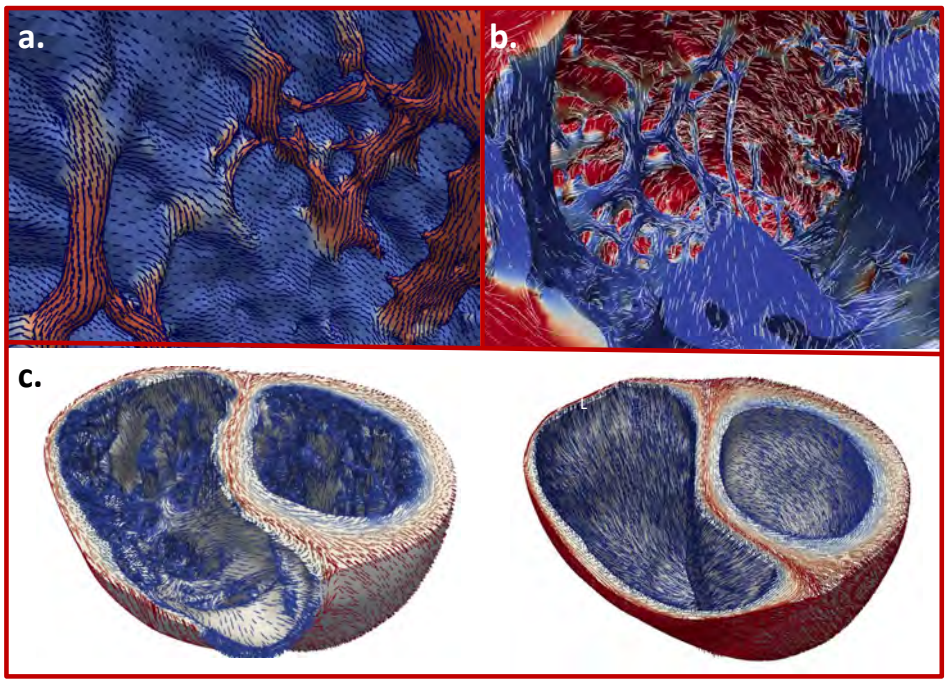

Figure 3.7: Obtained fiber orientation in different complex geometries. a) fiber orientation in the trabecula-endocardium junction. b) General view of fiber orientation in LV trabeculae. c) Comaparison of fiber orientation obtained in a high detailed geometry versus the fiber orientation of a geometry with smooth endocardium.

3.3.1 Experiments

Three experiments were designed and conducted to analyse the performance of the proposed RBM. In the first experiment we estimated the differences between fiber configurations provided by the OT-RBM and existing ones in the literature. Magnetic resonance imaging data from an ex-vivo human heart available at the Johns Hopkins database [5], which also includes fiber information from DT-MRI was used for this experiment. Differences were computed as the angle between fibers in each point of the mesh. Furthermore, mean angle differences were evaluated in different regions of the heart, dividing the LV into the 17 AHA regions according to the well-known description of Cerqueira et al. [139]. For the RV, a division in 15 regions based on the model proposed by Zhong et al. [140] was performed.

Since the previous geometry did not include detailed fiber information in the OTs, we performed a second experiment where OT fibers are indirectly

[5] http://cvrgrid.org/data/ex-vivo

compared. This experiment involved running electrophysiological simulations, including fiber orientation patterns computed with the OT-RBM and the Streeter-based one, on heart geometries from nine idiopathic OTVA patients. The simulated electrical propagation waves were then compared with clinical data from the OTVA patients, acquired during the ablation procedure at Hospital Clínic de Barcelona, Spain. Clinical data consisted of EAMs acquired by the CARTO 3 system (Biosense Webster, Inc., Diamond Bar, CA, USA). Early activation sites were manually identified by clinicians during the intervention. Characteristics of the isochrones (area, axis ratio) around the earliest activated point in the RV endocardium were also manually measured by clinicians after the intervention. Isochronal characteristics provide useful information to predict the site of origin (SOO) of the ectopic focus [29, 30]: if the longitudinal axis of the isochrones follows the apico-basal axis, the SOO should be in the RVOT (following the fibers in the OT); LVOT origins create more isotropic isochrones or with a larger perpendicular axis.

To simulate cardiac electrophysiology on patient-specific biventricular geometries we made use of the Mitchell-Schaeffer's electrophysiological model [141]. This model describes the transmembrane potential as the sum of a passive diffusive current and active reactive currents. It has two variables; the transmembrane potential u and a gating variable z that controls the depolarization and repolarization phases. Their evolution can be described by the following equations:

$$\begin{cases} \partial_t u = div(D\nabla u) + \dfrac{zu^2(1-u)}{\tau_{in}} - \dfrac{u}{\tau_{out}} + J_{stim}(t) \\ \partial_t z = \begin{cases} \dfrac{1-z}{\tau_{open}} & \text{if} \quad v < v_{gate} \\ \dfrac{-z}{\tau_{close}} & \text{if} \quad v > v_{gate} \end{cases} \end{cases} \tag{3.9}$$

Where the parameters τ_{in} and τ_{out} define the repolarization phase and τ_{open} and τ_{close} define the gate opening or closing depending on the change-over voltage v_{gate}. The term $D = d \cdot diag(1, r, r)$ is the anisotropic diffusion tensor, where d is the diffusion coefficient and r is the anisotropy ratio. This ratio produces a conduction velocity 2.5 larger along the fiber direction than in the transverse plane ($r = 1/2.5^2$). The tissue electrical diffusivity was adapted to obtain a longitudinal conduction velocity of 0.68 m/s. Finally, the term $J_{stim}(t)$ is the stimulation current at the SOO. Values of the parameters used in our models are summarized in Table 3.1

Table 3.1: Simulation Parameter Values

Parameter	Value
$\tau_{in}[ms]$	0.3
$\tau_{out}[ms]$	6
$\tau_{close}[ms]$	150
$\tau_{open}[ms]$	120
u_{gate}	0.13
$J_{stim}[s^{-1}]$	2000

Simulations were performed using the Mitchell-Schaeffer model implementation [142] in the SOFA framework[6] with a time step of 0.01 ms. The SOO was placed in different parts of the OTs, including the one found by the clinicians during the intervention. The isochronal area, i.e. the surface occupied by mesh elements in the RV endocardium that has been activated at a given time (10 ms in our case) after the earliest activated point, and the clinical ratio of the simulated isochrones were calculated in each case following the same protocol than clinicians when analyzing isochrones from the EAM data [29, 30]. The protocol implemented by the clinicians measures the longitudinal diameter of the isochronal map area, which was defined by a line parallel to the septal projection of the RVOT longitudinal axis (perpendicular to the plane of the pulmonary valve). The defined longitudinal axis specified the perpendicular axis of the early activated area (perpendicular direction of the longitudinal axis).

Finally, in order to demonstrate the influence of fiber orientation in electrophysiological simulations we carried out a sensitivity analysis by changing RVOT fiber orientation by different angles and performing simulations from two different SOO (RVOT and right coronary cusp). Resulting isochrones were evaluated and compared with clinical observations.

3.3.2 Comparison with other RBM and DT-MRI

Figure 3.8 shows the comparison of fiber distribution maps provided by the OT-RBM, the one based on Streeter (ST-RBM) [143], Bayer et al. [70] (BY-RBM) and DT-MRI on the ex-vivo human heart from the Johns Hopkins database. The top row of the figure shows the fiber configurations provided by the OT-RBM, ST-RBM and BY-RBM models (a, b, c, respectively). The bottom row shows the comparison between DT-MRI fibers and the

[6] http://www.sofa-framework.org

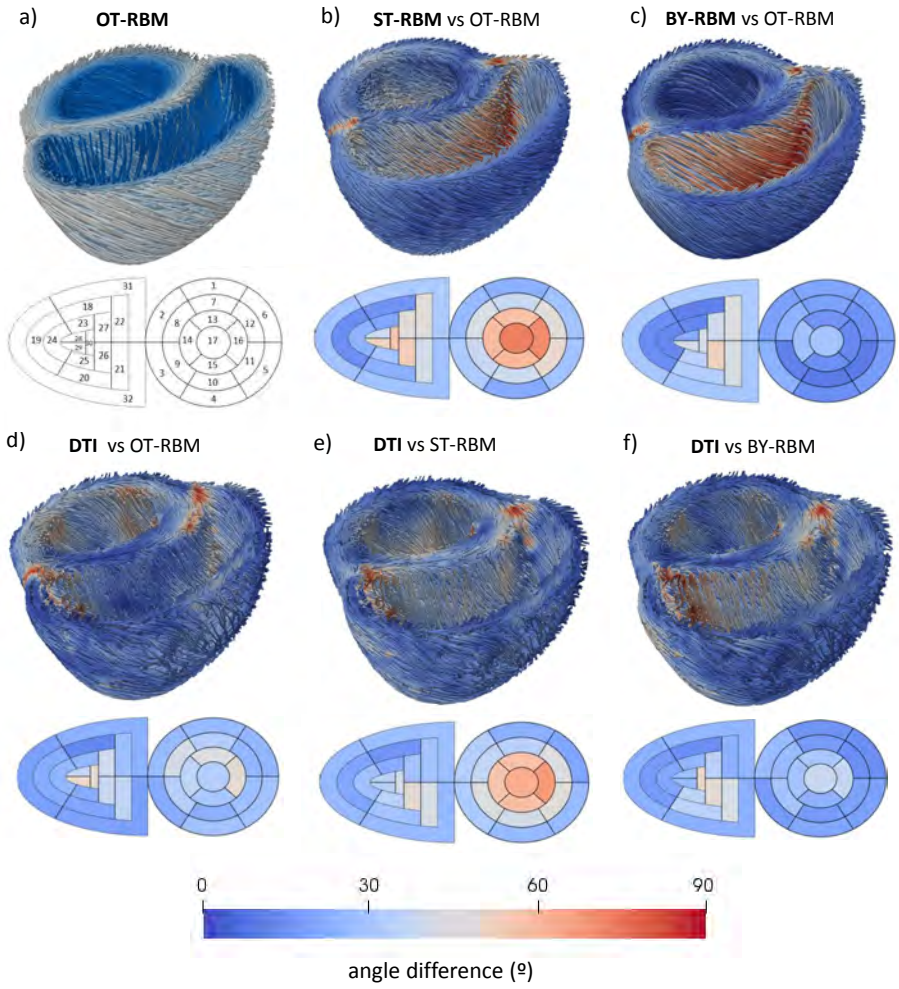

Figure 3.8: Top row: Fibers obtained using the OT-RBM (a) and angle differences (in degrees) with the ones obtained using ST-RBM (b) and BY-RBM (c). Bottom row: Angle differences between DT-MRI human fibers and OT-RBM (d), ST-RBM (e) and BY-RBM (f). Angle differences are shown in each case in a 3D mesh view and in a AHA plot with regional mean angle differences. For each geometry, name in bold indicates the represented fibers.

Table 3.2: Quantitative comparison of the angle differences presented in Figure 3.8 (b-f). Mean angle difference and standard deviation are presented for each region of the biventricular bulls' eye plot shown in Figure 3.8.

	angle ± sd (°)				
Region	**ST-RBM vs OT-RBM**	**BY-RBM vs OT-RBM**	**DTI vs OT-RBM**	**DTI vs ST-RBM**	**DTI vs BY-RBM**
1	23,0 ± 14,0	19,8 ± 12,9	26,6 ± 16,0	23,0 ± 15,0	16,3 ± 12,8
2	26,4 ± 18,6	18,3 ± 19,5	25,5 ± 14,8	32,9 ± 17,3	25,3 ± 15,4
3	31,6 ± 19,8	23,0 ± 24,5	22,0 ± 19,2	31,5 ± 17,9	17,0 ± 15,1
4	21,5 ± 12,2	15,3 ± 14,3	29,1 ± 13,4	25,8 ± 13,3	20,6 ± 14,0
5	28,6 ± 10,8	17,3 ± 14,4	29,5 ± 14,8	26,2 ± 10,8	19,6 ± 11,7
6	28,8 ± 11,1	18,8 ± 14,1	25,1 ± 12,2	20,0 ± 11,2	15,0 ± 10,9
7	39,0 ± 10,0	18,5 ± 10,0	33,1 ± 16,5	33,9 ± 10,0	17,6 ± 14,3
8	43,3 ± 16,8	23,4 ± 18,5	40,8 ± 17,3	37,5 ± 12,6	26,6 ± 14,6
9	38,8 ± 13,6	12,5 ± 12,1	32,7 ± 21,1	44,2 ± 13,0	28,5 ± 22,5
10	39,5 ± 12,7	11,0 ± 7,1	22,9 ± 15,2	41,4 ± 8,3	17,9 ± 17,1
11	48,9 ± 12,2	11,1 ± 7,8	27,2 ± 15,0	46,2 ± 9,1	18,7 ± 12,3
12	46,0 ± 11,3	14,1 ± 10,2	25,2 ± 12,9	43,9 ± 10,8	14,2 ± 10,5
13	57,6 ± 11,1	16,0 ± 9,5	44,3 ± 22,1	57,6 ± 13,8	30,3 ± 16,9
14	58,7 ± 14,7	27,7 ± 18,3	36,4 ± 20,2	55,4 ± 12,1	28,2 ± 20,1
15	59,9 ± 11,9	14,4 ± 10,8	30,5 ± 20,6	56,7 ± 7,8	23,1 ± 17,4
16	69,6 ± 10,4	13,3 ± 10,9	46,7 ± 21,4	66,5 ± 9,0	36,8 ± 16,1
17	72,5 ± 10,1	28,7 ± 24,0	33,5 ± 20,8	62,6 ± 10,4	39,1 ± 22,8
18	15,9 ± 8,1	12,5 ± 8,4	13,4 ± 10,6	16,0 ± 8,3	14,6 ± 8,8
19	15,1 ± 5,5	15,1 ± 11,7	21,6 ± 14,0	20,0 ± 11,6	16,9 ± 13,2
20	23,6 ± 7,4	33,0 ± 13,3	19,7 ± 18,3	29,5 ± 14,6	34,5 ± 16,5
21	41,2 ± 16,0	43,4 ± 22,9	36,4 ± 25,3	43,6 ± 17,9	42,7 ± 23,7
22	45,7 ± 25,6	44,6 ± 29,2	27,4 ± 17,2	28,8 ± 13,8	23,3 ± 14,0
23	20,4 ± 6,5	13,0 ± 6,4	24,8 ± 13,8	21,6 ± 13,6	24,9 ± 16,3
24	23,4 ± 5,3	13,0 ± 9,5	25,1 ± 16,3	26,9 ± 11,6	21,0 ± 13,6
25	29,0 ± 8,2	34,8 ± 15,2	21,2 ± 11,5	34,6 ± 7,7	35,3 ± 12,3
26	52,9 ± 17,2	51,9 ± 26,0	38,3 ± 25,0	47,0 ± 13,2	47,3 ± 21,3
27	45,3 ± 26,5	39,4 ± 28,5	40,4 ± 17,7	28,7 ± 15,9	34,0 ± 21,2
28	39,1 ± 15,1	22,2 ± 17,1	37,3 ± 20,5	34,7 ± 13,9	28,0 ± 14,1
29	52,0 ± 18,9	42,1 ± 27,6	48,0 ± 25,0	35,1 ± 7,4	25,5 ± 11,3
30	56,0 ± 21,3	40,8 ± 26,0	47,6 ± 22,9	42,0 ± 19,3	48,3 ± 21,4
31	31,9 ± 20,6	31,5 ± 21,2	23,4 ± 19,7	28,0 ± 20,8	24,5 ± 19,8
32	28,7 ± 19,2	30,7 ± 20,0	18,8 ± 15,7	26,0 ± 17,9	23,4 ± 17,9

different RBMs: OT-RBM (d), ST-RBM (e) and BY-RBM (f). Information about the mean angle difference projected into a 2D visualization of different regions of the heart is also included in the figure.

A quantitative analysis of these regional average angle differences is summarized in Table 3.2. As expected, the main angle differences (red colors

in Figure 3.8) between our model and the other RBMs are found in the RV endocardium, where we defined longitudinal directions from the apex towards the pulmonary and tricuspid valves. Fibers are more circumferential when generated with the other RBMs, when compared to histological data in this region. Low differences were found in the LV, especially comparing to BY-RBM ($< 20°$). The comparison with BY-RBM also presented low differences in the free wall of the RV ($< 15°$). Differences between OT-RBM and DT-MRI fibers are slightly larger in the LV ($\sim 30°$) but there is only one region, close to the apex, with high angle differences ($> 45°$, region number 16). The ST-RBM and BY-RBM methods, especially the former, also present difficulties for generating fibers close to DT-MRI data in the LV apex ($> 60°$ and $\sim 38°$ for ST-RBM and BY-RBM, respectively).

3.3.3 Electrophysiological simulations on OTVA biventricular geometries

Isochrone ratios and areas were estimated for the electrophysiological simulations with RVOT and LVOT sites of origin using fiber directions computed with the OT-RBM and the ST-RBM. A quantitative analysis of isochrone ratios provided by electrophysiological simulations with the OT-RBM and the ST-RBM with different SOO in nine different patient-specific biventricular geometries is shown in Table 3.3. It also includes the SOO identified by the clinician and the manually measured isochrone ratio during the intervention. For each origin, mean of isochrone ratios were the following (mean $\pm$ SD): 1.86 ± 0.22 and 0.57 ± 0.16 for RVOT-SOO using OT-RBM and ST-RBM, respectively; and 0.88 ± 0.3 and 0.9 ± 0.4 for LVOT-SOO, using OT-RBM and ST-RBM respectively. We can observe that the largest differences correspond to RVOT-SOO, where the OT-RBM successfully predicted a larger longitudinal direction than the transversal one, unlike ST-RBM.

The obtained isochrone areas were the following (mean $\pm$ SD): 1.5 ± 0.4 cm^2 and 1.4 ± 0.4 cm^2 for RVOT-SOO using OT-RBM and ST-RBM, respectively; and 5.5 ± 2.3 cm^2 and 5.6 ± 2.1 cm^2 for LVOT-SOO using OT-RBM and ST-RBM, respectively. Therefore, both RBM provided similar results in terms of isochrone areas, independently of the site of origin.

We also evaluated the potential of the OT-RBM as a tool to predict the SOO in OTVAs. An example of differences between isochrones obtained in the RV endocardium around the earliest activated point from the electrophysiological simulations with different SOO can be seen in the first column

Table 3.3: Clinical ratio (Longitudinal/Perpendicular diameter) of the 10 ms isochrones map area obtained from the simulated OTVAs using different SOO and RBMs. (RVOT: right ventricle outflow tract; RCC: right coronary cusp; LCC: left coronary cusp; OT-RBM: Outflow Tract extended rule based method; ST-RBM: Streeter-Based rule based method)

		Patient									
		P1	**P2**	**P3**	**P4**	**P5**	**P6**	**P7**	**P8**	**P9**	**All**
OT-RBM	**RVOT**	2.06	1.59	2.07	2.15	1.81	1.70	1.78	1.99	1.55	1.86±0.22
	LVOT-RCC	1.08	0.99	0.62	1.14	1.00	1.23	0.99	1.24	0.84	1.02±0.2
	LVOT-LCC	0.46	0.41	0.73	0.56	0.76	0.95	0.79	0.78	0.75	0.74±0.25
ST-RBM	**RVOT**	0.50	0.43	0.50	0.96	0.58	0.59	0.49	0.50	0.56	0.57±0.16
	LVOT-RCC	0.87	0.77	0.42	0.95	1.70	1.31	1.14	1.35	1.08	1.07±0.37
	LVOT-LCC	0.70	0.51	0.46	0.44	1.13	1.46	1.01	0.55	0.39	0.74±0.4
Clinical		0.54 (RCC)	0.81 (LCC)	0.73 (RCC)	0.67 (LCC)	0.82 (RCC)	0.64 (RCC)	1.63 (RVOT)	0.71 (RCC)	2.27 (RVOT)	

of Figure 3.9. For LVOT origin we generated simulations from the right and left coronary cusps (RCC and LCC, respectively). Substantial differences were found in the isochrone characteristics depending on the site of origin, mainly a higher degree of isochronal isotropy with a LVOT origin (RCC in the figure) than with a RVOT origin, where the longitudinal direction along the fibers is preferential.

We can observe that the OT-RBM contributes to simulate isochrone ratios well differentiated depending on the RV or LV site of origin. A dependent t-test between results in statistically significant differences between isochrone ratios from RVOT-SOO and RCC-SOO ($p < 0.001$) and from RVOT-SOO and LCC-SOO ($p < 0.001$), but not from RCC-SOO and LCC-SOO. Additionally, the OT-RBM successfully replicated clinical findings such as the preferential longitudinal direction in RVOT origins (isochrone ratios larger than 1.5 in P7 and P9), unlike the Streeter-based one (isochrone ratios around 0.6 in P7 and P9).

3.3.4 Sensitivity analysis

A sensitivity analysis was carried out to assess the influence of RVOT fiber orientation in the simulated RV isochrones, with different ectopic focus in the RVOT and LVOT (RCC origin). Fibers were changed as follows: 90° (chosen value in the OT-RBM), 0°, 45° and -45°. We also included fiber configurations provided randomly, with ST-RBM and BY-RBM; we extended ST-RBM and BY-RBM to work in heart geometries with OT, placing the basal plane boundary condition in the mitral and tricuspid valves. Figure 3.9 shows the simulated 10 ms isochrones in the RV and their corresponding clinical isochrone ratio, obtained with the different fiber configurations. Longitudinal and perpendicular ratios are displayed in yellow and green arrows, respectively. Only simulations guided by OT-RBM generated fibers were able to replicate the high clinical ratio (1.78) and correct isochronal orientation obtained with a RVOT site of origin. The simulated isochrones with a LVOT-RCC origin did not present large differences with respect to the chosen fiber configuration.

3.4 Discussion

The aim of this work was to develop a novel rule-based method (OT-RBM) for assigning myofiber orientation in heart geometries including specific in-

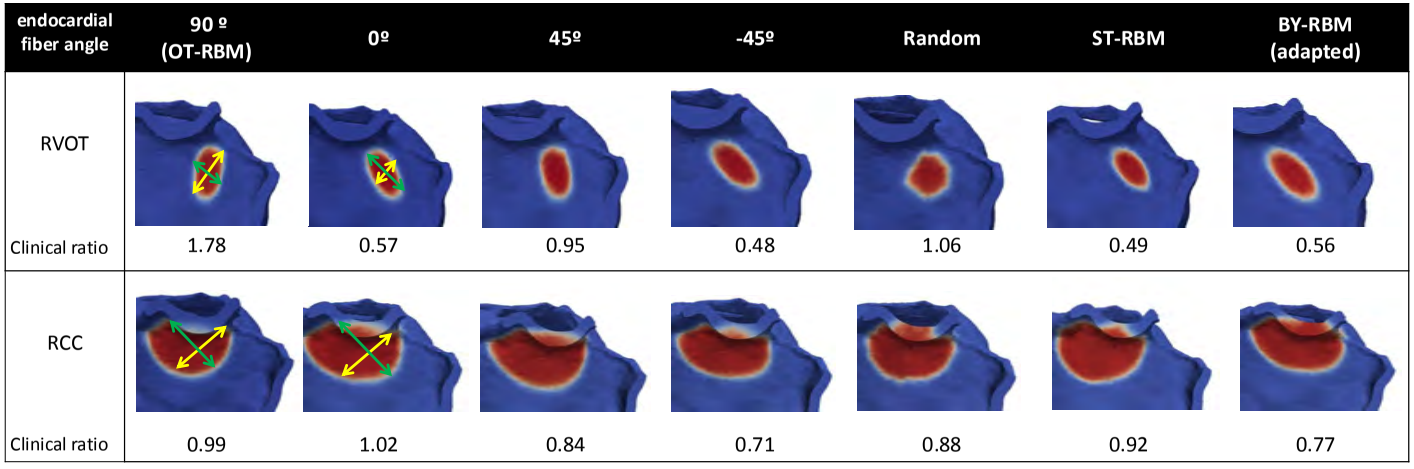

Figure 3.9: Sensitivity analysis results for the simulated right ventricular outflow tract (RVOT) and Right coronary cusp (RCC) origin isochrones and their corresponding ratios obtained by changing endocardial fiber orientation and running electrophysiological simulations.Yellow arrows indicate the measured longitudinal direction and green arrows the perpendicular one.

formation of the RV and OTs. This new method will allow performing *in silico* studies to better understand and predict the behaviour of cardiac pathologies where the RV and OTs have an important role. The developed OT-RBM is based on myocyte aggregate configuration observed on histological data. It includes the following novel features that were not available before: 1) treatment of each ventricle separately, which improves the individual fitting of fiber angles; 2) new definition of longitudinal direction ($\nabla\Psi$) based on histological descriptions [3, 137], which generate a new coordinate system allowing simple angle assignation to different regions of the heart; 3) fiber angles specific to the LV, RV, septum and OTs; and 4) addition of septal interpolation between the ventricles. These novelties make the OT-RBM flexible enough to assimilate fiber information from multimodal imaging (DT-MRI, histology, synchrotron data) and to work in a wide variety of heart geometries.

The proposed OT-RBM was compared with state-of-the-art RBMs, namely Streeter-based RBM (ST-RBM) and Bayer's RBM (BY-RBM). Differences on fiber configuration provided by the different RBMs can be visualized in Figure 3.8. As expected, the largest differences appear mainly near the RVOT, the RV endocardium and closer to the septum. For instance, ST-RBM and BY-RBM fibers are more circumferential that when generated with the OT-RBM, when compared to histological data in the RV. Interestingly, there were small differences ($< 20°$) observed between OT-RBM and BY-RBM fiber configurations in the LV. This suggests that longitudinal directions obtained with the apex-mitral and apex-aortic valve boundary conditions in OT-RBM are equivalent to the apex-base ones in BY-RBM in the LV. The LV valve geometrical configuration, where the mitral and aortic valves are quite close together is probably the main reason for the OT-RBM and BY-RBM similarities in the LV. Over all the studied regions OT-RBM fibers were closer to BY-RBM ones, comparing to ST-RBM results.

The different RBMs were indirectly compared running electrophysiological simulations involving the outflow tracts guided by the different RBM-based fiber configurations. Results of this comparison can be seen in Figure 3.9. One of the major contributions of the OT-RBM is that it greatly improved OTVA simulations when compared to clinical observations. The simulated longitudinal/perpendicular clinical ratios of the isochrones (Table 3.3 and first column of Figure 3.9) were in agreement with measurements made by clinicians during the intervention [29]. According to this study, clinical ratios for RVOT isochrones are 1.9 ± 1.2 ($n = 14$) and 0.79 ± 0.4 ($n = 23$) for LVOT isochrones. The OT-RBM isochrone clinical ratio for RVOT cases

in our simulation study (1.86 ± 0.22; see Table 3.3) was very close to the value measured by electrophysiologists. This agreement was possible due to the new distribution of fibers, especially in the RV and OTs, following histological observations. Other RBMs use simpler rules for generating fibers in these regions, obtaining unrealistic fiber configuration and, therefore, incorrect electric wave propagation and resulting isochrones (a ratio of 0.57 ± 0.16).

The influence of the cardiomyocyte orientation in electrophysiological simulations was further analysed in a sensitivity analysis (Figure 3.9). Isochrones obtained using the OT-RBM (90°) were the only ones showing good agreement with clinical observations from EAM [29, 30]. When the origin of the arrhythmia is in the RVOT (top row of Figure 3.9), the longest axis is in the longitudinal direction of the RVOT, which corresponds to axis ratios larger than 1.5. By contrast, the remaining fiber configurations showed an isochronal principal direction opposite to clinical observations, as observed in Figure 3.9. Obtaining simulated isochrones similar to clinical ones by only following histological observations, while being blind to any other patient-specific electrophysiological data, is a strong feature of the proposed method.

Finally, we also compared the RBMs with fibers obtained from DT-MRI data. An ex-vivo human heart geometry from Johns Hopkins database was used for the comparison. Unfortunately, fiber orientation data was only available below a certain basal plane, substantially below the outflow tracts and the valves, preventing a detailed evaluation of the OT-RBM. Despite this limitation, the comparison showed relatively small fiber angle differences in the LV (∼30°; Figure 3.8,d), except close to the apex, which is a complex region for all RBMs when compared to DT-MRI data. The small fiber angle differences between OT-RBM, BY-RBM and DT-MRI data suggests that they will have a similar behavior in simulations involving the LV [38, 70, 144]. In the RV, differences to DT-MRI fibers obtained with the OT-RBM are slightly lower than the ones obtained with other RBMs, especially in the septum, which has high relevance in the OTVAs. It is important to highlight that the OT-RBM is not designed to strictly follow DT-MRI data (neither in the LV nor in the RV), but guided by histology-derived information. As can be seen in histological pictures shown in Figure 3.1, fibers in the RV endocardium and the OTs present a different orientation compared to those obtained by DT-MRI. The OT-RBM has been parameterized to match as much as possible fiber orientation observed in histological data and based on cardiac anatomist observations; by design, RV and OT fiber

configuration from our RBM will necessarily differ from DT-MRI. Therefore, we cannot consider fiber angle differences between them as a conclusive index to assess the accuracy of the OT-RBM.

Another major outcome of our study is the improved realism of OTVA electrophysiological simulations when guided by OT-RBM fiber configurations since it could support electrophysiologists in the prediction of the SOO in OTVA patients. Frequently, LVOT vs RVOT prediction of SOO in OTVAs is a challenging task for electrophysiologists, especially in difficult cases where the LVOT and RVOT geometries are spatially close and their electrophysiological signals from the electrocardiogram cannot be distinguished. Several works [25, 27, 29, 30] proposed several indices to predict the SOO of ectopic focus and then reduce the time of and improve the success rate of interventions. Using OT-RBM based electrophysiological simulations on patient-specific geometries, we have been able to differentiate the SOO by measuring the longitudinal/perpendicular clinical ratio of the 10 ms isochrones. According to Table 3.3 there are statistical significant differences between RVOT and LVOT (LCC or RCC) origin isochrone ratios. Isochronal areas can also be used to predict the SOO in simulations (larger in LVOT cases) but cannot be consistently be measured in clinical routine. The previous findings show the potential of our modelling pipeline to be used as an additional pre-operative source of information to the clinician to predict the site of origin of ectopic foci.

4

In silico pace-mapping: prediction of left vs right outflow tract origin in idiopathic ventricular arrhythmias with multi-scale electrophysiological simulations

Abstract – The pre-operative identification of the site of origin (SOO) of outflow tract ventricular arrhythmias (OTVAs) is important to plan radiofrequency ablation procedures. Depending on the SOO, a different approach is needed. Although clinicians have developed several algorithms to predict left versus right ventricular origins based on electrocardiograms (ECG), their accuracy is still limited, especially in complex anatomies. The aim of this work is to predict the SOO using electrophysiological simulations on personalized geometries from OTVA patients. An *in silico* pace-mapping procedure was simulated in eleven patient-specific geometries, generating simulated ECGs from twelve clinically plausible SOO. Subsequently, the simulated ECGs were compared with patient ECG data obtained during the clinical tachycardia using a 12-lead correlation coefficient (12- lead ρ). The obtained simulations showed higher correlation coefficients in virtual sites close to the ablation points that stopped the arrhythmia. Additionally, the LV/RV ratio was calculated from simulations, which allowed to differentiate LV vs LV SOO (1.07 vs 0.93 $p < 0.05$ for 12-lead ρ). A more precise anatomical location of the SOO within a given outflow tract was also predicted, although accuracy was reduced. As a conclusion, the developed pipeline based on OTVA simulations demonstrates potential to become a useful pre-procedure tool complementary to standard ECG and support electrophysiologists in finding the SOO of complex ventricular arrhythmias.

This chapter is adapted from: Ruben Doste, Rafael Sebastian, Juan Francisco Gomez, David Soto-Iglesias, Alejandro Alcaine, Lluís Mont, Antonio Berruezo, Diego Penela and Oscar Camara. In silico pace-mapping: prediction of left vs right outflow tract origin in idiopathic ventricular arrhythmias with patient-specific electrophysiological simulations. Submitted.

4.1 Introduction

Outflow tract ventricular arrhythmias (OTVAs) are a type of idiopathic arrhythmia in which the site of origin (SOO) of the ectopic beat is located near the RV or LV outflow tracts (RVOT and LVOT, respectively). Patients with OTVAs can be managed with pharmacological treatment or by applying Radio-Frequency Ablation (RFA) at the SOO, which is the most common and effective treatment [12]. The estimation of the SOO location is an important step before RFA procedure since it affects the planning and timing of the ablation, the risk evaluation, and the catheter approach. When the SOO is estimated at the RVOT, the intra-cardiac catheter is introduced via the right femoral vein whereas in the LVOT cases the catheter reaches the LV through the femoral artery. Finally, in cases where there is a LV epicardial site of origin the region is accessed through the coronary venous system [13].

In clinical practice, electrophysiologists usually estimate the SOO after visual inspection of the 12-lead electrocardiogram. ECGs are composed by four main components: a P-wave, a QRS-complex, a T-wave and a U-wave. Each component is related with different electrophysiological stages of the heart, being the QRS-complex the most important since a great number of ventricular arrhythmias are detected by changes of the morphology on the QRS-complex.

To localize the SOO, pace-mapping is a common technique being used by electrophysiologists [31, 145]. It is possible to reproduce the clinical tachycardia characteristics by stimulating at different places of the heart. Therefore, if the obtained QRS morphology by pacing at a site matches well with the observed on the 12-lead ECG, the site is considered to be a potential ablation site.

RVOT origin has been reported to be the most common site ($\sim$75%) [15, 146, 147], although recent studies suggest that LVOT has an incidence in nearly 50% of the OTVA cases [17]. Epicardial SOO are 15% of the LVOT arrhythmias and usually come from the left ventricular summit [148]. Other anatomical structures where LVOT arrhythmias can emerge are the distal coronary sinus, the aortic root or the aorto-mitral continuity [13].

Unfortunately, estimating the SOO from the ECG pre-operatively is often a difficult task due to the complex anatomy of the outflow tracts, which leads to ECG patterns that may not provide enough information to discern

between left and right origins. Several studies have proposed algorithms to predict the SOO based on the standard ECG recordings of the patient, which are mainly based on the existence of transitions in the precordial leads and the amplitude of the QRS [23]. Some of these algorithm-derived indices include the R-wave duration index and R/S amplitude ratio index [24], the V2 transitional ratio [14], the V2S/V3R index [25] and the transition zone index [26]. These studies particularly stressed the relevance of having incorrect ECG lead placement since it would affect the morphology of the ECG signal and therefore the performance of the algorithms. Other studies [9, 27, 28] proposed to modify some of the standard precordial lead positions to improve the accuracy of the ECG-based predictions. In particular, moving leads V5 and V6 to more posterior locations (V7, V8, V9) [27, 28], or modifying leads V1 and V2 [9], seems to provide more information about the wave propagation and increases the effectiveness of the prediction. Some not ECG-based approaches have also shown relatively good accuracy in differentiating RVOT vs LVOT origin using indices such as the aorto-pulmonary valvular planar angulation [17] or the area and ratio of the 10 ms isochronal activation pattern [29, 30] obtained from the patient's EAM. However, these algorithms present several drawbacks. All the ECG-based algorithms show good results in their original publication, but their accuracy decrease when tested with different populations, especially when applied to patients with V3 transition, which are approximately the 40 % of OTVA patients [16]. A possible explanation for study discrepancies is that the measurement of these parameters highly depends on the clinician ECG analysis skills and presents high inter-observer dependence/variability; some QRS characteristics are easy to determine, however, calculation of other features where pattern recognition is involved becomes subjective and requires long-term expertise; some algorithms require numerous steps and can be severely affected by measuring errors during the index calculation. In addition, medications, preferential conduction of the depolarization wave or changes in heart morphology, among other factors, will affect the recorded ECGs [15]. Furthermore, the application of these algorithms is restricted in patients with paced rhythms or intra-ventricular conduction disorders [17] for which ECG morphology has been less analysed due to the limited amount of data available.

We hypothesized that personalized multi-scale electrophysiological simulations of the heart could provide added value to the electrophysiologists for the pre-operative non-invasive localization of the SOO in OTVA patients. We showed preliminary simulation results in Chapter 3, as part of

the validation performed for the developed OT-RBM [149]. Personalized electrophysiological simulations have already shown promising results to support clinical decision-making in cardiology [38, 39, 150, 151]. In order to achieve relevant clinical use, simulation of the ECG arises as a fundamental step since ECG is the most common non-invasive signal used in clinical practice. Although several works have been focused on performing ECG electrophysiological simulations, very few have tried to simulate and compare patient-specific ECGs [40, 106, 152, 153, 154]. Moreover, simulations where RV or OT have a crucial role are scarce due to the difficulties to get good anatomical and functional data in these regions, including myofiber orientation and EAM characterization.

In this work, we propose a novel framework to predict the SOO of OTVA by performing patient-specific electrophysiological simulations. The 3D anatomical model is constructed by segmentation and volumetric meshing the patient's CT images, together with regional tissue characterization (fiber orientation, tissue conductivity). Following, multi-scale biophysical models of cardiac electrophysiology are used to simulate the electrical activity from cell level to organ level. All the models include the heart and the torso, which allows to solve the forward problem of electrophysiology, and obtain the *in silico* patient ECG. With our computational model we can perform the pace-mapping procedure which is often used during ablation interventions by simulating surface ECGs from different ectopic foci and comparing them with the patient clinical ECG to identify the most likely site of origin. Beyond our research, only two recent works [155, 156] have attempted a similar simulation approach for the same clinical application, but it was applied to very few geometries (three and one, respectively) and without specific OT and RV-based RBM.

4.2 Methods

The methodology to simulate the *in silico* pace-mapping process is illustrated in Figure 4.1. All the simulations were run using the data of eleven OTVA patients obtained during a previous ablation procedure. Patient-specific biventricular geometrical models were created and the OT-RBM was used to assign proper myocyte direction in the OTs. A total of 12 electrophysiological simulations were carried out in each geometry by changing the SOO according to clinical reports [21]. Resulting potentials were propagated to the torso surface where ECG was calculated. Finally, after

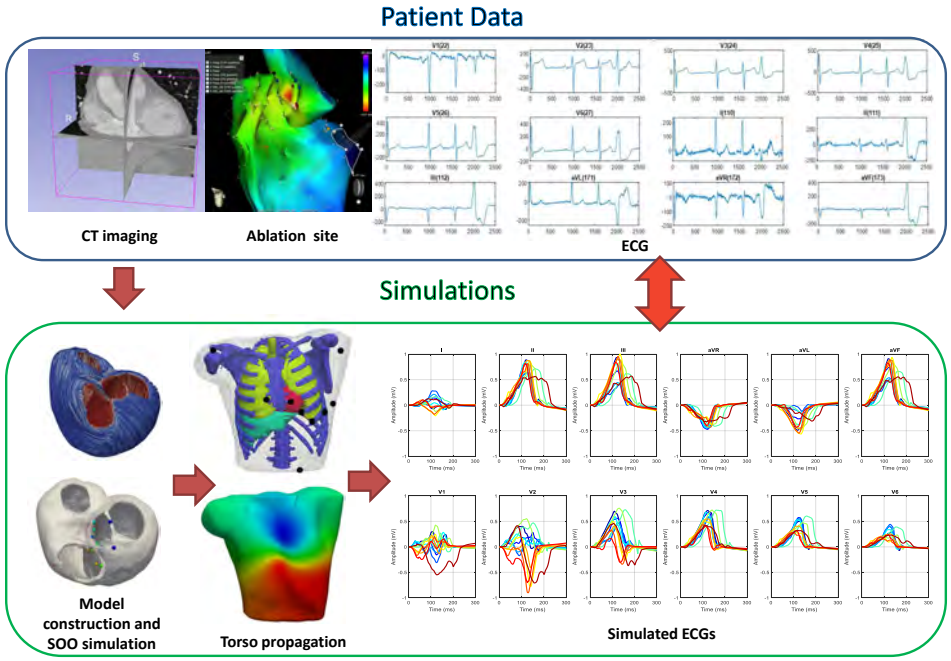

Figure 4.1: Scheme of the proposed methodology. Patient-specific geometries were created from medical computed tomography scans. Fibers were assigned using the OT-RBM algorithm (see Chapter 3). Electrophysiological simulations were run from different sites of origin (SOO) and electrocardiograms (ECGs) were calculated after the propagation to the torso surface. Finally, simulated ECGs were compared with the patient ECG in order to find the most similar pattern and therefore the best candidate for the SOO. Suggested SOO were then validated against the ablation site.

simulations were validated, simulated ECGs were compared with patient ECG in order to find the SOO that gave place to the most similar ECG.

4.2.1 Clinical Data

Patient-specific biventricular geometries were reconstructed from the processing of CT images that corresponded to eleven patients with idiopathic OTVAs submitted for ablation procedure at Hospital Clínic de Barcelona. A multidetector CT ECG-gated study was performed on a 128 x 2 -slice CT scanner (Somatom Definition Flash, Siemens Healthcare, Erlangen, Germany). Images were acquired during an inspiration breath-hold using a retrospective ECG-gating technique with tube current modulation set between 50% and 100% of the cardiac cycle. The isotropic spatial resolution was 0.4 x 0.4 x 0.4 mm.

All patients underwent a RFA procedure. The study was approved by the local ethics committee and written informed consent was obtained from all participants. EAM was acquired by CARTO 3 navigation system (Biosense Webster, Diamond Bar, CA) with a 3.5 mm irrigated tip catheter (NaviStar, Biosense Webster). Anti-arrhythmic drugs and beta-blockers were discontinued for 5 half-lives prior to the procedure. No patient received isoproterenol during mapping. During the procedure, 12-surface ECG and intracardiac recordings were obtained and displayed by an electrophysiology data acquisition system (Bard LabSystem, CR Bard Inc, Lowell, MA; or EP-Tracer, CardioTek, Maastricht, The Netherlands).

4.2.2 Biventricular model

The biventricular geometries were extracted from CT images using a semi-automatic segmentation procedure with the region growing techniques available in the 3DSlicer[7] and medInria[8] softwares. Surface meshes were generated from the binary segmentations using the Marching Cubes method [157]. After that, some mesh post-processing steps such as smoothing or face repairing were performed using Blender software[9] . Finally, an hexahedral volume mesh was generated with MeshGems-hexa software (Distene S.A.S., Bruyeres-le-Chatel, France)[10]. The generated meshes had an average of 3.5 million nodes and 4 million elements, with an average edge length of 0.38 mm.

Geometrical surfaces of the meshes were labelled in order to assign different tissue properties and cardiomyocyte orientation: the epicardium, the LV and RV endocardium, RV/LV apices and the four heart valves. We used a semi-automatic approach in which the apices and valve position were manually identified according to the CT images; the endocardial and epicardial surfaces were labelled using ray/triangle intersection algorithms [135]. Rays were traced from the normal of every face of the surface mesh and intersections with other faces were computed. If any intersection was found, the face was classified as endocardium; the rest were set as epicardium. Figure 4.2 (a) shows the resulting mesh labelling for one of the processed biventricular geometries. Each mesh region is identified by a different color.

Cardiomyocyte orientation was included in the model using the Outflow Tract extended Rule Based Method (OT-RBM) [149] detailed in Chapter 3. This RBM created detailed cardiomyocyte orientation in specific

[7] https://www.slicer.org
[8] http://med.inria.fr
[9] https://www.blender.org
[10] http://www.meshgems.com

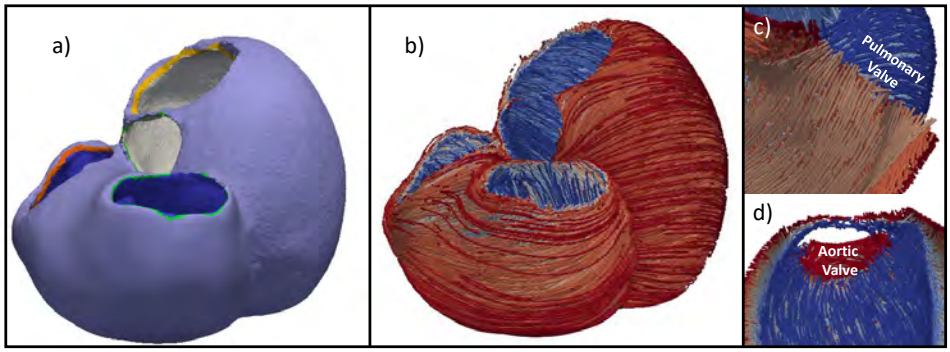

Figure 4.2: a) Labels assigned to the mesh surface (aortic, pulmonary, mitral and tricuspid valves, both apices, epicardium and right and LV endocardium). The different surfaces will be used to obtain the cardiomyocyte orientation with the OT-RBM algorithm (see Chapter 3). b) Streamlines showing the cardiomyocyte orientation created with the OT-RBM in one patient geometry. c) and d) Detail of fiber orientation near the pulmonary and aortic valves, respectively.

regions such as the outflow tracts, RV and the inter-ventricular septum according to histological information [1, 3, 29]. These regions play a key role in the OTVA simulations. In particular, OT cardiomyocyte configuration has longitudinal and circumferential directions in the sub-endocardium and sub-epicardium, respectively. This orientation highly differ from the myocyte orientation that is present in rest of the ventricle. Furthermore, there are also substantial differences between the RV and LV cardiomyocyte arrangement that need to be modelled individually. [1, 137]. An example of the obtained cardiomyocyte orientation in the epicardium as well as in the RV and LV OTs can be seen in Figure 4.2. The OT-RBM also provided some interesting labels in the geometrical interface between the two ventricles, automatically dividing the septum between RV and LV replicating some anatomical findings such as the myofiber transmural angle behaviour in the LV or the orientation in the septum [116, 136].

4.2.3 Torso model

A 3D torso model developed in previous works [40, 97, 105] was used to simulate Body Surface Potential Maps (BSPMs) that represent the electrical activity at the torso after the propagation of the electrical wave generated at the heart. The model was originally created from the data available at the online repository of the Scientific Computing and Imaging Institute (SCI) from the University of Utah [59]. The surface mesh can be found and freely

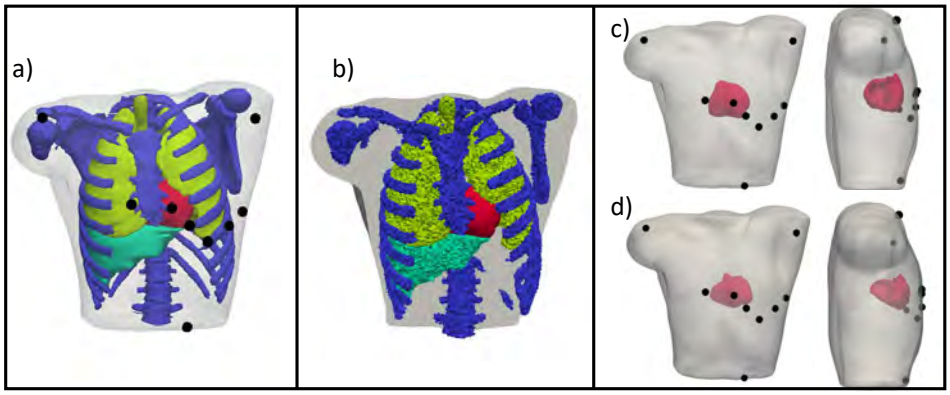

Figure 4.3: a) Anterior view of the surface mesh of the torso. The location of the electrocardiogram leads is represented by the black spheres. b) Resulting tetrahedral mesh of the torso. Each organ has a different conductivity and label: bones (blue), lungs (yellow), liver (cyan) and the ventricles (red). c) Anterior and lateral views of the heart placement in two different patients.

downloaded at the CoMMLab repository[11].

The torso mesh was conformed by the different surface meshes of the most relevant organs and structures for the electrical wave propagation from the heart (bones, lungs, liver, ventricles, blood pools of the ventricles, blood vessels and body contour), as can be seen in Figure 4.3. For each patient, the ventricle was replaced by the own patient-specific geometry. Finally, the tetrahedral torso volume mesh was generated with TetGen [158]. Surface mesh nodes were preserved during the meshing process, which included the surface of the inner organs such as the heart. In this way, the comparison between simulated BSPMs for different patients can be done point by point.

4.2.4 Electrophysiological Modeling

The electrophysiological behaviour of the myocardium was modelled using the human ventricular ionic model formulated by ten Tusscher et al. [88]. Transmural heterogeneity was added by defining three different action potential models for three different myocardial layers; endocardium, mid-myocardium and epicardium. Electrical propagation in tissue was modelled using the monodomain formulation and solved using ELVIRA software [95], which uses the finite element method to solve the monodomain equations of the electric propagation. Time step was set to 0.02 ms.

[11] https://commlab.uv.es/repository

Conduction velocity was obtained by tuning the longitudinal and traversal conductivities, considering axisymmetric anisotropy. Several simulations were performed on a tissue slab geometry (20 x 7 x 3 mm) composed of hexahedral elements with an edge length of ∼0.38 mm. A longitudinal conductivity value of 0.24 S/m and a anisotropic ratio of 0.19 resulted in a conduction velocity of 0.68 m/s along the cardiomyocyte orientation direction, which is consistent with values obtained experimentally in different works [159].

Electric propagation in the torso was considered isotropic; the different conductivity values assigned to each organ were extracted from the literature [59, 97]: lungs (0.039 S/m), blood (0.700 S/m), liver (0.028 S/m), bones (0.020 S/m) and the rest of the torso, conformed mainly by flesh and fat (0.239 S/m).

4.2.5 Simulation experiments

A total of twelve simulations were performed in each of the eleven patient-specific geometries. In each simulation the origin of the ectopic focus was changed according to the most common SOOs according to clinical studies [13, 21]. OTVAs were first simulated at the organ level (biventricular model) from which resulting transmembrane potentials were used to calculate the BSPM and ECGs.

4.2.5.1 Simulation of OTVA with different origins

Before simulating the OTVA, all models were stabilized by simulating 4 beats at sinus rhythm with a basic cycle length of 1000 ms. This stabilization was needed to homogenize the coupling of all the different cell models. Sinus activation pattern was obtained by stimulating 128 endocardial points in each geometry at specific times according to the activation pattern extracted from an EAM of a biventricular model previously developed [40]. In that model, sinus rhythm was generated by stimulating each point according to its associated local activation time of the EAM. A tailored adaptation of the Universal Ventricular Coordinates algorithm [160], which takes into account the outflow tracts, was used to map these 128 points to each of the eleven patient geometries.

Once the model was stabilized, a mesh node placed in the ectopic focus was stimulated, obtaining a 300 ms OTVA simulation of the ventricular

depolarization. For each patient, 7 SOO were placed in the LV and 5 were in the RV, as can be observed in Figure 4.5. The number and location of these points were chosen according clinical observations [13, 21]. A more detailed distribution of different SOO reported in these works can be seen in Figure 4.4. The seven LV-SOO (blue and green colours in Figure 4.5) were distributed as follows: 2 in the LCC and 2 in the RCC, 1 in the LCC-RCC commissure, 1 in the AMC (yellow-green point in Figure 4.5) and 1 in the LV summit (at the epicardium; turquoise-green point in Figure 4.5). The five RV-SOO (red, orange and yellow colours in Figure 4.5) were distributed as follows: 4 in the septal side of the RV, including two close (orange and yellow colours in Figure 4.5) and two away (red colours in Figure 4.5) from the pulmonary valve, as well as one in the free-wall (dark red colour in the top panel of Figure 4.5). In the end, a total of 132 simulations were carried out.

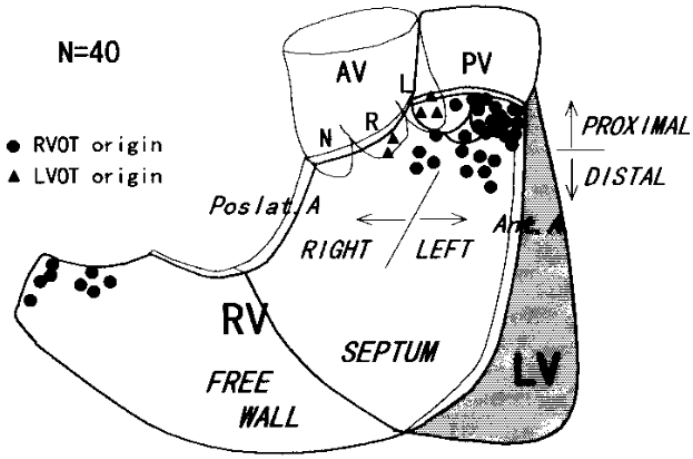

Figure 4.4: Reported sites of origin for left and right ventricular arrhythmias. Image adapted from Kamakura et al. [21]

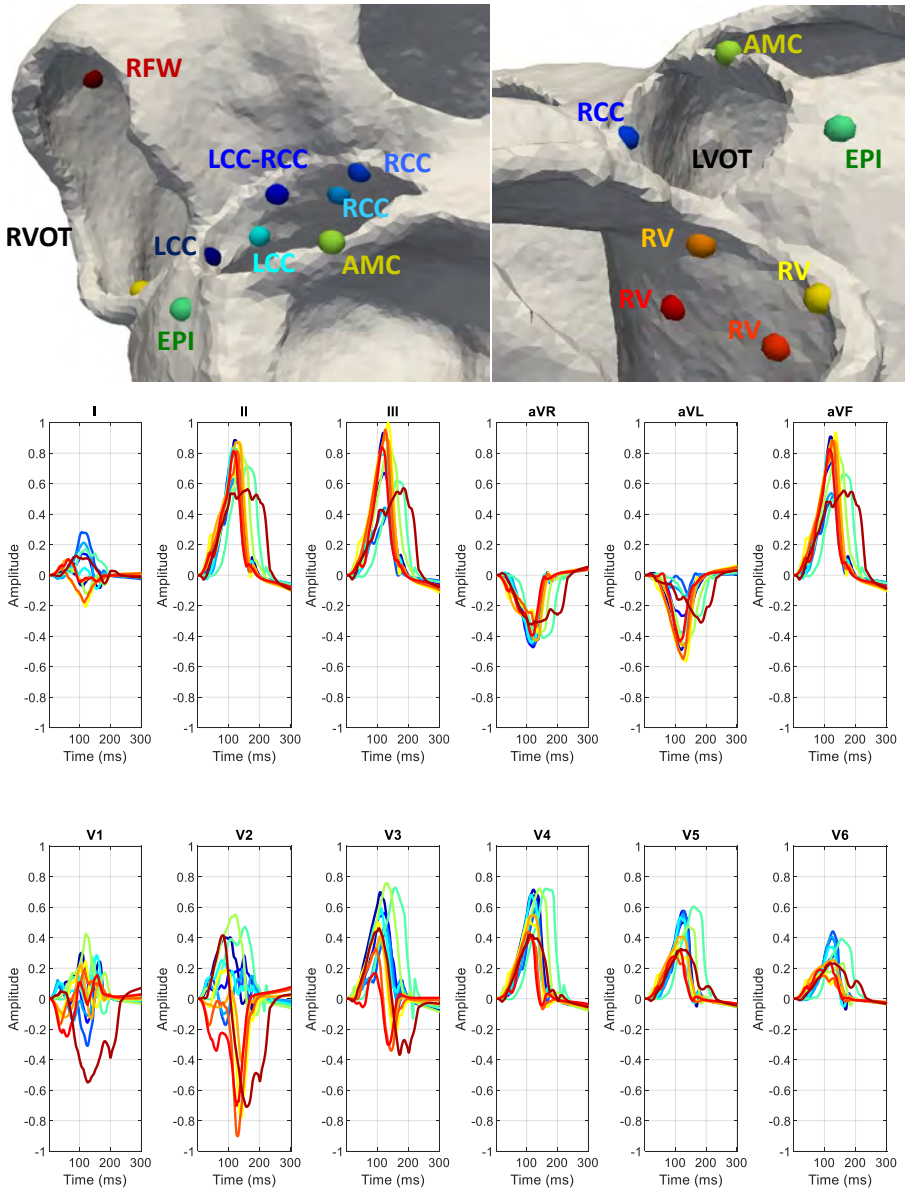

Figure 4.5: Top row: little spheres show the 12 different locations used as site of origin (SOO) in the simulations on a patient geometry (Patient 11). Seven SOO were located in the LV (blue and green colours): 2 in the LCC and 2 in the RCC (left and right coronary cusps, respectively), 1 in the LCC-RCC commissure, 1 in the AMC (aorto-mitral continuity) and 1 in the LV summit (at the epicardium, EPI). The five RV SOO were distributed as follows: 4 in the septal side of the RV, including two close (orange and yellow colours) and two distant (red colours) from the pulmonary valve, as well as 1 in the free-wall (RFW). Second and third rows: Simulated 12-lead electrocardiogram. Each signal color matches with the color of the point that represents the SOO.

4.2.5.2 Simulation of electrocardiograms

Body surface potential maps were obtained by computing the extracellular potential at the torso surface mesh nodes. ECGs were obtained by selecting the closest nine torso mesh nodes to the standard 12-lead ECG electrode location, as depicted in Figure 4.3. The electrical potential in each torso point was calculated as in [40, 97, 161], starting from the potentials simulated in the biventricular geometries with the ELVIRA software. First, potentials simulated in the the biventricular tetrahedral mesh were interpolated to the corresponding ventricular nodes in the hexahedral torso-based mesh. Subsequently, extracellular potentials were estimated in the ventricular nodes of the torso mesh by solving the diffusion term of the bidomain equation. Extracellular potentials were finally computed in the torso nodes using the finite element method to solve the Laplace equation, while applying Dirichlet and Neumann boundary conditions at the biventricular geometry-torso interface and the torso surface, respectively.

In addition, in order to include variability to the results and replicate possible lead misplacement [162], 13 different lead configurations were used for each simulation scenario, slightly varying each lead position between the different configurations within a range of 2 cm. A 12-lead ECG with a duration of 300 ms was then obtained for each SOO (12) and lead configuration (13) for each geometry (11), resulting in a total of 1716 simulated 12-lead ECGs.

4.2.6 Metrics and experiments for the validation of simulated ECGs

Simulated ECGs were quantitatively compared with patient-specific ECGs with the correlation coefficient (ρ) metric to assess the quality of the developed modelling pipeline. The expression of the ρ metric for two signals X and Y is given by:

$$\rho = \frac{\sum_{i=1}^{n}(X_i - \bar{X})(Y_i - \bar{Y})}{\sqrt{\sum_{i=1}^{n}(X_i - \bar{X})^2 \sum_{i=1}^{n}(Y_i - \bar{Y})^2}} \tag{4.1}$$

where signals are equally sampled with n points and $\bar{X}$ represents the average of all X samples. In our application, ρ was independently computed for each one of the 12-lead ECG signals. Additionally, we also estimated the 12-lead correlation coefficient (12-lead ρ) metric by averaging each individual lead-based ρ values using the Fisher Z-transformation [163]. This score, that has been previously proposed for ECG signal comparison [33, 34, 152], will return a number for every two 12-lead ECG comparison, being 1 when the waveforms are identical.

Signal processing was carried out using the MATLAB software (MathWorks, Natick, MA). All (simulated and patient-specific) ECGs were normalized in amplitude between -1 to 1, which corresponded to the minimum and maximum values of the 12-lead ECGs, respectively. Prior to calculating the 12-lead ρ metric, QRS complexes were manually extracted for each lead of the real patient ECGs. Then, signals were aligned by maximizing the value of the cross-correlation between the real patient signal and the simulated ones. Next, the 12-lead ρ metric was calculated for each simulation case. Since our simulations were carried out using 13 different lead configurations, only the maximum 12-lead ρ score was chosen among the (13) possible ones in each case. We also derived a LV/RV ratio in order to determine the LVOT vs RVOT origin in each patient: it was calculated by dividing the mean of the ρ values of all the LV-SOO simulations by the one corresponding to the RV-SOO simulations. A LV/RV ratio larger and smaller than 1 will indicate a LVOT and RVOT origins, respectively.

For validation purposes, the simulated 12-lead ECGs were initially qualitatively compared with patterns found in the literature for different SOO. We then used the correlation coefficient ρ to quantitatively compare all the simulated 12-lead ECGs against the real recorded ECGs. LV/RV ratio was derived from the 156 calculated 12-lead ρ in each patient (since 12 SOO and 13 lead configurations). Classification, i.e. an *in silico* based SOO assignment to each patient, was performed using the LV/RV ratio for LV vs RV SOO classification and the maximum 12-lead ECG ρ value for a more detailed location of the SOO. The assigned simulation-based SOO label was finally evaluated against the clinically found SOO, which was determined during the RFA intervention. The EAM acquired during the ablation treatment for each patient were used to analyse the local activation time (LAT) isochrones at different cardiac cycle time points and visually compared them with simulated ones. Statistical comparisons were made using a Student t-test; a p value ≤ 0.05 was considered statistically significant.

4.3 Results

In this section, the most significant results after applying the developed modelling pipeline on 11 patient-specific geometries described above are shown. First, we illustrate the variability present in the simulated ECG traces for different hearts (and a subset of SOO) and all SOO (and a subset of heart models). Then, some examples of simulated ECGs, representing the various SOO found in the studied database (i.e. RVOT, LCC and RCC of LVOT) are qualitatively compared with knowledge from clinical literature [13, 15, 23] that summarize the most relevant ECG features for SOO identification. Finally, recorded ECGs and LAT maps from EAM acquired during the RFA intervention of some patients are used to assess the accuracy of the simulated ECGs and electrical wave propagation, thus evaluating the whole modelling pipeline. All the simulations results for the eleven patients can be found in Appendix A.

4.3.1 Variability from different sites of origins and geometries

Figure 4.5 shows the simulated signals for each one of the 12-leads of the ECG that correspond to the 12 studied SOO (different colour for each SOO) in one of the analysed cases. It can easily be observed the variability of the simulated signals when having different SOO for the same biventricular geometry, in particular when qualitatively comparing signal patterns of LV vs RV origins (cold and hot colours, respectively). At the same time, some characteristics of the simulated signals that fit with clinical knowledge can be appreciated. The reader is referred to the excellent reviews of Anderson et al. [15], Enriquez et al. [23] and Lerman [13] for a summary of the existing knowledge on OTVAs that we use to compare our simulation results with. For instance, all leads of the RVOT RFW site of origin (red-brown colour in Figure 4.5) have a wider QRS complex compared to other SOOs, which has been extensively reported in the literature. Additionally, while some leads have polarity concordance (e.g. II, III, aVR, aVL, aVF), others are more heterogeneous, especially from V1 to V4, where precordial transitions differ depending on the SOO.

To better appreciate LV vs RV sites of origin, Figure 4.6 shows the same simulation results on the same case (Patient 11) but with simulated signals uniformly coloured according to ventricular origin: red and blue colours for

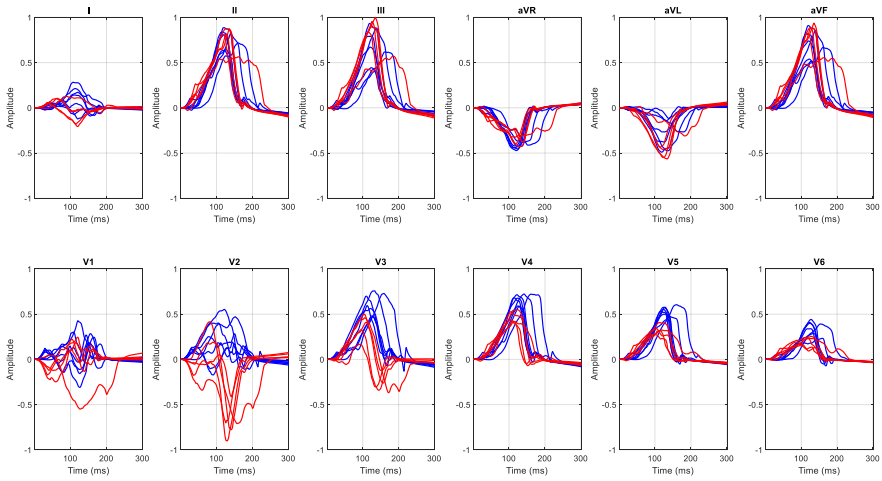

Figure 4.6: Influence of site of origin (SOO) on simulated ECG signals (fixed biventricular geometry). Twelve-lead simulated ECG signals with the 12 different SOO for the same patient (Patient 11) displayed in Figure 4.5. Red and blue colours represent right and left ventricular SOO, respectively.

RV and LV origin, respectively. In this figure, it is more evident the differences found in some key ECG leads that are precisely the ones targeted in clinical routine and in ECG-based algorithms to detect features helping distinguishing the ventricular origin of OTVAs, i.e. lead I to define anterior/posterior location and V1-V4 for precordial transition. For instance, it is straightforward to observe in Figure 4.6 that in V2 several LV-SOO signals (in blue) are already predominantly positive, which a clear sign of early transition in LV-based SOO, while most RV-SOO signals are still mainly negative. It is in V3 where some RV-SOO signals change polarity and in V4 where all transitions have already made the transition, matching the expected late transition of RV-SOO signals.

Figure 4.7 illustrates the variability of the simulated ECG signals for the SOO approximately located in the same locations but in two different biventricular geometries (Patient 5 and Patient 10). The results shown in this figure demonstrate the large impact of the heart geometry on the simulated ECG signals. For instance, we can observe different polarity in V1 lead for LV-SOO signals (Panel A in Figure 4.7), being mainly negative and positive for Patient 5 (blue colour) and Patient 10 (orange colour), respectively. In addition, one can notice that Patient 5 generally has a later precordial transition (V3) than Patient 10 (V2). On the other hand, the visual inspec-

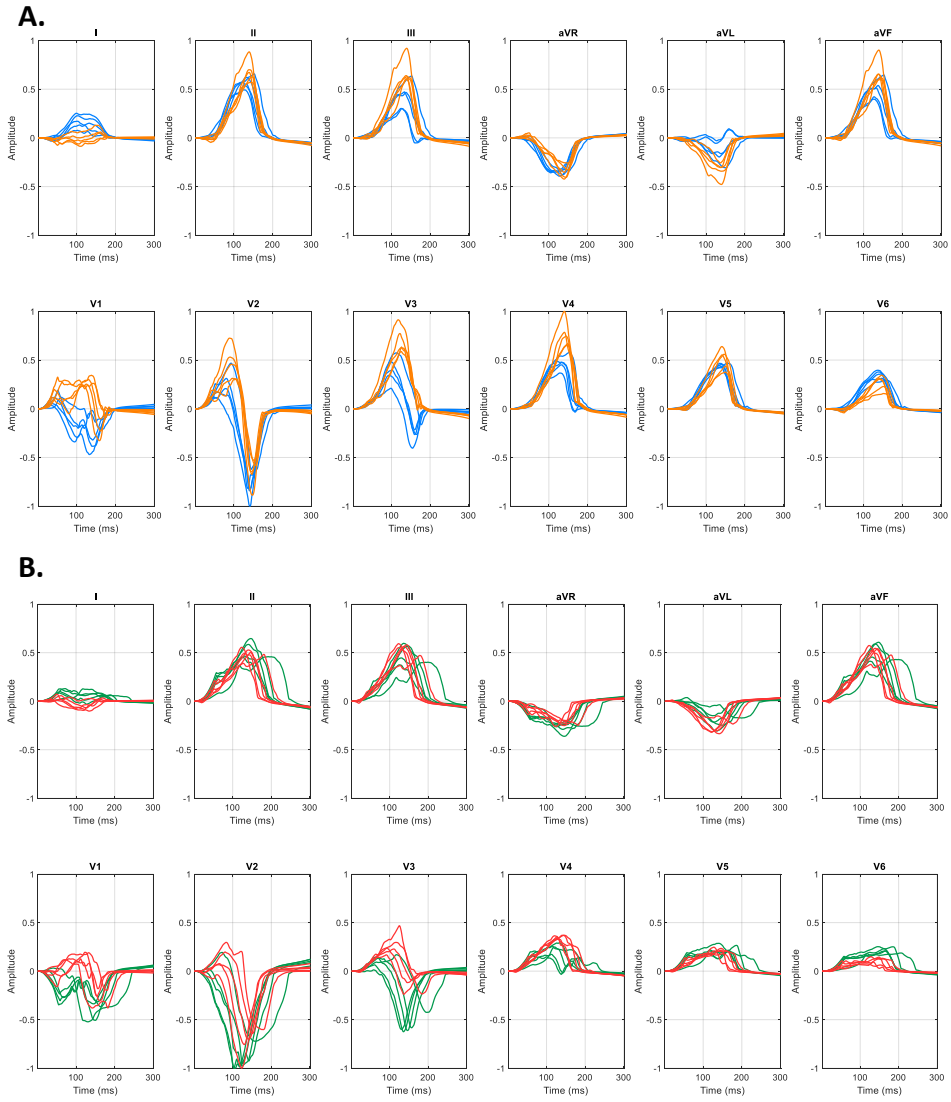

Figure 4.7: Influence of biventricular geometry on simulated ECG signals (fixed Site of origin, SOO). Twelve-lead simulated ECG signals with for two different biventricular geometries. A and B panels show right and left ventricular SOO, respectively. Blue and green ECG signals correspond to Patient 5 while orange and red are from Patient 10.

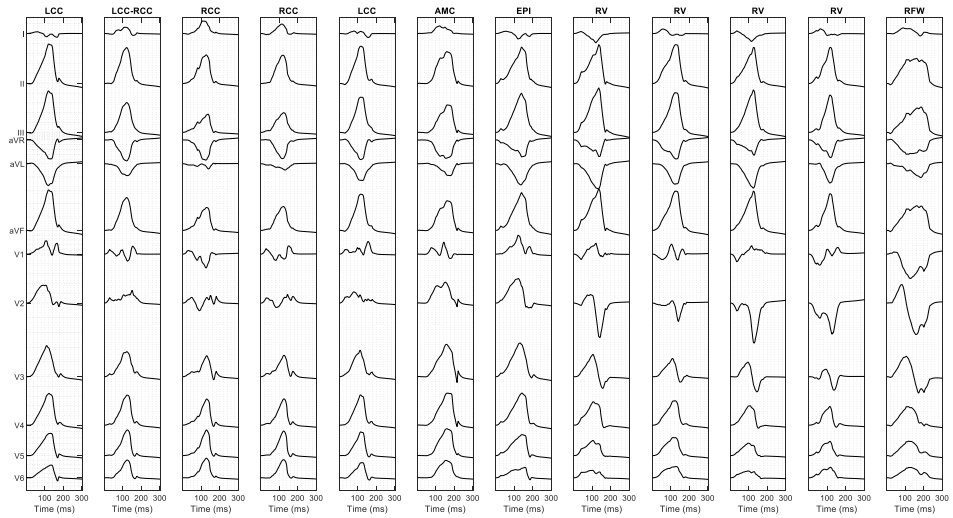

Figure 4.8: Twelve-lead simulated signals for the 12 different sites of origin of Patient 11. This type of visualization is inspired by artwork presented in Anderson et al. [15].

tion of RV-SOO signals (Panel B in Figure 4.7) shows several SOO with precordial transition in V3 for Patient 10 (red colour) but mainly in V4 for Patient 5 (green colour). Finally, we can observe a wider QRS complex in the RV free wall SOO for Patient 5 than for Patient 10.

4.3.2 Qualitative comparison of simulated ECGs with clinical literature

Figure 4.8 shows the 12-lead simulated ECG signals with the 12 different SOO corresponding to Patient 11, which will be used to assess the similarity with typical ECG features characteristic for each SOO described in the literature. Reader is referred to Appendix A for the complete visualization of simulated ECG signals for the 11 biventricular geometries studied in this work.

LCC: The simulated ECG signals with LCC SOO (columns 1 and 5 in Figure 4.8) present a multi-phasic (or notched M- or W-shaped) V1 lead, which is the main key morphological ECG feature for this SOO; moreover, they have narrower QRS complexes than RCC-SOO; other good characteristics according to literature include a large R wave amplitude, a negative

lead I and aVR/aVR waves as well as an early precordial transition in V1-V2.

LCC-RCC: This type of SOO is usually characterized by a QS notch in the downward deflection in V1, which is not easy to seen in the simulation of Patient 11 (second column in Figure 4.8)); clearer examples of this ECG feature can be found in other studied cases in Appendix A (i.e. Patient 2, Patient 4, Patient 5, Patient 9, among others); on the other hand, it correctly shows a transition in V2-V3 and a Rs wave in lead I.

RCC: The simulated ECG signals with RCC SOO (columns 3 and 4 in Figure 4.8) correctly have a precordial transition in V2-V3, slightly later than LCC-SOO in the same case; they also present a positive lead I, with tall R waves in II and III, a rS pattern in V1 and a broad R-wave in V2.

AMC: An AMC SOO is usually identified with a positive precordial concordance and no S wave in V6 as well as with a qR pattern V1, characteristics than appear in the simulated signal with this SOO in column 6 of in Figure 4.8; however, we need to be cautious on any ECG feature from the V1-V2 leads in this particular case since they are a bit noisy and thus difficult to interpret; it is then not very clear if we can confirm a V1 (or none) precordial transition in this simulated case, even if it seems so; finally a R or Rs pattern is seen in lead I, as expected.

Epi / LV summit: This type of SOO should present a V2 lead pattern break according to literature, i.e. an abrupt loss of R wave in V2 that cannot be appreciated in our simulations (column 7 in Figure 4.8); moreover, the expected rS/QS pattern is not found in V1; on the other hand, lead I is rightly negative, aVL is more negative than aVL and we can observe a larger R-wave in lead III compared to II, as described in the literature.

RV, anteroseptal RVOT: As expected, the precordial transition in this RV-based origin, occurs later than in LV-based SOO, in this case in V3; the obtained simulations for lead I for this particular SOO (columns 8 and 10 in Figure 4.8) are in agreement with the descriptions of Lerman [13] and Anderson et al. [15], showing a negative S pattern; in addition, we can appreciate a larger Q-wave aVL/aVR ratio, as suggested by Anderson et

al. [15]. A negative QS pattern in the aVR and positive R wave in the inferior leads are also obtained.

RV, posteroseptal RVOT: according to Anderson et al. [15], posteroseptal locations produce ECGs that are very similar to the ones that have an anteroseptal RVOT origin. The main morphological ECG feature to identify a posteroseptal RVOT origin, is a positive R wave in lead I, which is correctly captured in our simulations (columns 9 and 11 in Figure 4.8). In addition, as described by Enriquez et al. [23], posteroseptal RVOT ECG signals show a later precordial transition ($\geq$ V3).

RV free wall, anterior: Finally, the simulated 12-lead ECG signals corresponding to this SOO, shown in the last column of Figure 4.8, rightly present a late precordial transition in V4 and a wide QRS with inferior notching, as expected; inferior leads also have a smaller amplitude than the presented in other RVOT septal origins. It is a more unclear to confirm that in our simulations we can find other secondary ECG patterns sometimes found in this SOO such as having a negative lead I or a rS pattern in V1.

4.3.3 Comparison of simulated and recorded ECGs and EAM

The 156 simulated 12-lead ECG signals available for each one of the eleven patient geometries studied in our work were qualitatively and quantitatively compared with each patient-specific recorded ECG and EAM data. Figure 4.9 shows a visual comparison of the simulated and recorded ECGs for a couple of patients with clinically confirmed LV (Patient 2) and RV (Patient 7) site of origins, respectively. As in previous figures, ECG signals corresponding to RV and LV sites of origin are uniformly coloured in red and blue, respectively.

The visual inspection of recorded ECG data of Patient 2 in Figure 4.9 confirms the multi-phasic waveform in the V1 lead that is characteristic of LCC SOO. The LV SOO simulated (blue) curves also present negative and positive polarity curves in this lead when compared with RV SOO signals that are predominantly negative. The recorded ECG data clearly shows a V3 transition. The obtained simulations also provided a precordial

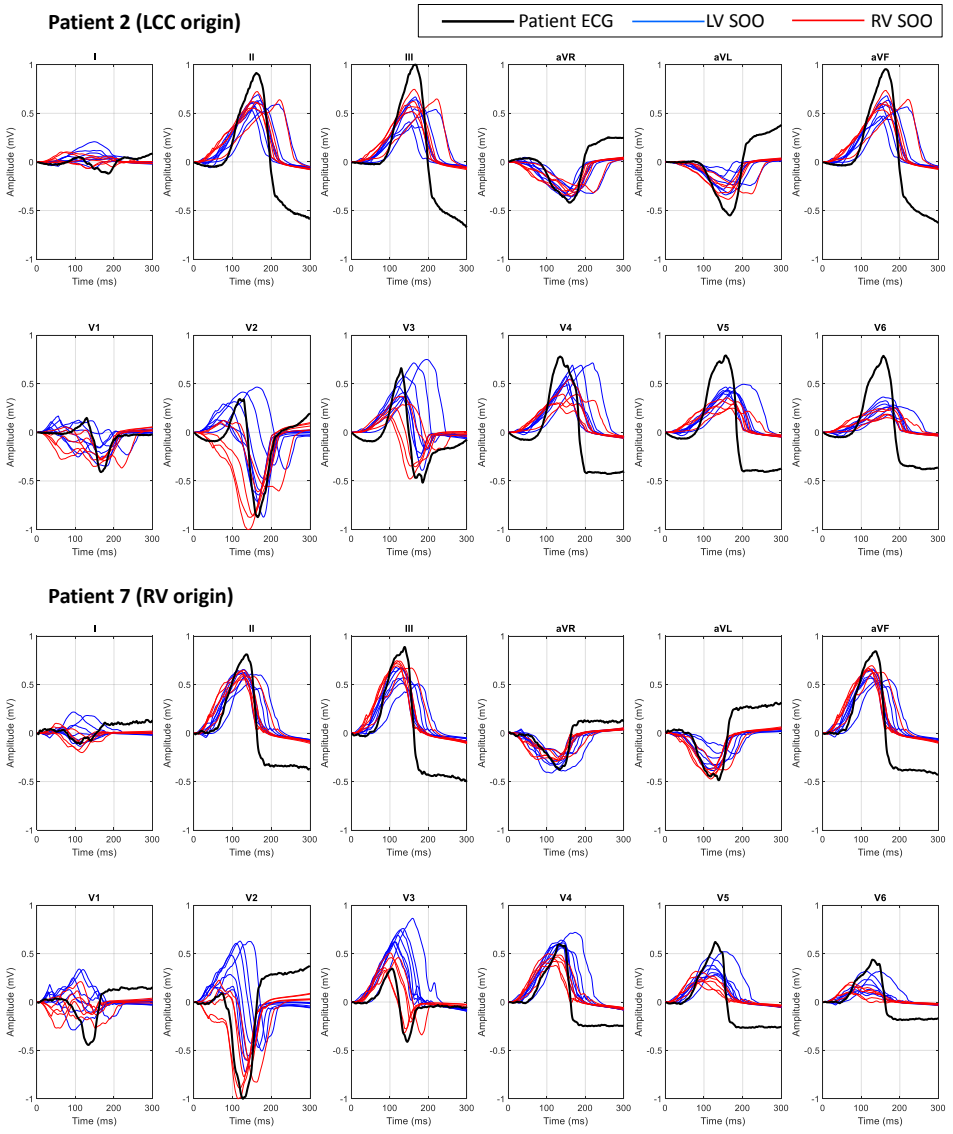

Figure 4.9: Comparison between the measured patient 12-lead ECG of the patient ectopic focus (black) and the simulated ECGs. Curves simulated with the origin in the LV are represented in blue color whereas RV SOO curves are in red. Two patients (Patient 2 and Patient 7) with different ablation sites are shown. Represented curves are not aligned temporally.

transition on LV SOO of V3 (blue colour), whereas RV-based ones (red colour) definitively changed polarity in V4.

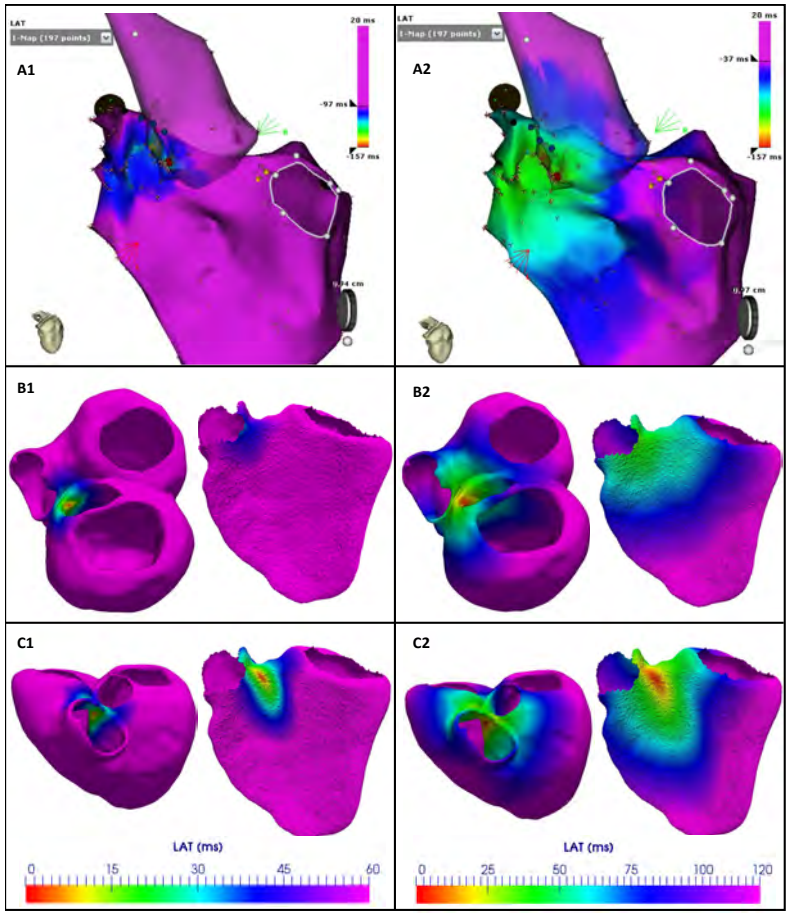

Figure 4.10: Comparison of measured and simulated Local Activation Times (LATs) isochrones in Patient 2, who had a LV site of origin (SOO) since it was ablated in the left coronary cusp (LCC). Red and pink colours indicate the earliest and the latest activated points, respectively. First column (1) shows the 60 ms isochrones whereas the second column represents the 120 ms isochrones. A) LATs measured with the electro-anatomical system during the ablation intervention. B)C) Isochronal map from electrophysiological simulations with a LCC and a RV SOO, respectively. It can be seen that LCC-SOO simulated isochrones are more similar to the measured ones during the intervention than the ones with RV-SOO.

The same conclusions can be drawn from the visual comparison of measured and simulated Local Activation Times (LATs) isochronal maps for Patient 2, which are shown in Figure 4.10. The figure depicts the 60 ms and 120 ms isochronal maps (left and right column, respectively) to represent the electrical wave propagation in the biventricular geometry obtained from the EAM acquired during the ablation treatment (top panel A) as well as the

equivalent simulations with a LV and RV SOO (middle B and bottom C panels in Figure 4.10, respectively. Red and pink colours indicate the earliest and the latest activated points, respectively. It can be seen that LCC-SOO simulated isochrones have more similar morphological characteristics than RV-SOO ones, notably the latter showing a more anisotropic behaviour due to longitudinal cardiomyocyte orientation in the RV pointing to the outflow tract.

The equivalent analysis of results obtained for Patient 7 (RV origin), also shown in Figure 4.9, confirms that the simulated ECG signals from the correct ventricular origin are more similar to the recorded ECGs than from the wrong ventricle. For instance, a better matching of RV-based curves (in red) with real ECG (black curve) can clearly be seen in lead 1 (negative polarity) than with LV-based ones. Moreover, the real ECG data suggest a precordial transition in V4 while simulated LV-SOO curves (in blue) are already predominantly positive in V3; several simulated RV-SOO curves correctly have significant negative polarity in V3, also suggestion a transition in V4. Finally, it can easily be appreciated a better matching of real data with RV curves (red colour), compared to LV ones (blue colour) in other leads such as V2.

The validation metrics presented in Section 4.2.6 help to quantify the accuracy of the developed modelling pipeline for the prediction of the ventricular origin of the ectopic foci in OTVAs. Table 4.1 shows the average and standard deviation of the 12-lead ρ between the recorded and the simulated ECGs for LV and RV SOO (Sim LV SOO and Sim RV SOO in the table) for each patient. Additionally, the LV/RV ratio that indicates the predicted ventricular origin (> 1 from the LV; RV otherwise) is also included. As the clinically-found SOO is shown in Table 4.1, it is straightforward to notice that the modelling pipeline correctly predicted the ventricular origin in 10/11 cases (91%). Only Patient 6 was incorrectly labelled from the simulations as RV-SOO when clinically it was found with a RCC-LV SOO. It needs to be pointed out that distinction between RV-SOO and RCC-LV SOO is one of the most challenging cases, also with real data. All patients presented significant differences between the average 12-lead correlation coefficient for RV origin vs LV origin ($p < 0.05$). In general, the LV/RV ratio of clinically-determined LV SOO was higher than those originated from the RV: 1.07 vs 0.93, respectively, $p < 0.05$).

In order to achieve a more precise location of the SOO, results of the maximum 12-lead ρ in each simulation were computed and are shown in Ta-

Table 4.1: Average and standard deviation of correlation coefficient (ρ) and LV/RV ratios from the simulated ECGs in each patient (P). Sim LV and RV SOO indicate left and right ventricular site of origin in the simulations, respectively. RCC-LV and LCC-LV indicate left and right coronary cusp ectopic foci, i.e. LV SOO. Highest values for simulated SOO of each patient are marked in bold. Bold values for the simulated LV/RV ratio indicate agreement between the predicted SOO from simulations and the clinical SOO.

	Clinical RCC-LV SOO				
	P1	P5	P6	P8	P9
Sim LV SOO	**0.83±0.02**	**0.81±0.04**	0.78±0.02	**0.87±0.07**	**0.91±0.02**
Sim RV SOO	0.75±0.02	0.71±0.02	**0.82±0.04**	0.84±0.05	0.89±0.02
LV/RV ratio	**1.11**	**1.15**	0.95	**1.03**	**1.03**

	Clinical LCC-LV SOO			Clinical RV SOO		
	P2	P3	P4	P7	P10	P11
Sim LV SOO	**0.88±0.02**	**0.88±0.03**	**0.86±0.03**	0.82±0.04	0.80±0.04	0.77±0.05
Sim RV SOO	0.84±0.04	0.85±0.03	0.72±0.03	**0.88±0.03**	**0.84±0.04**	**0.85±0.05**
LV/RV ratio	**1.05**	**1.04**	**1.19**	**0.93**	**0.96**	**0.91**

ble 4.2. Highest score per patient represent the most similar signal compared to the patient ECG and his marked in bold. Using a straightforward approach for classification based on the correlation coefficient values, i.e. labelling each cases only based on the highest ρ value per SOO, the modelling pipeline correctly predicts the clinical SOO in 6/11 cases (55%). More specifically, the 3 RV-SOO cases were rightly predicted (100%), while labels for the LCC and RCC SOO get somewhat confused: right prediction of LCC-SOO in only 1/3 cases (33%) and in 2/5 for RCC-SOO (40%). However, further analysis of the LV SOO, we can observe that the incorrect predictions are labelled from simulations as the closest possible anatomical SOO to what it was found clinically:

- Patient 1, labelled as LCC based on simulations but with a RCC SOO clinically;
- the opposite case for Patient 2;
- simulations suggest an AMC origin for Patient 3, which is anatomically very close to the clinically found LCC;
- we considered Patient 5 as wrongly predicted by simulations (LCC-RCC) since it clinically had a RCC origin, but it could arguably be classified as a correct case, due to real measurement uncertainties;
- very interestingly, Patient 6 (the only one missed with the LV/RV ratio) was tagged as posteroseptal RV from simulations, which is the closest possibility to the clinically determined LV-RCC SOO.

It needs to be pointed out that the incorrectly classified cases could have been better predicted with only a bit less naïf strategy looking also at the second best ρ value in each case. For instance, Patient 2 ρ values are practically the same (0.92) for LCC and RCC origins, while for Patient 4 (and for Patient 6), there is only a 0.01 difference between the AMC and LCC simulated SOOs (0.94 for AMC and 0.93 for LCC, which was the correct one).

Table 4.2: 12-lead Correlation Coefficient (ρ) values calculated for each patient (P) and each one of the 12 simulated (Sim) sites of origin (SOO) when compared to the recorded ECG. There are seven left ventricular (LV) SOO located in the left and right coronary cusps (LCC and RCC, respectively) as well as one in their commisure (LCC-RCC), the Aorto-Mitral Continuity (AMC) and in the LVOT epicardium. Additionally there are five right ventricular SOO : two in the antero and posteroseptal RVOT (RV_A and RV_P, respectively) as well as one in the anterior right free wall (RWF). Highest coefficient ρ of each patient is marked in bold. Sim refers to simulation.

	P1	P2	P3	P4	P5	P6	P7	P8	P9	P10	P11
Clinical SOO	RCC	LCC	LCC	LCC	RCC	RCC	RV	RCC	RCC	RV	RV
Sim LCC	**0.91**	0.92	**0.94**	0.93	0.85	0.81	0.83	0.85	0.90	0.87	0.82
Sim LCC-RCC	0.87	0.89	0.93	0.92	**0.86**	0.82	0.87	0.94	0.90	0.88	0.85
Sim RCC	0.86	0.87	0.88	0.91	0.79	0.82	0.88	0.94	0.91	0.91	0.88
Sim RCC	0.89	**0.92**	0.91	0.91	0.83	0.84	0.91	**0.95**	**0.93**	0.89	0.88
Sim LCC	0.90	0.92	0.93	0.93	0.85	0.84	0.88	0.88	0.92	0.87	0.82
Sim AMC	0.83	0.88	0.94	**0.94**	0.82	0.76	0.84	0.84	0.88	0.88	0.83
Sim EPI	0.85	0.91	0.92	0.90	0.83	0.79	0.81	0.85	0.84	0.84	0.81
Sim RV_A	0.88	0.91	0.90	0.81	0.76	0.76	0.88	0.80	0.88	0.88	0.87
Sim RV_P	0.82	0.81	0.90	0.85	0.73	0.81	0.88	0.86	0.89	0.89	0.88
Sim RV_A	0.87	0.87	0.88	0.82	0.72	0.80	0.89	0.84	0.88	**0.92**	0.91
Sim RV_P	0.84	0.83	0.88	0.85	0.73	**0.85**	**0.92**	0.89	0.88	0.90	**0.93**
Sim RFW	0.81	0.83	0.82	0.81	0.69	0.79	0.89	0.69	0.86	0.86	0.75
Predicted	No	No	Yes	No	No	No	Yes	Yes	Yes	Yes	Yes

4.4 Discussion

The modelling pipeline presented in this chapter for the *in silico* determination of the site of origin in OTVAs has demonstrated a good performance. It has potential to be used in the future, in combination with other computational techniques and indices, to support clinical decisions in this type of patients, in particular for preoperative planning of radiofrequency ablation treatment.

The obtained simulation results, thoroughly described for some illustrative cases in Section 4.3 and listed for all the studied patients in Appendix A, are

in close agreement with clinical descriptions reported in recent reviews in the literature [13, 15, 23] in most scenarios, which is quite noteworthy considering the complexity of the task, geometrical variability and necessary simplifications in the model. Performing the electrophysiological and electrocardiogram simulation study on eleven different patient-specific biventricular geometries and with 12 different SOOs, covering the most frequent OTVA anatomical locations, has never been done before since it is not obvious to obtain the necessary clinical data for model validation and the appropriate tools and knowledge to create realistic enough simulations. To get to this point, we needed to develop a modelling pipeline to process patient-specific data and generate the required finite-element meshes. More importantly, the good performance of the simulation results was only possible due to the development of the OT-RBM method presented in Chapter 3 to include realistic cardiomyocyte orientation in the RVOT and guiding the electrical wave propagation and thus, the ECG simulation. Some authors [10, 164] have confirmed good quality patient-specific geometry and OT fibers as key aspects for realistic electrophysiological and electrocardiogram simulations

Most key morphological ECG features for each SOO were well captured in the simulations, especially the correct SOO-dependent precordial transition. Still, some complicated and less well-defined SOO such as the AMC and the LV summit could be better simulated with our pipeline. Furthermore, in some cases certain leads presented artifacts preventing a reliable identification of ECG features (e.g. lead V1 in Patient 11, as it can be seen in Figure 4.8).

However, even with current limitations of the modelling pipeline, the proposed evaluation metrics such as the correlation coefficient ρ quantifying the similarity between simulated and recorded ECG signals showed a very good agreement between them. As a consequence, a simple index such as the LV/RV ratio proved its usefulness to determine the ventricular origin, with predictive values similar to state-of-the-art ECG-based algorithms available in the literature (see review in Anderson et al. [15], most of them around 80% - 90% of sensitivity). Obviously, to be properly compared with these algorithms, we need to apply the developed modelling pipeline to a larger database since we have tested in only 11 cases. If comparable, the proposed modelling pipeline should theoretically be more reproducible and robust to different inter-observer criteria than the current ECG-based morphological features that are mainly measured manually and prone to various interpretations.

The use of a simple approach to classify the simulated ECG signals for specific SOO resulted in poor prediction results (55%) due to misclassifications in LV-based SOO. Nevertheless, when carefully analysed, one can observe that wrong SOO labels corresponded to neighbouring, anatomically close, structures. Also, using only a slightly more sophisticated classification algorithm, considering beyond the largest percentage value, would already correctly re-classify most of the found errors. We should also be aware that there might be errors in clinically-defined labels due to uncertainty and current spatiotemporal resolution in electrophysiological measurements.

5

Predicting the site of origin in outflow tract ventricular arrhythmias with machine learning techniques trained on patient-specific electrophysiological simulations

Abstract – Identifying the site of origin (SOO) of outflow tract ventricular arrhythmias (OTVAs) is a key step to plan radiofrequency ablation procedures. Currently, electrophysiologists try to infer that information pre-operatively from the ECG, and intra-operatively from EAMs. In this work, we studied whether machine learning techniques can be used to predict the SOO. To cope with the lack of enough data for training such models, we studied the inclusion of biophysical simulations as training data. Therefore, we used simulated ECGs to train different machine learning algorithms and classify the different SOO between RV SOO and LV SOO. According to our results, the V3 lead is the precordial lead that provides more information for SOO localization, when combined with other leads; the combination of (V2,V3,V4,V5) leads provides the highest accuracy, 89%, when a k-NN model is used for classification. The obtained classification rates show that virtual databases with large number of simulated ECGs can be used as part of training of machine learning algorithms aiming at determining RV versus LV outflow tract origin.

This chapter is adapted from: Ruben Doste, Miguel Lozano, Guillermo Jimenez-Perez, Gabriel Bernardino, Alejandro Alcaine, Lluis Mont, Antonio Berruezo, Diego Penela, Oscar Camara and Rafael Sebastian. Predicting the Origin of Outflow Tract Ventricular Arrhythmias Using Machine Learning Techniques Trained with Patient-Specific Electrophysiological Simulations. In preparation.

5.1 Introduction

Machine Learning (ML) is a field of artificial intelligence that uses algorithms that learn from data and make predictions based on these data. Recently, the use of these algorithms in medical applications has increased considerably. One particular application where several successful cases have been reported is in the use of ML for ECG analysis, as recently reviewed in [107, 108]. In particular, machine learning techniques have been successfully applied to classify different ventricular arrhythmias [109, 110], to distinguish between normal heart beat and arrhythmias [111] or among all types of arrhythmias [165].

One of the main limitations for generalising the use of ML techniques on ECGs is the absence of large databases with good quality labelling for training. As a consequence, the number of investigated heart pathologies is substantially reduced. This problem has been overcome in other fields by generating large virtual populations of fully-controlled synthetic data using realistic simulations. Examples of this strategy can be found in the medical domain such as in Alessandrini et al. [166] to generate simulated ultrasound images to validate image processing algorithms. The same principle is also being used in non-medical domains for AI algorithm training such as the recent Open Source AI Habitat of Facebook[12]. Therefore, the generation of synthetic ECGs, properly validated with real data, can help to increase the number of data available. Electrophysiological simulations arise as one of the main techniques for carrying out these process, since several studies have reported successful simulations of patient-specific ECGs [40, 45, 97, 106, 154].

We propose the use of ML techniques on ECGs from outflow tract ventricular arrhythmia (OTVA) patients to guide their treatment. OTVAs are a type of tachycardia in which the site of origin (SOO) of the ectopic beat is located near the RV or LV outflow tracts (RVOT and LVOT, respectively). Radiofrequency ablation is the standard treatment and is usually performed guided by EAM data. However, the determination of the SOO before the ablation procedure is necessary to better plan the intervention, the risk evaluation and the catheter approach. In order to overcome this challenging step, clinicians have developed several algorithms based on manual feature detection from ECGs [13, 15], although they present several drawbacks: when they are tested in populations different from the one of the study their

[12] https://aihabitat.org

accuracy decreases; they require high skills in ECG analysis; and are sensible to the interobserver measurement variability. In addition, they cannot be applied to patients that present paced rhythms, intraventricular conduction disorders or structural heart disease [16]. The use of ML techniques for classification of the SOO between RV and LV SOO could overcome these constraints, specially at the tasks of quantifying the variations of the ECG leads or locating certain shapes or lead transitions in the ECG. In addition, identifying the area towards which more detailed pace-mapping should be directed would decrease the intervention time and the radiation exposure, facilitating a successful ablation procedure.

As shown in Chapter 4, simulated ECGs can be used to predict the SOO (RV vs LV). However, the modelling pipeline usually involves long computational times (image segmentation, model generation, use of finite element method simulations with heavy meshes, validation, among others) making them difficult to use in clinical practice. As a solution, new automatic pipelines and fast simulations procedures [167, 168] are being developed to accelerate this process. Another benefit of electrophysiological simulations is their ability to generate realistic simulated ECGs that can increase the OTVA ECGs databases. In clinical practice, datasets that contain a great number of OTVA cases, including the ECG and the ablated SOO, are scarce. Furthermore, creating these large datasets is a demanding task since collected data during intervention is rarely shared between clinical institutions and most of the obtained ECGs are recorded in paper. Finally, there are very few recordings for rare cases where ablation was performed in unusual SOO. For all these reasons, the training of ML algorithms using these data is a challenging process. Electrophysiological simulations that reproduce the behaviour of the OTVA patients ECG arise as a solution to overcome these limitations. We can train ML algorithms with a high number of simulated data that includes the variability among patient geometries, SOO location and lead placement variability. Similar approaches for training ML algorithms applied to premature ventricular contractions have recently reported successful results [155, 169].

In this work, we study the feasibility of building ML models that predict the SOO using simulated data for training. Data used in this study was obtained and evaluated in Chapter 4. Several supervised and unsupervised ML techniques such as self organizing maps (SOM), k-nearest neighbors (k-NN), support vector machine (SVM), random forest (RF) and multiple kernel learning (MKL) were used to evaluate the simulated and recorded clinical ECGs and their ability to predict the SOO (RV vs LV).

5.2 Methodology

We developed some experiments to evaluate the accuracy of a ML-based methodology to predict the ventricular origin in OTVA patients from their ECGs. Several ML techniques were tested for classification purposes and to better understand the relation between simulation results and real data. These techniques include supervised algorithms such as the classical k-nearest neighbors, random forest or support vector machine algorithms. When data are unlabelled is not possible to apply supervised learning, and an unsupervised learning technique is required. This method tries to find unknown patterns in the data to perform a clustering of these data to groups, and map new input data to these groups. Among the different unsupervised techniques we have used self-organizing maps and multiple kernel learning. In the following, a brief description of the employed ML algorithms and the set-up of experiments is given.

5.2.1 k-nearest neighbors (k-NN)

The k-NN algorithm is a supervised learning method that finds a predefined number (k) of training samples closest in distance to the new sample, and predict the new label by assigning the most frequent label. Distance can be determined by any metric, being Euclidean distance the most common. In this work, we used the algorithm implemented in the Scikit learn package [170, 171]. The parameter k was arbitrarily set to k = 1, i.e. effectively being the nearest neighbor algorithm.

5.2.2 Random forests

Random forests are an ensemble learning method for classification and regression that operates by creating a high number of decision trees at training time and returning the class that is the mode of the classes (classification) or mean prediction (regression) of the individual trees [172]. Random forests correct for decision trees' problems of over-fitting to their training set [173]. Decision trees are a popular method for various machine learning tasks. They have been extensively used for classification of ECGs [174], e.g. reducing false arrhythmia alarms [175], for detection of premature ventricular contractions (PVCs) in patients [176], and for assessing the probability of

arrhythmia recurrence and mortality in patients after ventricular tachycardia (VT) ablation [177]. The random forest algorithm employed in this thesis was again the one implemented in the Scikit learn package, with 100 defined trees.

5.2.3 Support vector machine (SVM)

SVMs are supervised ML methods that use learning algorithms to perform data classification and regression. SVM algorithms use labelled training samples to build a model that assigns the new input data to different categories. The objective of the SVM algorithm is to construct a hyperplane or a set of hyperplanes in a high- or infinite-dimensional space that can be used for classification, regression, or other tasks like outlier detection. SVMs have successfully been used to classify ECGs of patients into different types of arrhythmia [178, 179], or to improve the detection of RFA targets by using model-based augment features to train classifiers [180]. In general, the performance of the classifier mostly depends in the features extracted from the signals that are used to train the SVM model [181]. In this work the SVM implementation available in the Scikit learn package wa used, with a Gaussian radial basis function as kernel and a parameter $nu = 0.25$. This parameter is both an upper bound on the fraction of training errors and a lower bound of the fraction of support vectors.

5.2.4 Self-organizing maps (SOM)

A SOM is a type of artificial neural network that is trained using unsupervised learning (i.e. samples are not labeled) to create a low-dimensional, discretized representation of the input space of the training samples, called a feature map [182]. SOMs apply competitive learning, as opposed to the error-correction learning that is used in other types of artificial neural networks. In addition, they use a topological neighborhood function to maintain the topological relations of the input space, as can be appreciated in Figure 5.1. They have been used for obtaining visual information among four important groups of patients: ventricular fibrillation, ventricular tachycardia, healthy patients and other anomalous heart rates and noise using as input features extracted from ECGs [183]. Other studies

have also used SOM to discriminate premature ventricular contraction arrhythmias [184], or to detecting fatal cardiac arrhythmia in implantable cardioverter-defibrillators [185].

In this thesis, two different SOM were trained with all the simulated samples of one class: one SOM with all the RV SOO signals and the other with all the LV SOO signals. All signals were previously temporally aligned using as reference their absolute max value. An example of the structure of the SOM used in the work can be seen in Figure 5.1. The SOMs were implemented usign the MiniSom package [13]. The output layer of the SOMs were conformed by a grid of 8×8 neurons, the initial spread was defined by a Gaussian as neighborhood function with $\sigma = 0.48$ and an initial learning rate (parameter that controls the size of the weights during the learning process) of 0.25. These values were obtained after a sensitivity analysis on these parameters, testing the SOMs with different values to make sure that the algorithm reached sufficient resolution and accuracy. A quantization error (QE), which is a measure of variance associated with the final weights of the neurons after the training process, was calculated in each SOM. Since both SOMs were defined with the same parameters, the resulting QE represents the average distance between each test data and the best matching signal, which can be used to determine the best classification [186]. The best match of the two SOMs that had the smallest QE with respect to the input signal was set as the winner class.

5.2.5 Multiple kernel learning (MKL)

The unsupervised version of the MKL algorithm is able to handle heterogeneous descriptors and reduce their complexity into a low-dimensional space that has one less dimension that the total number of evaluated signals. However, only the first few dimensions, which generally capture the most significant characteristics of the data are usually evaluated. The MKL algorithm that we used in this work was validated in previous works [187], to detect phenotypes of patients prone to a better response to cardiac resynchronization therapy. In our application, the MKL was used to better explore and understand the differences between the simulated and the real signals as well as their ability to differentiate between RV and LV SOO. The MKL algorithm was trained using a combination of both the simulated and the real patient QRS-complex portions of the 12-lead ECG signals.

[13] https://github.com/JustGlowing/minisom

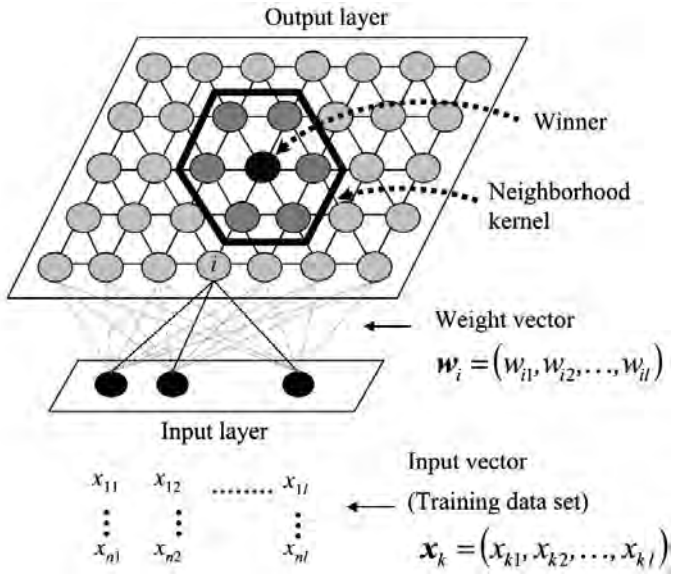

Figure 5.1: Structure of the self-organization map used in this work. Image adapted from Kinoshita et al. [185].

5.2.6 Experiments

ML training was performed using some of the simulated data described in Chapter 4. We initially simulated 132 OTVA ECGs in 11 patient geometries, which were augmented by calculating the ECGs with slightly different lead placements. After validation with real data (see Chapter 4), we discarded simulated ECG signals corresponding to the patient that was not correctly predicted with the modelling pipeline (Patient 6). Therefore, considering the 13 different lead configurations generated for each patient, a total of 1560 simulated 12-lead ECG signals (120 without data augmentation) were finally introduced to the algorithm training.

The classification test dataset was constituted by 35 $\times$ 12-lead ECG signals from OTVA patients that underwent ablation in different SOO. The QRS complex of these signals was extracted manually in order to improve the comparison against simulated data. The clinical SOO was determined by an expert electrophysiologist from the inspection of EAM data available for each patient, evaluating the final ablation points that terminated the arrhyhthmia.

The accuracy of the different algorithms to correctly classify the 35 test patients was evaluated. First, we studied the relevance of each individual

lead in the classification and the combinations of leads giving the best results when applied on simulated (80 % training, 20 % validation) and real data. Then, we studied and visualized the different relations between the simulated and real signals as well as their ability to properly distinguish between RV and LV SOO by applying dimensionality reduction using MKL. Finally, we analysed the benefit of using simulated data in the training of ML algorithms for SOO-OTVA classification compared to when only using real patient data.

Different ML algorithms described above (RF, SVM, k-NN and SOM) were used for evaluating the best leads for classifying the training and the test ECGs. An interesting characteristic of the SOM is that they allowed visualizing the most similar signals of the test data that were found in the training data. Therefore, it facilitated finding the key factors that affected the performance of the method. Once evaluated the performance of each lead for classifying the test signals, we studied how the combinations of multiple leads could improve the overall accuracy. Therefore, an exhaustively analysis with all possible 12 lead combinations was performed to estimate the one reaching the best accuracy. In addition, we performed a ranking of the leads that showed highest accuracy in their combinations. A total of 4095 lead combinations were calculated applying the k-NN, SVM, RF and SOM algorithms. We did each experiment twice, first using the raw signal as input and then applying a feature extraction using principal component analysis (PCA) on the input signals. PCA kept the 10 modes that explained most of the signal variance. Raw signals were previously aligned using cross-correlation.

5.3 Results

5.3.1 Single lead evaluation

For individually studying the best leads for SOO classification from the ECG, the RF, SVM, k-NN and SOM algorithms were trained with a single lead for each 12-lead ECG. Only raw 300 ms signals centred around the maximum peak of the QRS complex were used. The obtained accuracy for each lead is summarized in Table 5.1. Although the use of a single lead seems to be insufficient to classify the SOO, results highlights the leads that provide more information or are more discriminant. For the case of classifying simulated ECGs, the accuracy was very high (> 0.9) among

Table 5.1: Accuracy in the real ECG signal classification using each lead of the ECG. RF: Random Forest; SVM: Support Vector Machine; k-NN: k-Nearest Neighbor; SOM: Self-Organizing Maps.

	Simulated (n=1560)				Real (n=35)			
Lead	RF	SVM	k-NN	SOM	RF	SVM	k-NN	SOM
I	0.87	0.88	0.85	0.95	0.46	0.51	0.43	0.37
II	0.93	0.9	0.87	0.99	0.66	0.46	0.57	0.63
III	0.93	0.83	0.81	0.92	0.66	0.43	0.51	0.51
aVR	0.94	0.87	0.87	0.96	0.66	0.4	0.54	0.57
aVL	0.85	0.76	0.74	0.9	0.69	0.43	0.51	0.54
aVF	0.93	0.86	0.84	0.95	0.66	0.37	0.49	0.51
V1	0.95	0.88	0.89	0.97	0.4	0.37	0.49	0.51
V2	0.95	0.92	0.9	0.95	0.37	0.43	0.63	0.66
V3	0.91	0.93	0.86	0.93	0.37	0.54	0.4	0.54
V4	0.92	0.92	0.88	0.97	0.69	0.66	0.74	0.71
V5	0.9	0.91	0.87	0.94	0.66	0.69	0.54	0.57
V6	0.93	0.9	0.87	0.93	0.66	0.63	0.51	0.46

all leads, i.e. the ML algorithms could easily learn simulations. That was expected since even though variability was introduced (different patients, different lead placement on the torso), the simulated ECG morphology was very consistent and not as noisy as real data. When classifying real cases the accuracy decreased, indicating that some aspects of the precordial leads were not faithfully reproduced by the biophysical solver, including potential data uncertainties. In any case, the best accuracy in single lead evaluation in almost all methods was shown by lead V4 (0.74 using k-NN, 0.71 using SOM).

One additional advantage of the SOM approach is that it provides a graphical representation of the results, as can be seen in Figure 5.2. In this figure the test signal (green) of a recorded ECG of a patient (Patient 32) is compared with the closest (neuron) simulated signals according to the SOM results from each of the two classes (blue in the case of LV SOO and red for RV SOO). The SOM that produces the lowest QE is the one finding the most similar signal, and therefore is set as the winner. In this particular case, the ectopic foci determined clinically had a right ventricular origin, as correctly captured with the QE metric in leads V2 and V3, but not in lead V1.

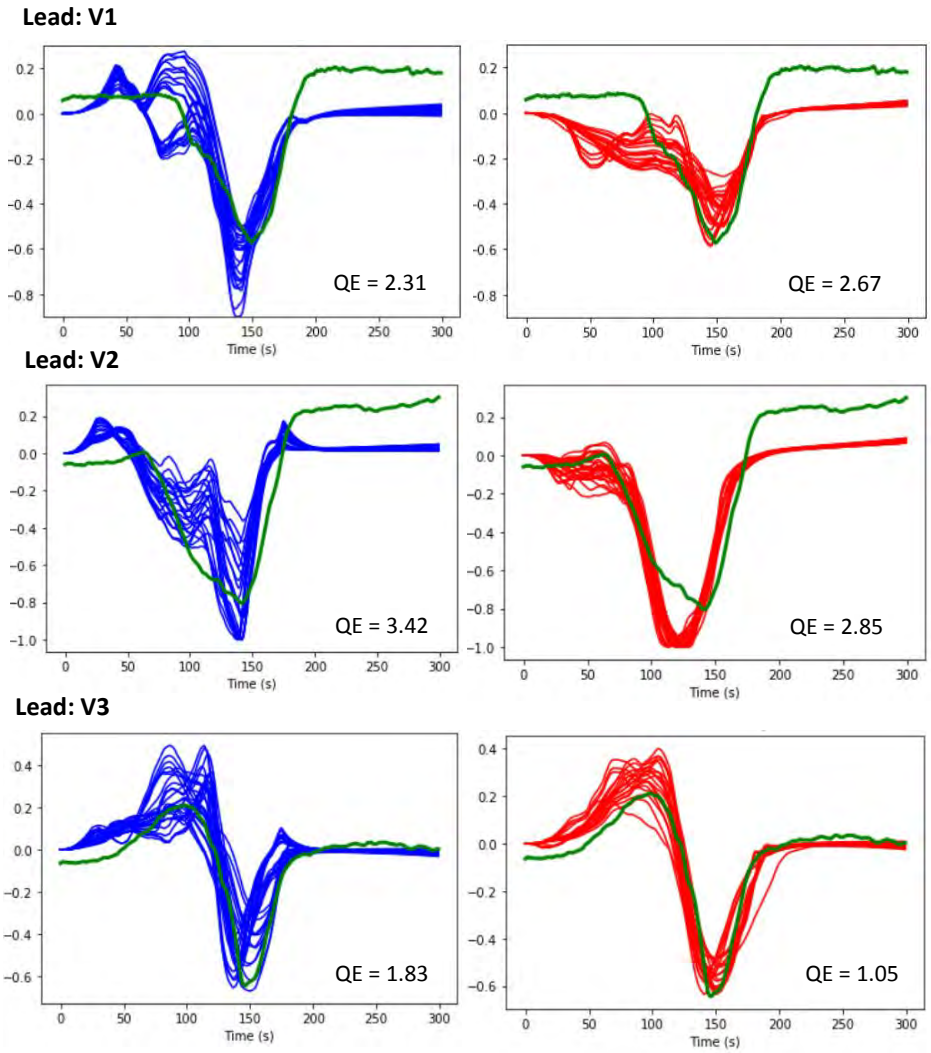

Figure 5.2: Visualization of SOM results for single ECG leads. As an example, three different leads of a measured ECG of a test case (Patient 32) are shown. This patient had a right ventricular origin according to clinical data. For each lead the test signal (green) is compared against the LV SOO simulated signals (blue) and the RV SOO simulated signals (red) that are the most similar signals of these leads according to SOM estimations. The one that has less quantization error (QE) is set as the winner.

5.3.2 Multiple lead evaluation

We performed an exhaustive exploration of the best lead combinations that produced the best accuracy results in classification. A ranking of each lead

Table 5.2: Ranking of the best leads for ECG classification. Leads are ordered from the most to the least relevant according to their calculated score.

k-NN				**SVM**			
Raw		**PCA**		**Raw**		**PCA**	
Lead	Score	**Lead**	**Score**	**Lead**	**Score**	**Lead**	**Score**
V3	241.75	V3	242.89	V3	240.01	V3	242.57
V2	233.90	V2	233.59	V2	227.07	V2	235.91
V4	231.47	V4	231.11	V4	221.1	V4	226.77
II	227.66	II	227.40	II	220.60	III	224.6
aVR	225.27	aVR	226.44	aVF	219.41	V5	224.55
V5	225.25	aVF	226.35	aVR	218.41	aVF	224.24
aVF	225.20	I	224.94	III	217.99	aVL	224.03
I	223.88	aVL	224.74	I	216.80	II	223.91
III	223.64	III	224.71	aVL	216.43	I	223.29
V6	223.59	V5	224.41	V1	214.87	aVR	223.00
aVL	222.9	V6	223.41	V5	214.87	V1	216.57
V1	215.03	V1	217.51	V6	210.39	V6	216.47
RF				**SOM**			
Raw		**PCA**		**Raw**		**PCA**	
Lead	**Score**	**Lead**	**Score**	**Lead**	**Score**	**Lead**	**Score**
V1	192.6	V2	231.42	V2	219.67	V3	224.68
aVF	182.66	V3	228.84	V3	217.44	V2	223.87
V2	181.67	V5	221.13	II	210.47	II	216.22
II	180.29	V4	220.51	V6	210.13	V4	215.2
III	179.08	aVR	217.34	aVF	209.69	aVF	214.62
V4	176.44	I	216.98	V4	208.96	V6	214.22
V6	176.27	V6	216.96	V5	208.94	V5	213.81
aVR	175.48	aVF	216.85	aVR	208.44	III	212.53
V5	175.43	aVL	216.65	III	208.28	aVR	212.52
aVL	172.82	II	216.5	aVL	206.1	aVL	211.07
I	172.8	III	216.3	I	205.54	I	210.84
V3	164.08	V1	209.81	V1	201.61	V1	207.28

according to their capacity of classifying properly the SOO considering all possible combinations and ML algorithms is shown in Table 5.2. The total ranking score for each lead is calculated by summing up all the weighted accuracy scores obtained in each combination in which the lead participated. The weighted accuracy score was the result of dividing the total accuracy obtained in one combination by the total number of leads that participated

Table 5.3: Accuracy and F1-score of the real ECG signal classification using different combinations of ECG leads.

	Raw							
	RF		SVM		kNN		SOM	
	accuracy	F1-score	accuracy	F1-score	accuracy	F1-score	accuracy	F1-score
All leads	0.74	0.66	0.54	0.55	0.74	0.66	0.74	0.69
Precordials	0.6	0.61	0.43	0.34	0.63	0.48	0.63	0.58
V2,V3,V4	0.4	0.52	0.54	0.1	0.83	0.72	0.77	0.71
V2,V3,V4,V5	0.4	0.51	0.6	0.3	0.89	0.82	0.69	0.6
	PCA							
	RF		SVM		kNN		SOM	
	accuracy	F1-score	accuracy	F1-score	accuracy	F1-score	accuracy	F1-score
All leads	0.77	0.66	0.77	0.71	0.71	0.65	0.71	0.62
Precordials	0.69	0.62	0.66	0.60	0.63	0.52	0.66	0.63
V2,V3,V4	0.8	0.72	0.66	0.57	0.83	0.77	0.66	0.65
V2,V3,V4,V5	0.89	0.82	0.71	0.62	0.83	0.76	0.69	0.65

in that combination. Therefore, high scores are obtained by leads which participate in combinations with a high classification score, and the number of leads used is smaller. The score was calculated in two different ways: first using the raw 300 ms data of the ECG as an input, and second by using the principal 10 components obtained from a PCA.

We analysed the results for k-NN, SVM, RF and SOMs, obtaining the best rankings for V3, closely followed by V2 and V4. The random forest algorithm showed unexpected results when raw data was used, which could be due to the type of training information used. The problem was solved when only a few characteristics estimated with PCA were provided instead of the raw signal. We observed good consistency between methods classified with raw data versus the best 10 characteristics from PCA. However, when PCA was applied before training the results improved in all cases, suggesting that this is the best strategy.

Finally, Table 5.3 shows the classification accuracy and the F1-score (harmonic mean of the precision and recall) obtained for different lead combinations with clinical relevance. Using all leads or the precordial leads shows an improvement in classification with respect to single leads, but differences are not notable. Selecting the leads that showed the best ranks from Table 5.2 (V2, V3, V4 and V5) the classification accuracy increased (up to 0.89 for RF), which was the best result obtained. As expected, RF and SVM had a better performance when using PCA.

5.3.3 Dimensionality reduction using MKL

Simulated and real ECG signals used for classification were evaluated using MKL. A total number of 155 ECG signals were introduced as input in the algorithm (120 simulated signals + 35 recorded signals). In order to facilitate the MKL algorithm computation, no augmented data was used. Results of using the 12-lead ECG as features vs the combination of the most important leads (V2,V3,V4,V5; according to previous analysis) are shown in Figure 5.3. This Figure shows the results of performing the training using the 12 leads as descriptors (A) and the best leads obtained in the previous ranking (B). Both figures clearly show two different groups that correspond to the LV vs RV SOO. This difference is clear in figure B, where only a few points were misclassified. We performed a classification (RV vs LV SOO) from the low-dimensional representation of the data provided by the MKL algorithm. For doing so, we used SVM with the same parameters mentioned above. The classification results obtained when using all leads as input (Figure 5.3 (A)) were the following (accuracy, F1-score): simulated ECG signals (0.84, 0.87); real ECG signals (0.51, 0.48). When only data from the most relevant leads (V2,V3,V4,V5) were used (Figure 5.3 (B)), the results were substantially improved for real data: simulated ECG signals (0.86, 0.88); real ECG signals (0.77, 0.80).

5.3.4 Classification performance with only real ECG data for ML training

In order to have a better estimation of the results obtained using the simulated data as training, we performed a classification using only the 35 ECGs recorded from patients, without any simulated signal. We used the ML methods that presented the best results in Table 5.3: RF, SVM, k-NN and SOM after a previous dimensionality reduction by PCA. We used the leave-one-out cross validation technique, since 35 ECGs is a low number for training ML algorithms. Results are shown in Table 5.4. Accuracy values were overall slightly inferior to the ones obtained by using simulated data (Table 5.3), except when using the precordial leads, where the highest value (0.8 using RF) was obtained. Calculated F1 scores were clearly inferior to the ones obtained using simulated data.

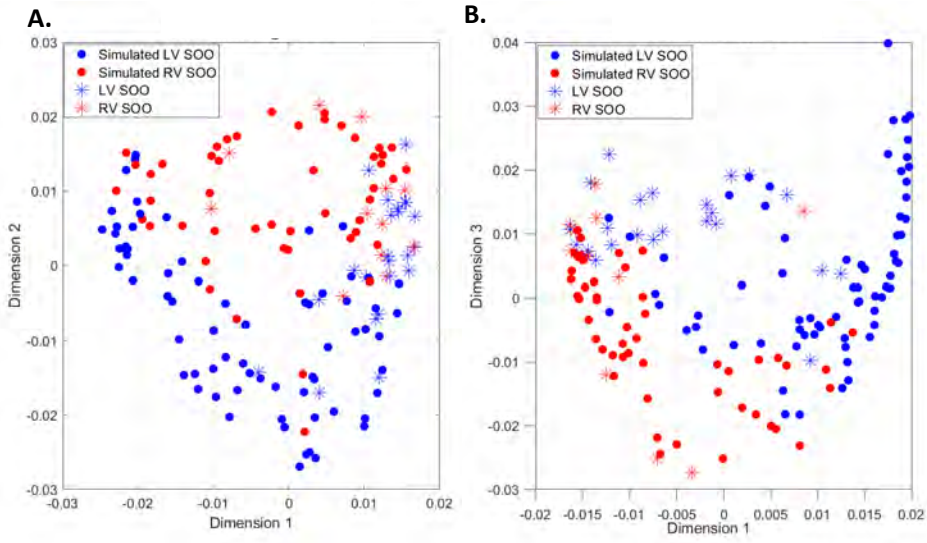

Figure 5.3: Comparison of LV (blue) and RV (red) SOO signals in a low-dimensional representation provided by the Multiple Kernel Learning (MKL) algorithm. The two panels show the cluster distribution in the first two dimensions of the low-dimensional space identified by MKL after using all leads as features (A) and only the most relevant leads (V2,V3,V4,V5) according with previous results (B). Simulated signals are represented by dots whereas real ECG signals are represented by asterisks.

Table 5.4: Accuracy and F1-score of the real ECG signal classification without using simulated ECGs

	RF		SVM		kNN		SOM	
	accuracy	F1-score	accuracy	F1-score	accuracy	F1-score	accuracy	F1-score
All leads	0.74	0.64	0.71	0.57	0.68	0.52	0.77	0.6
Precordials	0.8	0.69	0.65	0.37	0.65	0.5	0.71	0.6
V2,V3,V4	0.71	0.54	0.74	0.52	0.71	0.54	0.68	0.61
V2,V3,V4,V5	0.77	0.66	0.74	0.66	0.71	0.54	0.66	0.56

5.4 Discussion

This study shows the feasibility of utilizing simulated ECGs to train ML algorithms that are able to localize the SOO in OTVA from 12-lead ECGs. By applying different ML methods, we evaluated the role of the different ECG leads in data classification and the ability of the simulations to mimic the behaviour of the recorded ECGs. The role of the ECG leads was evaluated individually and by doing different combinations of leads. We used raw ECG signal (300 ms) obtained from the simulations and extracted from the ECG as an input. In order to have a good comparison of the differ-

ent morphologies of the QRS complex, signals were previously aligned by performing cross-correlation. This last step was important since little miss alignments could have critical effects in the classification. For this reason, we also performed a PCA on all the input signals. In that way, only the first 10 principal components were considered for the classification. There exist previous studies in the literature that try to classify the SOO in ventricular tachycardias, although they never studied the effect of each component individually, but the combination of all the signals in the 12-lead ECG. For instance, in [169] they use convolutional neural networks (CNN) and obtained and accuracy of 77.71% in the classification of the SOO. One of the drawbacks of this type of methods is the difficulty to determine and explain which characteristics were chosen by the CNN and why they work well. In [188] they analyse the most important characteristics of each ECG signal, and use them to train a SVM for classification of the SOO, obtaining an accuracy of 88.4%. However, they pointed out that the groups most difficult to classify were RVOT septum and aortic cusps, that showed an accuracy of 42.86%. These two SOO were also considered in our study, and can be the source of classification errors since they are anatomically close to each other.

We evaluated the ability of each lead to classify properly the signals between RV vs LV, as it is shown in Table 5.1. As expected, simulated data was classified properly showing high accuracy values, specially using SOM, where all values were above 0.9. Regarding the test data, which was only the recorded patients ECG, values were significantly lower, showing the incapability of classifying between RV vs LV SOO by using only one lead. Thanks to the design of the SOM algorithm, we can visualize how the algorithm learns from the input data since it shows the closest signal to the test data during the classification and the QE (see Figure 5.2). In that way, we can evaluate which simulated leads are closer to the test data and therefore have an estimation of the quality of the simulations.

Since we aim to obtain the best combination of leads for the prediction of the SOO we performed a global rank of the leads. We observed, as expected, that lead V3 and V4 were the most discriminant, followed by V2 and V5. That means that any prediction in which V3 or V4 are included has higher chances to predict correctly the SOO, for any location of the ectopic focus and any geometry of the heart studied. These results are in agreement with clinical studies that look for specific features in leads such as V3 [15, 25]. It is also important to take into account that we are training with simulated data, and that the simulated ECGs might be more realistic for some leads

than for others. Therefore, some features learnt in some leads in the training set could not fit with real ECGs for a given SOO, and then removing them from the training set improves the accuracy of the classifier.

We also studied the possibility of having a dimensionality reduction before the training by using PCA and a dimensionality reduction to 10 dimensions. Following that approach all the results improved significantly, specially the RF. This may indicate that algorithms such as RF or SVM could present problems to work with raw data instead of a reduced signal model.

Overall, the best results were obtained using the combination of leads V2, V3, V4 and V5, with k-NN (see Table 5.3). The cause under the good performance of this particular algorithm could be the evident relation between the SOO and the corresponding signals. k-NN algorithm works studying the similarities among ECG signals, and signals that are similar to each other correspond to ectopic focus triggered from points close to each other.

MKL was used for visualizing the input data. Since it is an unsupervised algorithm, all the data (test and training) was introduced as input. The obtained results, that can be seen in Figure 5.3 confirm that ML algorithms are able to distinguish between RV vs LV SOO in simulated and real data. One drawback of this method is the fact that although we can see its ability to classify, it is not straightforward to know what features are used for that purpose. The MKL algorithm can also be used to compared simulated vs real signals. In Figure 5.3 (A) we can observe that simulated signals are forming a small cluster at the right of the graph. This means that MKL is able to detect the simulated data from the rest of simulations. In Figure 5.3 (B), asterisks are more uniformly distributed on the plane, which indicates that the similarity between simulated and real data has increased. This might be caused by the fact that some simulated leads (e.g. lead V1 or V6) are not able to reproduce the behaviour shown in the real leads.

Finally, we evaluated the impact of using simulated data in the training of ML algorithms. We performed a real ECG classification without using simulated data and compared the results with the obtained using the simulated data as training. Results proved that better accuracy and F1 scores are obtained by using the simulated data for training, except when only the precordial leads are evaluated (RF trained with real data offers the best performance). This confirms the potential of the simulated data to reproduce the real ECG data and to improve the performance of the ML techniques. However, more test and training data are needed to have a solid confirmation.

In summary, we showed that it is possible to classify clinical data, using as a training set simulated signals, where we can control in detail the origin of the ectopic focus, and the patient anatomy. The classification works better when the patient-specific geometry is used, which indicates that we have to extend the database of simulations to take into account patient variability in terms of anatomy and orientation with respect to the torso. All cases analysed where idiopathic, i.e., we did not consider any type of structural disease, which would be much harder to classify due to the effects of scarred tissue in the activation sequence. Using the different ML algorithms we observed that not all the precordial leads exactly reproduced the real patterns, which affects negatively the model, since they cannot be used for training and classification. Therefore, improving the computational simulations together with a larger database that includes a large variability in the patient ECG would improve the results obtained in this study.

We have shown a computational approach to predict the SOO of idiopathic ventricular tachycardia originated in the ventricle outflow tract. The method that relies in biophysical simulation and machine learning techniques is able to differentiate between LV or RV origin of the ectopic beat with an accuracy of 89%, by using as an input data precordial leads V2, V3, V4, and V5. since all the simulated training set is built off-line, the methodology could be transferred to a clinical environment easily, avoiding the need of time consuming tasks such as building computational models of the heart and performing electrophysiology simulations. In addition, the methodology is not dependent on the expertise of electrophysiologist, and it is consistent between cases, which could provide an additional tool to electrophysiologist to plan RFA interventions of this type of tachycardia. Future works will focus on the accurate determination of the exact SOO of the tachycardia.

6

General Conclusions

6.1 Short summary

In this thesis, we have developed computational methods to simulate cardiac electrophysiology in patients with arrhythmia originated in the ventricle outflow tract, as well as tools to be able to identify its origin from non-invasive data.

The methodology has been divided in three main components.

In Chapter 3, we presented a RBM that includes fiber information specific to the RV, inter-ventricular septum and both OT of the ventricles, to replicate histological observations. The proposed model improves the realism of electrophysiological simulations in applications when these regions are important such as in OTVA patients. That was not possible with previous RBM in the literature since they tend to apply the rule of LV to RV, and do not model properly the septal wall. The RBM was indirectly validated by comparing the results of electrophysiological simulations that incorporated the proposed arrangement of fiber orientation with EAMs acquired from patients during OTVA. The obtained results showed good agreement with clinical observations, demonstrating the potential of the RBM as a component for the simulations that aim to replicate the sequence of activation of this type of arrhythmias.

In Chapter 4, we developed a computational pipeline, that included the RBM developed in Chapter 3, to perform patient-specific *in silico* pace mapping, which helped us to replicate the procedure followed by electrophysiologist in the electrophysiology Lab in a non-invasive manner. We were able to build 11 patient-specific models, that included the patient anatomy and EAMs. Following, we simulated the electrical sequence of activation of

the patient in sinus rhythm and during tachycardia, as well as the patient's ECG.

Simulations matched the clinical data, and allowed us to use the models to produce a large set of ECGs corresponding to arrhythmia originated from different locations on the LV and RV outflow tracts. That helped us to further validate the pipeline against data from the literature (description of ECG morphology as a function of SOO), and at the same time to evaluate the similarity between the ECGs originated from the same ectopic location in different patients. Simple tools such as the correlations between signals were used to evaluate the simulation versus the patient data, and to define which ECG precordial leads were more informative to differentiate between SOO.

Finally, in Chapter 5, we used all the models developed in previous Chapters, and studied different machine learning techniques to train a system with simulated ECGs, capable of predicting the site of origin of an arrhythmia originated in the OT. To account with the ECG variability introduced by the ECG lead placement, we enhanced our simulated ECG database with different ECGs obtained on the surrounding of the standard lead location (displacement and torso rotation). We test the classification of real clinical ECGs of patients with OT ventricular arrhythmias using single leads, or combinations of them. Our results showed that leads that show a better discrimination factor between left vs right origin of the tachycardia were V3 and V4, but results improved when V2-V5 were all combined. Our results matched the hypothesis of electrophysiologists that use mainly the information in V3 to decide the origin of the arrhythmia. The best model for classification of ECGs was the k-NN with an accuracy of 89%. We could classify properly some cases that were considered very complex for electrophysiologist pre-operatively, showing that the tool has the potential to help in planning intervention of RFA in this type of arrhythmia.

6.2 Limitations and future perspectives

There are several limitations of the work presented that are summarized in the following paragraphs.

One of the main limitations of the RBM method is the absence of quantitative 3D fiber information from imaging data in the RV and in the OTs. We developed our method being guided by findings in histological stud-

ies from 2D pictures of ex-vivo specimens and following recommendations from anatomists involved in this work. It would be desirable to compare our results with data obtained from advanced imaging techniques such as micro-CT or X-ray phase-contrast imaging, especially from the RV and OTs, which is rarely available in the literature. In this thesis we also compared our results with ex-vivo cardiac DT-MRI. This technique provides information related to myofiber orientation, but it cannot be considered as ground-truth since measurements are noisy, show poor signal-to-noise ratio and change under gradient calibration and temperature variation [189]. In addition, smoothing and interpolation techniques required to reconstruct tensor data from cardiac DT-MRI do not allow capturing myofiber orientation changes in very heterogeneous areas. Unlike in the LV, where DT-MRI may provide a good approximation of myofibers in most areas, this is particularly critical in thin structures of the heart such as the outflow tracts and the RV. Another limitation of the developed RBM is the smoothness of the resulting fiber orientation distributions, which is inherent to the RBM. Unlike the variability found in histological data, a RBM tend to generate idealistic fiber orientation, in part due to the use of smooth biventricular geometries (e.g. without trabeculae). Finally, the definition of the longitudinal direction in some points of the boundary surfaces can affect the fiber orientation. Due to the definition of the boundary, the gradient in these points is zero, thus obtaining an incorrect fiber orientation (an example can be seen in Figure 3.8, where apical regions have a slightly higher angle difference in all cases). However, this problem can be minimized by reducing the number of points taken as boundaries and applying interpolation with the closest neighbors.

Further work will be focused on the application of this pipeline to a larger clinical database and in the adaptation of the developed RBM to high-resolution fiber information provided by X-ray phase-contrast imaging data.

With respect to the computational pipeline to generate virtual ECGs of patient showing arrhythmia triggered from the OT, we have to acknowledge some limitations. Our patient-specific models included the patient geometry and general properties for the tissue, since we did not personalize the conductivities in the heart or other organs. Although we did not expect substantial changes in the overall pattern of the ECG due to that fact, there might be changes in the amplitude or the duration of the waves. That is why, we decided to work with normalized signals. A personalization of conductivity parameters will require a set of simulations that will increase substantially the computational cost, making the tool more diffi-

cult to translate to the clinics. One potential complementary alternative could be to use simplified models for performing fast simulations of cardiac electrophysiology that allow the fast estimation of the desired parameters.

Our models did not include patients with any type of structural heart disease, which will also impact the ECG wave morphology, and could hamper the classification of the signals by the automatic algorithm. In addition, we are using only the activation sequence to compare signals, not considering the repolarization, where the effect of infarcted regions will be more important. Therefore, we have only assessed the methodology in idiopathic patients.

As a future work, we expect to exploit the pipeline extending the current set of patients to a much large population, which allows us to consider more heart-torso geometries. We also want to perform simulations in patient with structural heart disease, so that we can assess the difference in the ECG in a quantitative way. Another important group of simulations that would be required are those triggered from the epicardium, since in this work we only considered one epicardial SOO for the tachycardias. These new datasets can help us to further validate the pipeline, and to improve the accuracy of the classifiers built based on the simulation data. Clinical studies that try to predict whether the origin of a ventricular tachycardia comes from the LVOT or RVOT have used algorithms based on particular properties of the ECG waves, and in particular the precordial leads. Since our simulations do not reproduce precisely some wave characteristics such as the amplitude, we did not use those algorithms for validation of our results. Therefore, one of the goals in the future is to improve the pipeline to obtain more realistic QRS-waves in terms of signal amplitude.

The systems should take into account possible incorrect location of some precordial leads. This is specially important since in the electrophysiology Lab due to requirements that the navigation system imposes, some leads might be displaced with respect to their standard locations. This fact has to be explicitly considered in our model, in order to improve the results in all possible scenarios.

Once all the improvements are carried out, we aim to assess the methodology to classify the origin of the tachycardia considering any location of the ventricles. That would involve a large number of simulations to be carried offline, but it should only be done once.

Regarding the machine learning methods studied in this thesis to determine the origin of the tachycardia, we have used standard and well-known tech-

niques, which have shown good performance but will require much larger training sets to be able to improve their accuracy. In addition, we need to balance better the number of cases we have from different locations, in order to perform better tests. While in the training set the origin of the ectopic focus can be virtually anywhere thanks to the use of the cardiac simulator, the validation set requires the collection of datasets from different patients and with ectopic foci distributed all over the regions of interest (e.g. AMC, LV summit, LCC-RCC, RVOT, RFW, etc).

In order to extract the correct features to train ML algorithms, future work will be focused on the use of deep learning techniques. However, using a black-box as a clinical decision making tool is not a good approach for clinicians. Other methods such as SVM or K-NN provide results which could be easily interpreted by doctors. In that sense, the introduction of non-supervised learning methods such as SOM or MKL could further help in the interpretation of the classifiers, complementing the current clinical methodologies to determine the origin of a focal tachycardia.

In conclusion, the methods and pipeline developed in this thesis have shown the potential of combining biophysical simulations of cardiac electrophysiology with machine learning techniques to predict the site of origin of idiopathic ventricular tachycardias, and help in RFA interventional planning. One of the advantages of the methods presented are that the simulations can be performed off-line by an expert engineering, and can be incorporated gradually into a database that the machine learning tools can exploit. Therefore, the translation into the clinical environment does not require experts in the field of simulations, or time consuming tasks such as segmentation, modeling and biophysical simulations. Therefore, the most important limitation if the amount of data available to build a database large enough to consider most of the potential scenarios.

The methodology could be easily integrated into already available clinical tools for planning interventions without a big effort, since the methods used in the thesis are standard and available in open-source scientific software packages.

A

Complete catalogue of electrophysiological and electrocardiogram simulation results

In Appendix A all simulation results obtained with the developed modelling pipeline for all 11 biventricular geometries studied in this work and the 12 different sites of origin (SOO) are presented. For each case, results are displayed in two figures. In the first one, simulation results are presented in 12 different columns according the SOO. This type of visualization is inspired by artwork presented in Anderson et al. [15]. In the second one, the measured patient 12-lead ECG (black) and the simulated ECGs (Blue for LV SOO and red for RV SOO) are compared. For the sake of clarity, only ECGs obtained using one of the thirteen lead configurations are presented.

A.1 Patient 1 (Ablation in RCC)

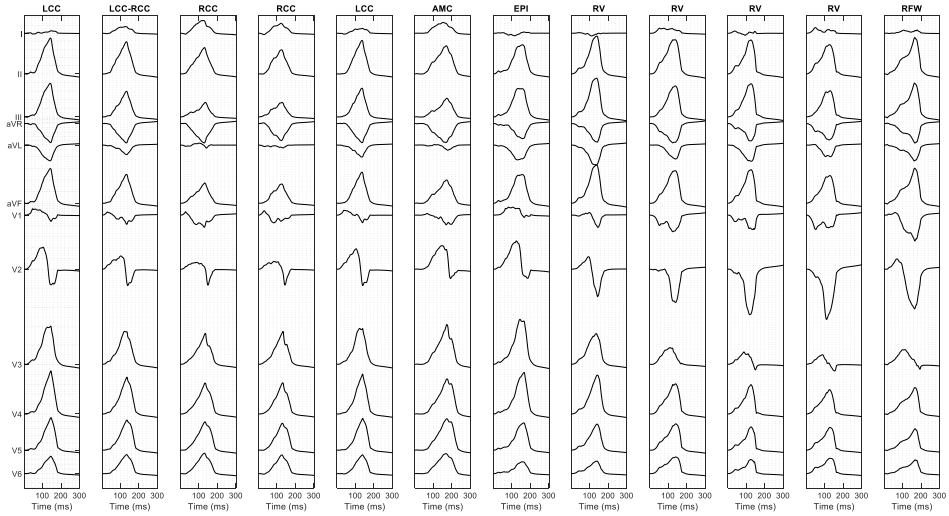

Figure A.1: 12-lead simulated signals for the 12 different sites of origin of Patient 1.

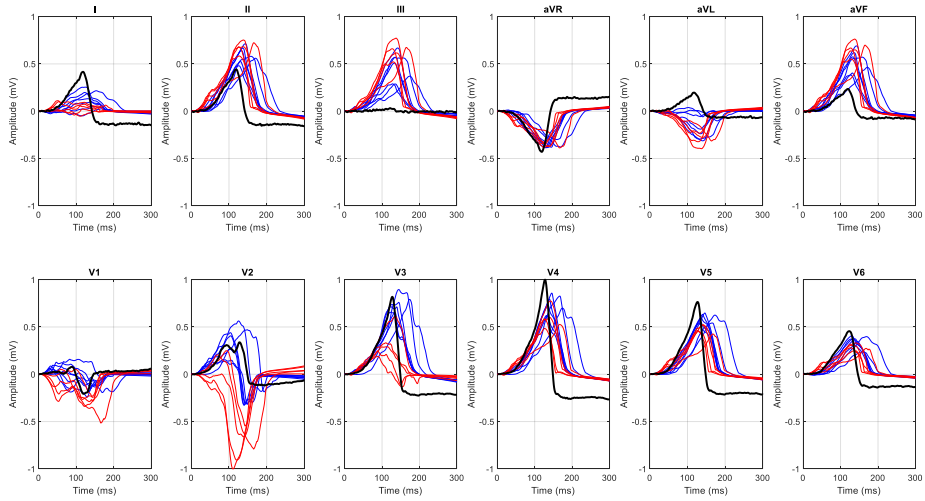

Figure A.2: Simulated 12-lead ECG for Patient 1. Signals simulated from a LV SOO are represented in blue color whereas RV SOO signals are in red. Black ECG belongs to the patient ECG.

A.2 Patient 2 (Ablation in LCC)

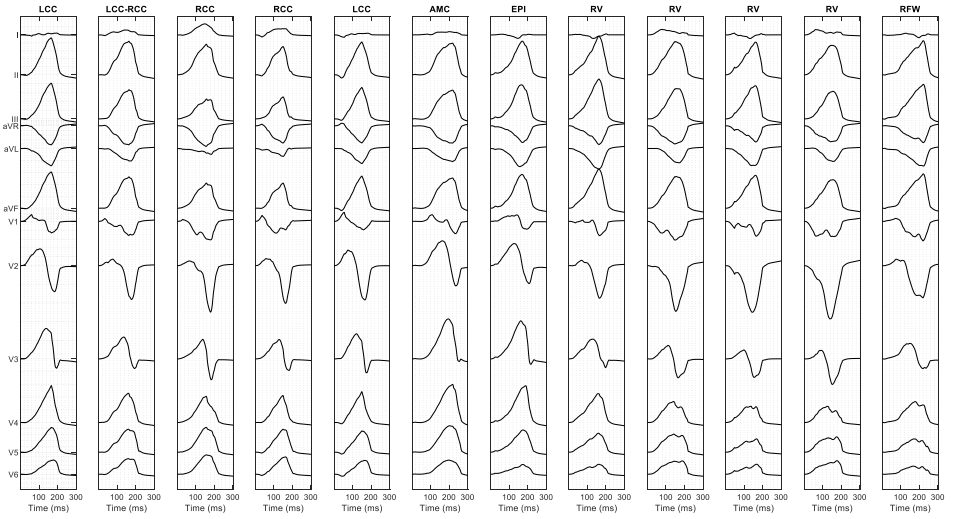

Figure A.3: 12-lead simulated signals for the 12 different sites of origin of Patient 2.

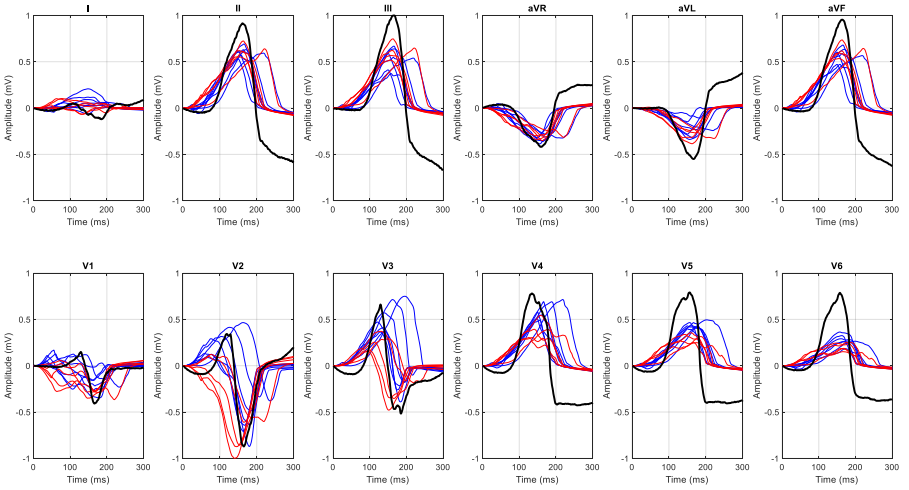

Figure A.4: Simulated 12-lead ECG for Patient 2. Signals simulated from a LV SOO are represented in blue color whereas RV SOO signals are in red. Black ECG belongs to the patient ECG.

A.3 Patient 3 (Ablation in LCC)

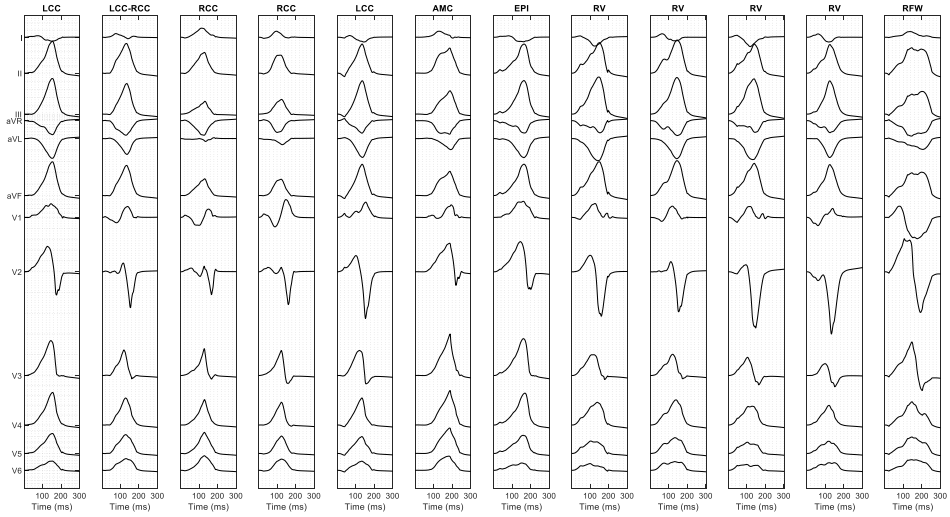

Figure A.5: 12-lead simulated signals for the 12 different sites of origin of Patient 3.

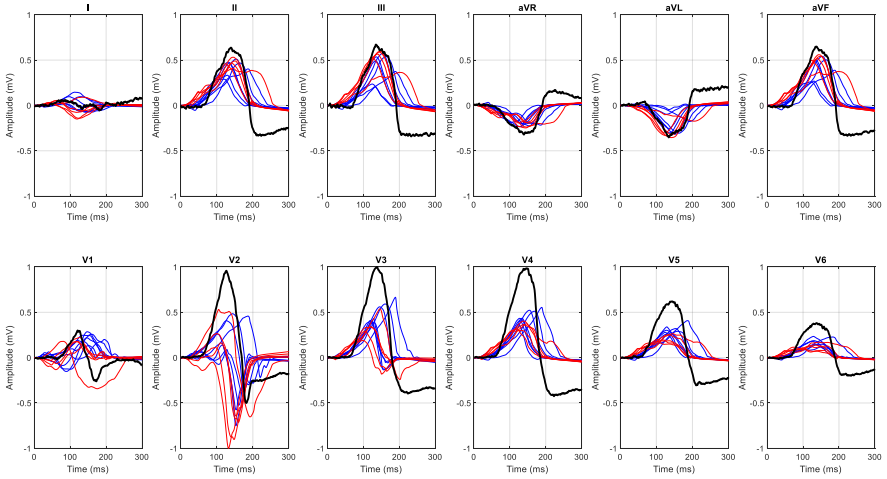

Figure A.6: Simulated 12-lead ECG for Patient 3. Signals simulated from a LV SOO are represented in blue color whereas RV SOO signals are in red. Black ECG belongs to the patient ECG.

A.4 Patient 4 (Ablation in LCC)

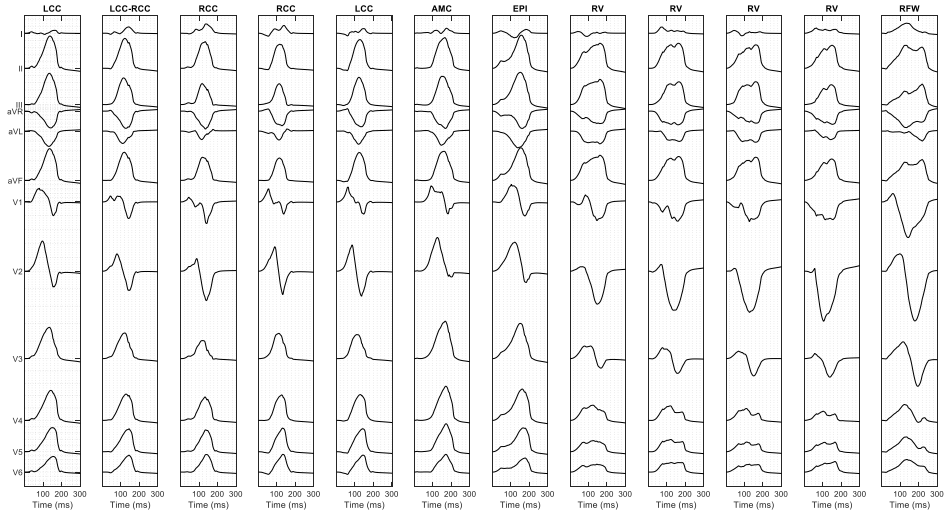

Figure A.7: 12-lead simulated signals for the 12 different sites of origin of Patient 4.

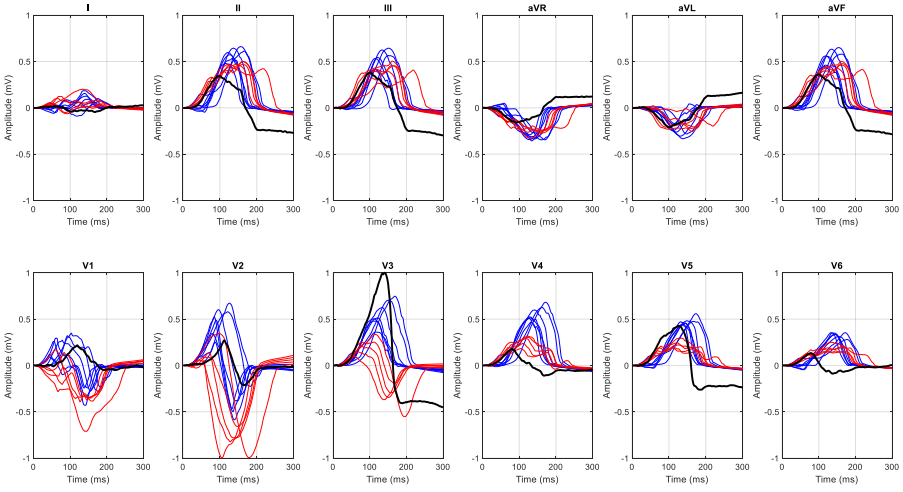

Figure A.8: Simulated 12-lead ECG for Patient 4. Signals simulated from a LV SOO are represented in blue color whereas RV SOO signals are in red. Black ECG belongs to the patient ECG.

A.5 Patient 5 (Ablation in RCC)

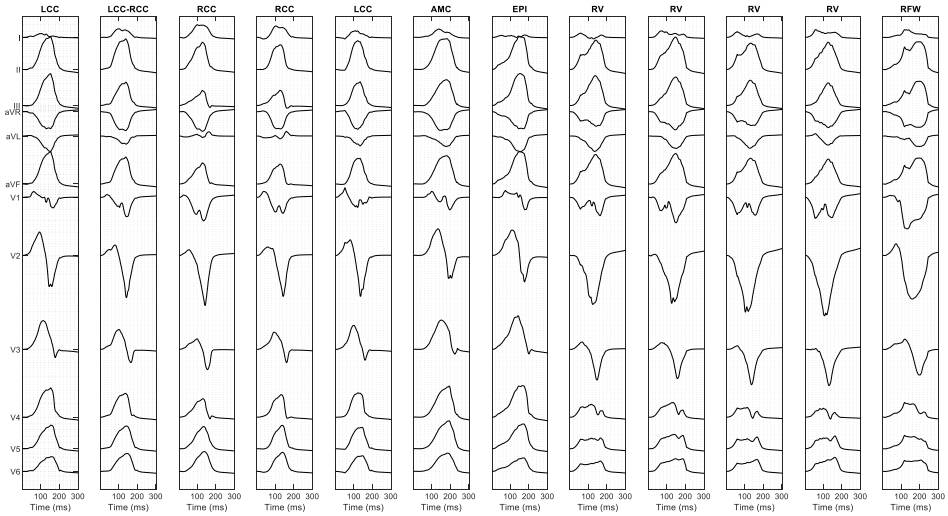

Figure A.9: 12-lead simulated signals for the 12 different sites of origin of Patient 5.

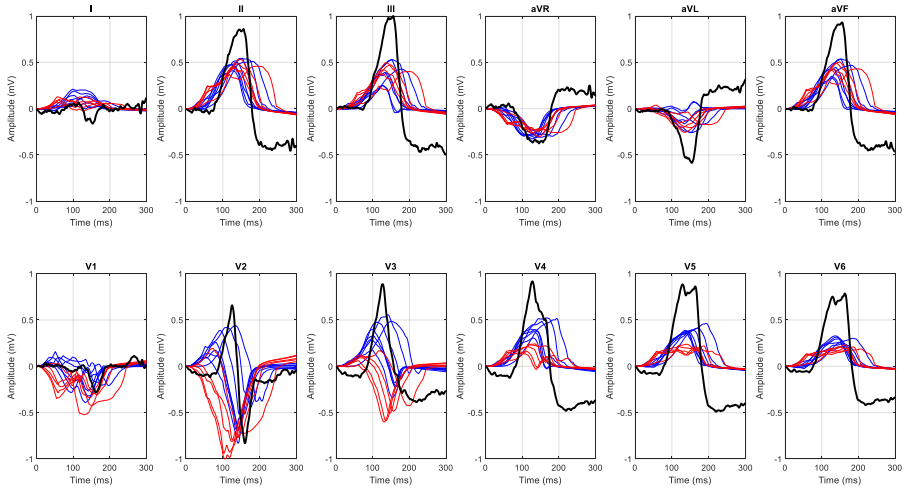

Figure A.10: Simulated 12-lead ECG for Patient 5. Signals simulated from a LV SOO are represented in blue color whereas RV SOO signals are in red. Black ECG belongs to the patient ECG.

A.6 Patient 6 (Ablation in RCC)

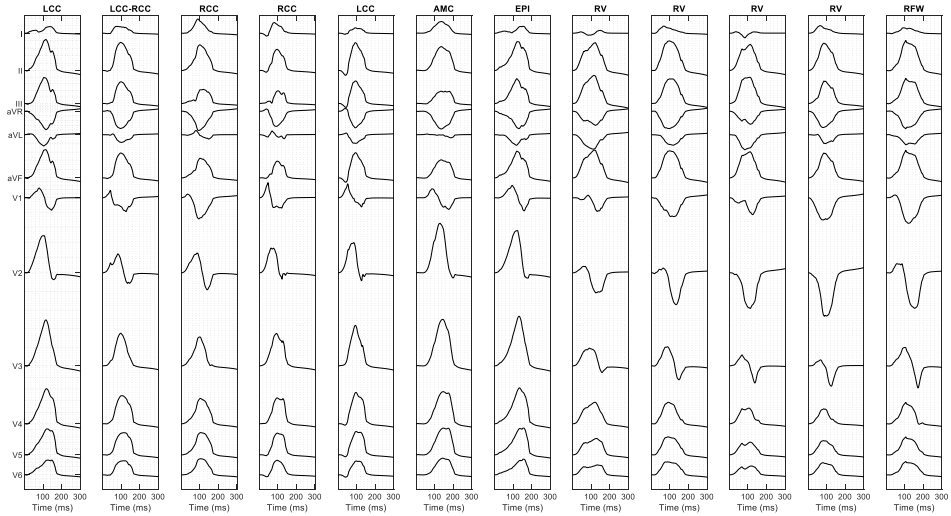

Figure A.11: 12-lead simulated signals for the 12 different sites of origin of Patient 6.

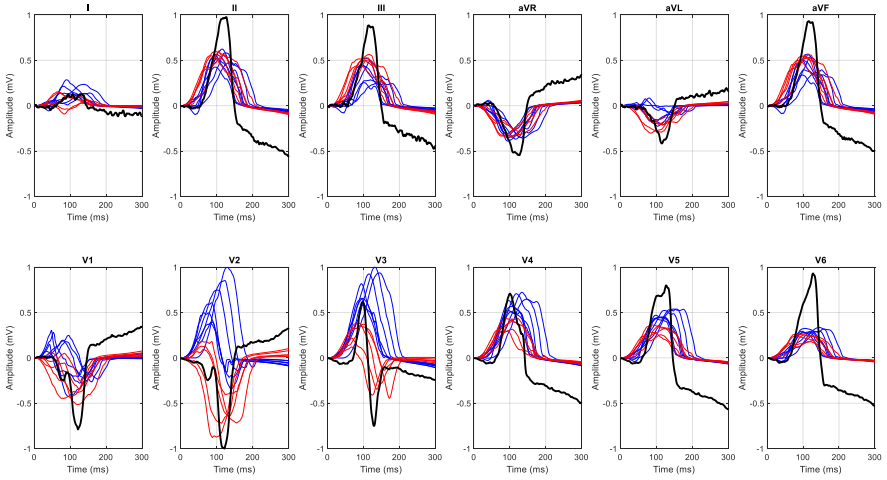

Figure A.12: Simulated 12-lead ECG for Patient 6. Signals simulated from a LV SOO are represented in blue color whereas RV SOO signals are in red. Black ECG belongs to the patient ECG.

A.7 Patient 7 (Ablation in RV)

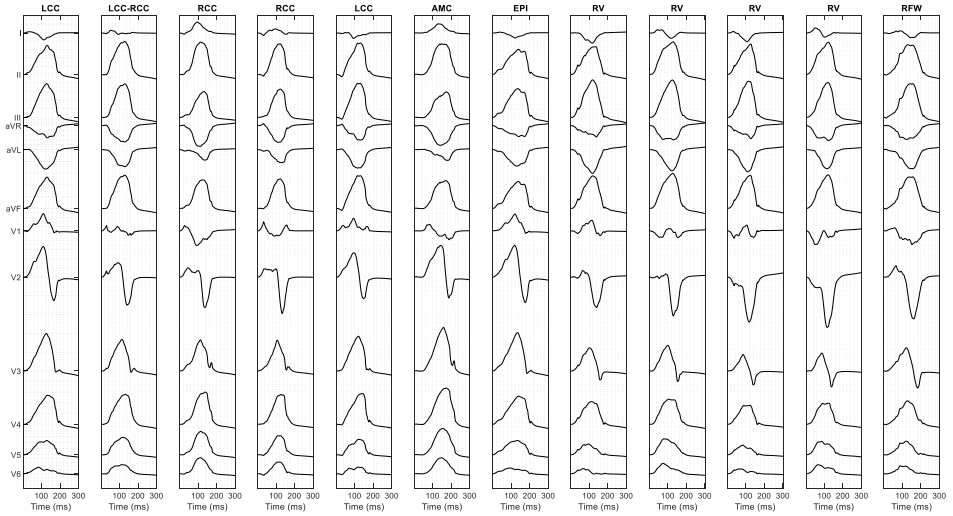

Figure A.13: 12-lead simulated signals for the 12 different sites of origin of Patient 7.

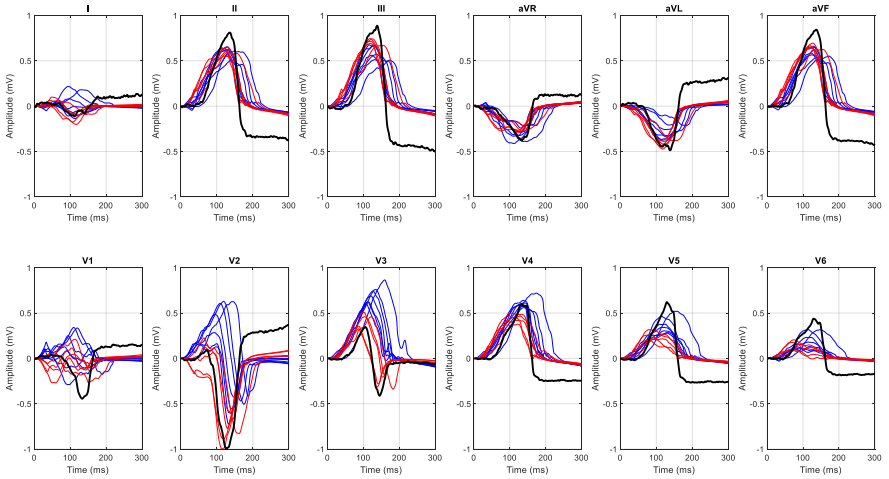

Figure A.14: Simulated 12-lead ECG for Patient 7. Signals simulated from a LV SOO are represented in blue color whereas RV SOO signals are in red. Black ECG belongs to the patient ECG.

A.8 Patient 8 (Ablation in RCC)

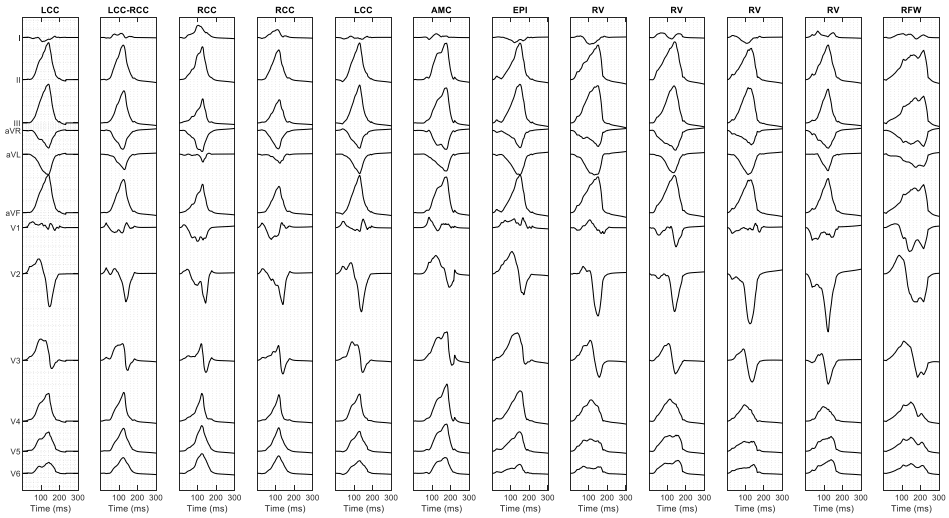

Figure A.15: 12-lead simulated signals for the 12 different sites of origin of Patient 8.

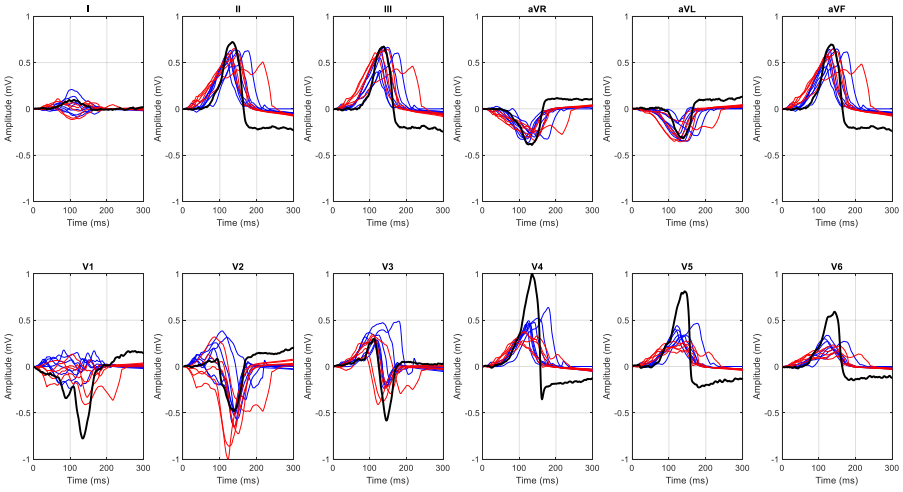

Figure A.16: Simulated 12-lead ECG for Patient 8. Signals simulated from a LV SOO are represented in blue color whereas RV SOO signals are in red. Black ECG belongs to the patient ECG.

A.9 Patient 9 (Ablation in RCC)

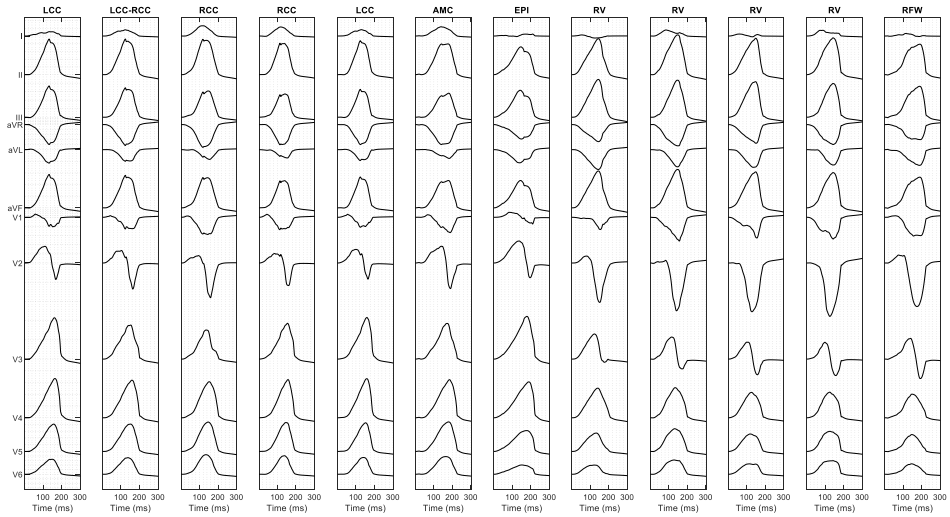

Figure A.17: 12-lead simulated signals for the 12 different sites of origin of Patient 9.

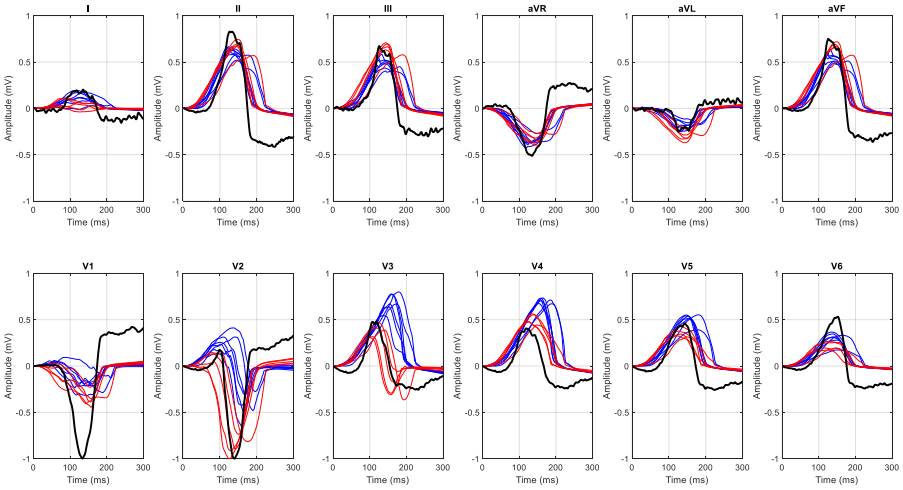

Figure A.18: Simulated 12-lead ECG for Patient 9. Signals simulated from a LV SOO are represented in blue color whereas RV SOO signals are in red. Black ECG belongs to the patient ECG.

A.10 Patient 10 (Ablation in RV)

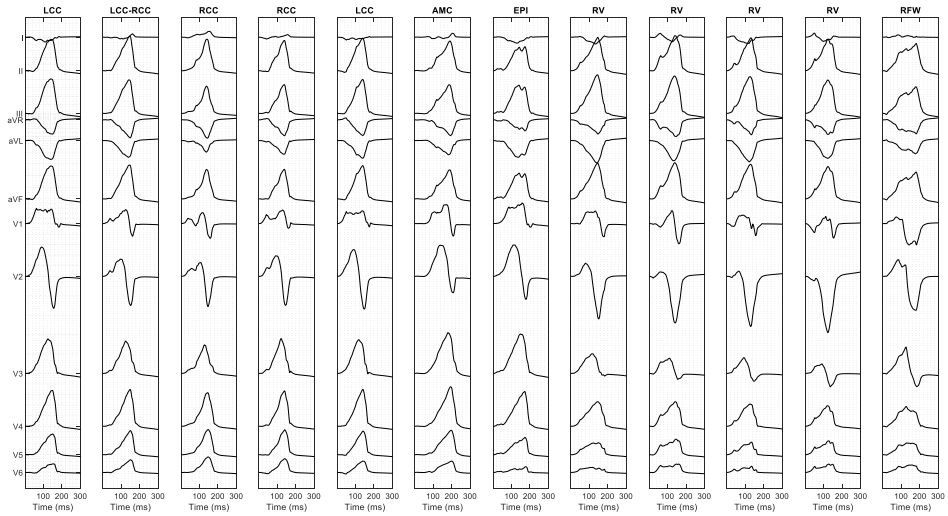

Figure A.19: 12-lead simulated signals for the 12 different sites of origin of Patient 10.

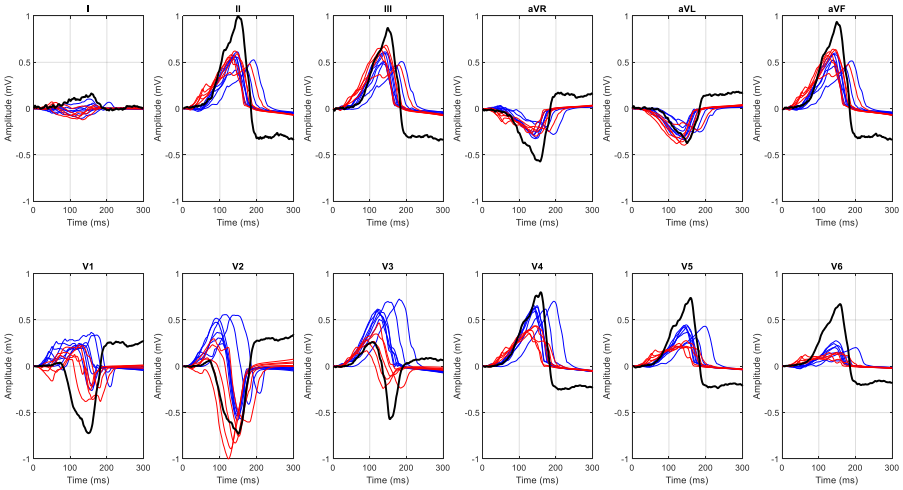

Figure A.20: Simulated 12-lead ECG for Patient 10. Signals simulated from a LV SOO are represented in blue color whereas RV SOO signals are in red. Black ECG belongs to the patient ECG.

A.11 Patient 11 (Ablation in RV)

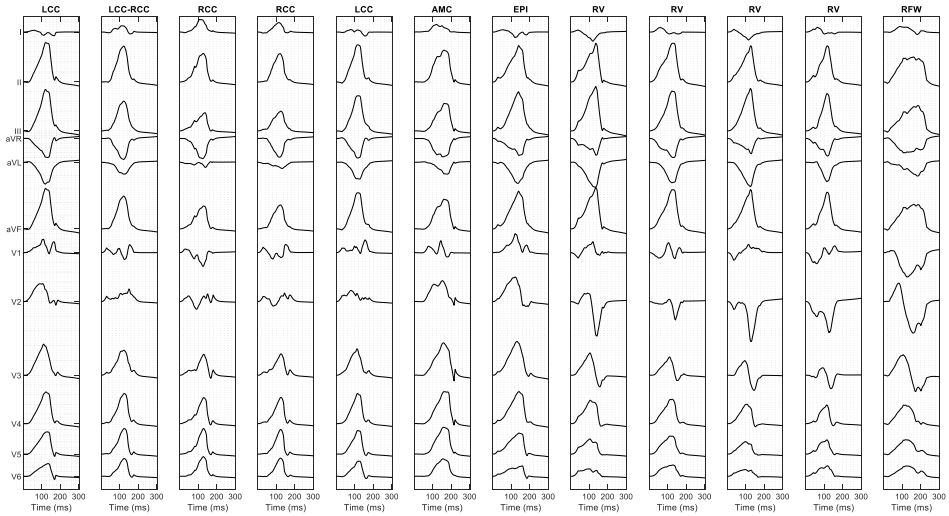

Figure A.21: 12-lead simulated signals for the 12 different sites of origin of Patient 11.

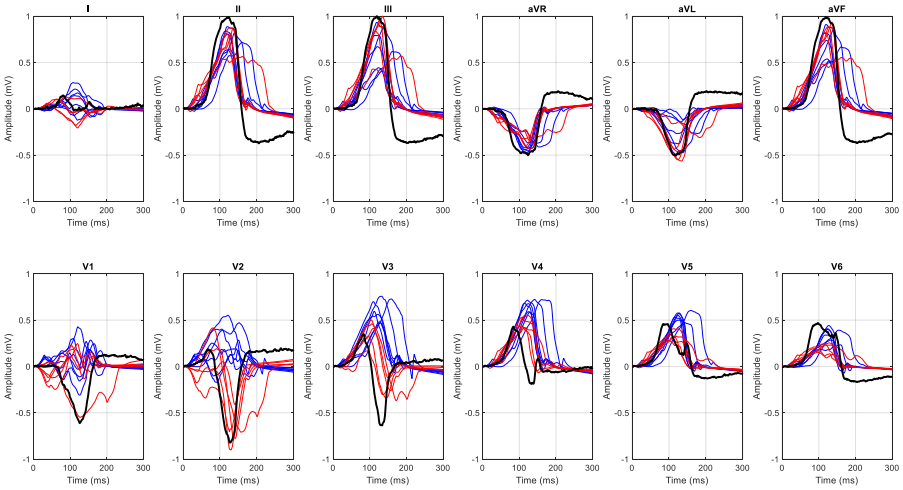

Figure A.22: Simulated 12-lead ECG for Patient 11. Signals simulated from a LV SOO are represented in blue color whereas RV SOO signals are in red. Black ECG belongs to the patient ECG.

Bibliography

[1] Damian Sánchez-Quintana, Manuel Doblado-Calatrava, Jose Angel Cabrera, Yolanda Macías, and Farhood Saremi. Anatomical Basis for the Cardiac Interventional Electrophysiologist. *BioMed Research International*, 2015:1–24, 2015.

[2] Robert S. Stephenson, Peter Agger, Paul P. Lunkenheimer, Jichao Zhao, Morten Smerup, Peter Niederer, Robert H. Anderson, and Jonathan C. Jarvis. The functional architecture of skeletal compared to cardiac musculature: Myocyte orientation, lamellar unit morphology, and the helical ventricular myocardial band. *Clinical Anatomy*, 29(3):316–332, 2016.

[3] R A Greenbaum, S Y Ho, D G Gibson, a E Becker, and R. H. Anderson. Left ventricular fibre architecture in man. *Heart*, 45(3):248–263, 3 1981.

[4] D D Streeter, Henry M Spotnitz, Dali P Patel, J Ross, and Edmund H Sonnenblick. Fiber orientation in the canine left ventricle during diastole and systole. *Circulation research*, 24(3):339–347, 1969.

[5] Larraitz Gaztañaga, Francis E. Marchlinski, and Brian P. Betensky. Mechanisms of Cardiac Arrhythmias. *Revista Española de Cardiología (English Edition)*, 65(2):174–185, 2 2012.

[6] R H Clayton, O Bernus, E M Cherry, H Dierckx, F H Fenton, L Mirabella, a V Panfilov, F B Sachse, G Seemann, and H Zhang. Models of cardiac tissue electrophysiology: progress, challenges and open questions. *Progress in biophysics and molecular biology*, 104(1-3):22–48, 1 2011.

[7] Rafael Sebastian, Viviana Zimmerman, Daniel Romero, Damian Sanchez-Quintana, and Alejandro F. Frangi. Characterization and modeling of the peripheral cardiac conduction system. *IEEE Transactions on Medical Imaging*, 32(1):45–55, 2013.

[8] Leif Sörnmo and Pablo Laguna. The Electrocardiogram-A Brief Background. In *Bioelectrical Signal Processing in Cardiac and Neurological Applications*. Elsevier, 2005.

[9] Elad Anter, David S Frankel, Francis E Marchlinski, and Sanjay Dixit. Effect of electrocardiographic lead placement on localization of outflow tract

tachycardias. *HRTHM*, 9(5):697–703, 2012.

[10] Uyen Chau Nguyên, Mark Potse, Francois Regoli, Maria Luce Caputo, Giulio Conte, Romina Murzilli, Stefano Muzzarelli, Tiziano Moccetti, Enrico G. Caiani, Frits W. Prinzen, Rolf Krause, and Angelo Auricchio. An in-silico analysis of the effect of heart position and orientation on the ECG morphology and vectorcardiogram parameters in patients with heart failure and intraventricular conduction defects. *Journal of Electrocardiology*, 48(4):617–625, 2015.

[11] Shirley A. Jones. *ECG notes: Interpretation and management guide 3rd Edition*. 2016.

[12] Christian Torp Pedersen, G. Neal Kay, Jonathan Kalman, Martin Borggrefe, Paolo Della-Bella, Timm Dickfeld, Paul Dorian, Heikki Huikuri, Youg Hoon Kim, Bradley Knight, Francis Marchlinski, David Ross, Frdric Sacher, John Sapp, Kalyanam Shivkumar, Kyoko Soejima, Hiroshi Tada, Mark E. Alexander, John K. Triedman, Takumi Yamada, Paulus Kirchhof, Gregory Y.H. Lip, Karl Heinz Kuck, Llus Mont, David Haines, Jukia Indik, John Dimarco, Derek Exner, Yoshito Iesaka, and Irene Savelieva. EHRA/HRS/APHRS Expert Consensus on Ventricular Arrhythmias. *Heart Rhythm*, 11(10):e166–e196, 2014.

[13] Bruce B. Lerman. Mechanism, diagnosis, and treatment of outflow tract tachycardia. *Nature Reviews Cardiology*, 12(10):597–608, 2015.

[14] Brian P. Betensky, Robert E. Park, Francis E. Marchlinski, Matthew D. Hutchinson, Fermin C. Garcia, Sanjay Dixit, David J. Callans, Joshua M. Cooper, Rupa Bala, David Lin, Michael P. Riley, and Edward P. Gerstenfeld. The V 2 transition ratio: A new electrocardiographic criterion for distinguishing left from right ventricular outflow tract tachycardia origin. *Journal of the American College of Cardiology*, 57(22):2255–2262, 2011.

[15] Robert D. Anderson, Saurabh Kumar, Ramanathan Parameswaran, Geoffrey Wong, Aleksandr Voskoboinik, Hariharan Sugumar, Troy Watts, Paul B. Sparks, Joseph B. Morton, Alex McLellan, Peter M. Kistler, Jonathan Kalman, and Geoffrey Lee. Differentiating Right- and Left-Sided Outflow Tract Ventricular Arrhythmias. *Circulation: Arrhythmia and Electrophysiology*, 12(6):e007392, 6 2019.

[16] Diego Penela, Marta De Riva, Csaba Herczku, Valentina Catto, Salvatore Pala, Juan Fernández-Armenta, Juan Acosta, Laura Cipolletta, David Andreu, Roger Borras, Jose Rios, Lluis Mont, Josep Brugada, Corrado Carbucicchio, Katja Zeppenfeld, and Antonio Berruezo. An easy-to-use, operator-independent, clinical model to predict the left vs. right ventricular outflow tract origin of ventricular arrhythmias. *Europace*, 17(7):1122–1128, 2015.

[17] Viatcheslav Korshunov, Diego Penela, Markus Linhart, Juan Acosta, Mikel Martinez, David Soto-Iglesias, Juan Fernández-Armenta, Francesca Vassanelli, Mario Cabrera, Roger Borràs, Beatriz Jáuregui, Jose T Ortiz-Pérez, Rosario J Perea, Xavier Bosch, Damian Sanchez-Quintana, Lluis Mont, and

Antonio Berruezo. Prediction of premature ventricular complex origin in left vs. right ventricular outflow tract: a novel anatomical imaging approach. *EP Europace*, 21(1):147–153, 1 2019.

[18] Bruce B Lerman. Mechanism of outflow tract tachycardia. *Heart Rhythm*, 4(7):973–976, 7 2007.

[19] Bastiaan J. Boukens, Ruben Coronel, and Vincent M. Christoffels. Embryonic Development of the Right Ventricular Outflow Tract and Arrhythmias. *Heart Rhythm*, 13(2):616–622, 2015.

[20] Robert H. Anderson, Timothy J. Mohun, Damian Sánchez-Quintana, Shumpei Mori, Diane E. Spicer, Jim W. Cheung, and Bruce B. Lerman. The anatomic substrates for outflow tract arrhythmias. *Heart Rhythm*, 2019.

[21] Shiro Kamakura, Wataru Shimizu, Kiyotaka Matsuo, Atsushi Taguchi, Kazuhiro Suyama, Takashi Kurita, Naohiko Aihara, Tohru Ohe, and Katsuro Shimomura. Localization of Optimal Ablation Site of Idiopathic Ventricular Tachycardia from Right and Left Ventricular Outflow Tract by Body Surface ECG. *Circulation*, pages 5–7, 1998.

[22] Takumi Yamada, H. Thomas McElderry, Harish Doppalapudi, Yoshimasa Murakami, Yukihiko Yoshida, Naoki Yoshida, Taro Okada, Naoya Tsuboi, Yasuya Inden, Toyoaki Murohara, Andrew E. Epstein, Vance J. Plumb, Satinder P. Singh, and G. Neal Kay. Idiopathic Ventricular Arrhythmias Originating From the Aortic Root. Prevalence, Electrocardiographic and Electrophysiologic Characteristics, and Results of Radiofrequency Catheter Ablation. *Journal of the American College of Cardiology*, 52(2):139–147, 2008.

[23] Andres Enriquez, Adrian Baranchuk, David Briceno, Luis Saenz, and Fermin Garcia. How to use the 12-lead ECG to predict the site of origin of idiopathic ventricular arrhythmias. *Heart Rhythm*, 16(10):1538–1544, 10 2019.

[24] Feifan Ouyang, Parwis Fotuhi, Siew Yen Ho, Joachim Hebe, Marius Volkmer, Masahiko Goya, Mark Burns, Matthias Antz, Sabine Ernst, Riccardo Cappato, and Karl-Heinz Kuck. Repetitive monomorphic ventricular tachycardia originating from the aortic sinus cusp. *Journal of the American College of Cardiology*, 39(3):500–508, 2002.

[25] Naoki Yoshida, Takumi Yamada, H. Thomas McElderry, Yasuya Inden, Masayuki Shimano, Toyoaki Murohara, Vineet Kumar, Harish Doppalapudi, Vance J. Plumb, and G. Neal Kay. A novel electrocardiographic criterion for differentiating a left from right ventricular outflow tract tachycardia origin: The V2s/V3R index. *Journal of Cardiovascular Electrophysiology*, 25(7):747–753, 2014.

[26] Naoki Yoshida, Yasuya Inden, Tomohiro Uchikawa, Hiromi Kamiya, Kazuhisa Kitamura, Masayuki Shimano, Yukiomi Tsuji, Makoto Hirai, and Toyoaki Murohara. Novel transitional zone index allows more accurate differentiation between idiopathic right ventricular outflow tract and aortic sinus cusp ventricular arrhythmias. *Heart Rhythm*, 8(3):349–356, 2011.

[27] Fengxiang Zhang, David Hamon, Zhen Fang, Yan Xu, Bing Yang, Weizhu Ju, Jason Bradfield, Kalyanam Shivkumar, Minglong Chen, and Roderick Tung. Value of a Posterior Electrocardiographic Lead for Localization of Ventricular Outflow Tract Arrhythmias: The V4/V8 Ratio. *JACC: Clinical Electrophysiology*, 3(7):678–686, 2017.

[28] Dian Cheng, Weizhu Ju, Lili Zhu, Kanghui Chen, Fengxiang Zhang, Hongwu Chen, Gang Yang, Xiaorong Li, Mingfang Li, Kai Gu, Bing Han, Jie Fan, Yazhou Lin, Kejiang Cao, Pipin Kojodjojo, Bing Yang, and Minglong Chen. V 3 R/V 7 Index. *Circulation. Arrhythmia and electrophysiology*, 11(11):e006243, 2018.

[29] Juan Acosta, Diego Penela, Csaba Herczku, Yolanda Macías, David Andreu, Juan Fernández-Armenta, Laura Cipolletta, Andres Díaz, Viatcheslav Korshunov, Josep Brugada, Lluis Mont, Jose a. Cabrera, Damian Sánchez-Quintana, and Antonio Berruezo. Impact of earliest activation site location in the septal right ventricular outflow tract for identification of left vs right outflow tract origin of idiopathic ventricular arrhythmias. *Heart Rhythm*, 12(4):726–734, 2015.

[30] Csaba Herczku, Antonio Berruezo, David Andreu, Juan Fernández-Armenta, Lluis Mont, Roger Borràs, Elena Arbelo, Jose M Tolosana, Emilce Trucco, Jose Ríos, and Josep Brugada. Mapping data predictors of a left ventricular outflow tract origin of idiopathic ventricular tachycardia with V3 transition and septal earliest activation. *Circulation. Arrhythmia and electrophysiology*, 5(3):484–91, 6 2012.

[31] Etienne M Aliot, William G Stevenson, Jesus Ma Almendral-Garrote, Frank Bogun, C Hugh Calkins, Etienne Delacretaz, Paolo Della Bella, Gerhard Hindricks, Pierre Jaïs, Mark E Josephson, Josef Kautzner, G Neal Kay, Karl-Heinz Kuck, Bruce B Lerman, Francis Marchlinski, Vivek Reddy, Martin-Jan Schalij, Richard Schilling, Kyoko Soejima, and David Wilber. EHRA/HRS Expert Consensus on Catheter Ablation of Ventricular Arrhythmias. *Europace*, 11(6):771–817, 6 2009.

[32] Ram L. Jadonath, David S. Schwartzman, Mark W. Preminger, Charles D. Gottlieb, and Francis E. Marchlinski. Utility of the 12-lead electrocardiogram in localizing the origin of right ventricular outflow tract tachycardia. *American Heart Journal*, 1995.

[33] Frank Bogun, Majid Taj, Michael Ting, Hyungjin Myra Kim, Stephen Reich, Eric Good, Krit Jongnarangsin, Aman Chugh, Frank Pelosi, Hakan Oral, and Fred Morady. Spatial resolution of pace mapping of idiopathic ventricular tachycardia/ectopy originating in the right ventricular outflow tract. *Heart Rhythm*, 5(3):339–344, 2008.

[34] Edward P. Gerstenfeld, Sanjay Dixit, David J. Callans, Yadavendra Rajawat, Robert Rho, and Francis E. Marchlinski. Quantitative comparison of spontaneous and paced 12-lead electrocardiogram during right ventricular outflow tract ventricular tachycardia. *Journal of the American College of Cardiology*,

41(11):2046–2053, 2003.

[35] Denis Noble. From the Hodgkin-Huxley axon to the virtual heart. *J Physiol*, 580(Pt 1):15–22, 2007.

[36] Natalia A Trayanova. Whole-heart modeling: applications to cardiac electrophysiology and electromechanics. *Circ Res*, 108(1):113–128, 2011.

[37] Edward Vigmond, Fijoy Vadakkumpadan, Viatcheslav Gurev, Hermenegild Arevalo, Makarand Deo, Gernot Plank, and Natalia Trayanova. Towards predictive modelling of the electrophysiology of the heart. *Exp Physiol*, 94(5):563–577, 5 2009.

[38] Hermenegild J. Arevalo, Fijoy Vadakkumpadan, Eliseo Guallar, Alexander Jebb, Peter Malamas, Katherine C. Wu, and Natalia A. Trayanova. Arrhythmia risk stratification of patients after myocardial infarction using personalized heart models. *Nature Communications*, 7(May):11437, 2016.

[39] Alejandro Lopez-Perez, Rafael Sebastian, and Jose M Ferrero. Three-dimensional cardiac computational modelling: methods, features and applications. *BioMedical Engineering OnLine*, 14(1):35, 2015.

[40] Alejandro Lopez-Perez, Rafael Sebastian, M. Izquierdo, Ricardo Ruiz, Martin Bishop, and Jose Maria Ferrero. Personalized cardiac computational models: from clinical data to simulation of infarct-related ventricular tachycardia. *Frontiers in Physiology*, 10(May):580, 2019.

[41] Alfonso Santiago, Jazmin Aguado-Sierra, Miguel Zavala-Aké, Ruben Doste, Samuel Gómez, Ruth Arís, Juan C Cajas, Eva Casoni, and Mariano Vázquez. Fully coupled fluid-electro-mechanical model of the human heart for supercomputers. *International Journal for Numerical Methods in Biomedical Engineering*, 34(12):e3140, 12 2018.

[42] Christoph M. Augustin, Aurel Neic, Manfred Liebmann, Anton J. Prassl, Steven A. Niederer, Gundolf Haase, and Gernot Plank. Anatomically accurate high resolution modeling of human whole heart electromechanics: A strongly scalable algebraic multigrid solver method for nonlinear deformation. *Journal of Computational Physics*, 305:622–646, 2016.

[43] Sophie Giffard-Roisin, Thomas Jackson, Lauren Fovargue, Jack Lee, Herve Delingette, Reza Razavi, Nicholas Ayache, and Maxime Sermesant. Non-Invasive Personalisation of a Cardiac Electrophysiology Model from Body Surface Potential Mapping. *IEEE Transactions on Biomedical Engineering*, pages 1–1, 2016.

[44] Nicolas Cedilnik, Josselin Duchateau, Remi Dubois, Frederic Sacher, Pierre Jaïs, Hubert Cochet, and Maxime Sermesant. Fast personalized electrophysiological models from computed tomography images for ventricular tachycardia ablation planning. *Europace*, 20:94–101, 2018.

[45] Jun Ichi Okada, Takumi Washio, Machiko Nakagawa, Masahiro Watanabe, Yoshimasa Kadooka, Taro Kariya, Hiroshi Yamashita, Yoko Yamada, Shin Ichi Momomura, Ryozo Nagai, Toshiaki Hisada, and Seiryo Sugiura. Absence of rapid propagation through the Purkinje network as a potential

cause of line block in the human heart with left bundle branch block. *Frontiers in Physiology*, 9(FEB):1–10, 2018.

[46] Hans C van Assen, Mikhail G Danilouchkine, Alejandro F Frangi, Sebastian Ordás, Jos J M Westenberg, Johan H C Reiber, and Boudewijn P F Lelieveldt. SPASM: a 3D-ASM for segmentation of sparse and arbitrarily oriented cardiac MRI data. *Med Image Anal*, 10(2):286–303, 2006.

[47] Alistair A Young and Alejandro F Frangi. Computational cardiac atlases: from patient to population and back. *Exp Physiol*, 94(5):578–596, 5 2009.

[48] Jean-Marc Peyrat, Maxime Sermesant, Xavier Pennec, Herv Delingette, Chenyang Xu, Elliot R McVeigh, and Nicholas Ayache. A computational framework for the statistical analysis of cardiac diffusion tensors: application to a small database of canine hearts. *IEEE Trans Med Imaging*, 26(11):1500–1514, 11 2007.

[49] Alejandro F Frangi, Daniel Rueckert, Julia A Schnabel, and Wiro J Niessen. Automatic construction of multiple-object three-dimensional statistical shape models: application to cardiac modeling. *IEEE Trans Med Imaging*, 21(9):1151–1166, 9 2002.

[50] Maria Lorenzo-Valdés, Gerardo I Sanchez-Ortiz, Andrew G Elkington, Raad H Mohiaddin, and Daniel Rueckert. Segmentation of 4D cardiac MR images using a probabilistic atlas and the EM algorithm. *Med Image Anal*, 8(3):255–265, 9 2004.

[51] Maxime Sermesant, Jean-Marc Peyrat, Phani Chinchapatnam, Florence Billet, Tommaso Mansi, Kawal Rhode, Herve Delingette, Reza Razavi, and Nicholas Ayache. Toward patient-specific myocardial models of the heart. *Heart Fail Clin*, 4(3):289–301, 7 2008.

[52] Roy C P Kerckhoffs, Andrew D McCulloch, Jeffrey H Omens, and Lawrence J Mulligan. Effects of biventricular pacing and scar size in a computational model of the failing heart with left bundle branch block. *Med Image Anal*, 13(2):362–369, 2009.

[53] Natalia A Trayanova, Thomas O'Hara, Jason D Bayer, Patrick M Boyle, Kathleen S McDowell, Jason Constantino, Hermenegild J Arevalo, Yuxuan Hu, and Fijoy Vadakkumpadan. Computational cardiology: how computer simulations could be used to develop new therapies and advance existing ones. *Europace*, 14 Suppl 5:v82–v89, 11 2012.

[54] Kathleen S McDowell, Hermenegild J Arevalo, Mary M Maleckar, and Natalia A Trayanova. Susceptibility to arrhythmia in the infarcted heart depends on myofibroblast density. *Biophys J*, 101(6):1307–1315, 9 2011.

[55] Y Rudy and R Plonsey. A comparison of volume conductor and source geometry effects on body surface and epicardial potentials. *Circ Res*, 46(2):283–291, 2 1980.

[56] S Abboud, O Berenfeld, and D Sadeh. Simulation of high-resolution QRS complex using a ventricular model with a fractal conduction system. Effects of ischemia on high-frequency QRS potentials. *Circulation Research*,

68(6):1751–1760, 6 1991.

[57] C P Bradley, A J Pullan, and P J Hunter. Geometric modeling of the human torso using cubic hermite elements. *Ann Biomed Eng*, 25(1):96–111, 1997.

[58] C P Bradley, A J Pullan, and P J Hunter. Effects of material properties and geometry on electrocardiographic forward simulations. *Ann Biomed Eng*, 28(7):721–741, 7 2000.

[59] Robert S. MacLeod, Christopher R Johnson, and Philip R Ershler. Construction of an inhomogeneous model of the human torso for use in computational electrocardiography. *Proceedings of the Annual Conference on Engineering in Medicine and Biology*, 13(2):688–689, 1991.

[60] Oleg V. Aslanidi, Michael A. Colman, Jonathan Stott, Halina Dobrzynski, Mark R. Boyett, Arun V. Holden, and Henggui Zhang. 3D virtual human atria: A computational platform for studying clinical atrial fibrillation. *Progress in Biophysics and Molecular Biology*, 107(1):156–168, 2011.

[61] Jana Lenkova, Jana Svehlikova, and Milan Tysler. Individualized model of torso surface for the inverse problem of electrocardiology. *J Electrocardiol*, 45(3):231–236, 2012.

[62] Martin W. Krueger, Gunnar Seemann, Kawal Rhode, D. U.J. Keller, Christopher Schilling, Aruna Arujuna, Jaswinder Gill, Mark D. O'Neill, Reza Razavi, and Olaf Dossel. Personalization of atrial anatomy and electrophysiology as a basis for clinical modeling of radio-frequency ablation of atrial fibrillation. *IEEE Transactions on Medical Imaging*, 32(1):73–84, 2013.

[63] Darren A Hooks, Karl A Tomlinson, Scott G Marsden, Ian J LeGrice, Bruce H Smaill, Andrew J Pullan, and Peter J Hunter. Cardiac microstructure: implications for electrical propagation and defibrillation in the heart. *Circ Res*, 91(4):331–338, 2002.

[64] Ian LeGrice, Greg Sands, Darren Hooks, Dane Gerneke, and Bruce Smaill. Microscopic imaging of extended tissue volumes. *Clin Exp Pharmacol Physiol*, 31(12):902–905, 2004.

[65] Bruce H Smaill, Ian J LeGrice, Darren A Hooks, Andrew J Pullan, Bryan J Caldwell, and Peter J Hunter. Cardiac structure and electrical activation: models and measurement. *Clin Exp Pharmacol Physiol*, 31(12):913–919, 2004.

[66] Daniel Romero, Rafael Sebastian, Bart H Bijnens, Viviana Zimmerman, Patrick M Boyle, Edward J Vigmond, and Alejandro F Frangi. Effects of the purkinje system and cardiac geometry on biventricular pacing: a model study. *Ann Biomed Eng*, 38(4):1388–1398, 2010.

[67] Siew Yen Ho, Damian Sanchez-Quintana, Jose Angel Cabrera, and Robert H. Anderson. Anatomy of the left atrium: implications for radiofrequency ablation of atrial fibrillation. *Journal of cardiovascular electrophysiology*, 10(11):1525–33, 11 1999.

[68] Damian Sanchez-Quintana and Siew Yen Ho. [Anatomy of cardiac nodes and

atrioventricular specialized conduction system]. *Revista espanola de cardiologia*, 56(11):1085–92, 2003.

[69] Fijoy Vadakkumpadan, Hermenegild Arevalo, Can Ceritoglu, Michael Miller, and Natalia Trayanova. Image-based estimation of ventricular fiber orientations for personalized modeling of cardiac electrophysiology. *IEEE Trans Med Imaging*, 48(Suppl 2):1–6, 2012.

[70] J. D. Bayer, R. C. Blake, G. Plank, and N. A. Trayanova. A novel rule-based algorithm for assigning myocardial fiber orientation to computational heart models. *Annals of Biomedical Engineering*, 40(10):2243–2254, 2012.

[71] DE Roberts, LT Hersh, and AM Scher. Influence of Cardiac Fiber Orientation on Wavefront Voltage, Conduction Velocity, and Tissue Resistivity in the Dog. *Circulation Research*, 44:701–712, 1979.

[72] Bonnie B. Punske, Bruno Taccardi, Bruce Steadman, Philip R. Ershler, Alice England, Maria L. Valencik, John A. McDonald, and Sheldon E. Litwin. Effect of fiber orientation on propagation: Electrical mapping of genetically altered mouse hearts. *Journal of Electrocardiology*, 38(4 SUPPL.):40–44, 2005.

[73] P S Chen, Y M Cha, B B Peters, and L S Chen. Effects of myocardial fiber orientation on the electrical induction of ventricular fibrillation. *The American journal of physiology*, 264(6 Pt 2):1760–73, 1993.

[74] L K Waldman, D Nosan, F Villarreal, and J W Covell. Relation between transmural deformation and local myofiber direction in canine left ventricle. *Circulation research*, 63(3):550–562, 1988.

[75] Paul P. Lunkenheimer, Klaus Redmann, Philipp Westermann, Kay Rothaus, Colin W. Cryer, Peter Niederer, and Robert H. Anderson. The myocardium and its fibrous matrix working in concert as a spatially netted mesh: a critical review of the purported tertiary structure of the ventricular mass. *European Journal of Cardio-thoracic Surgery*, 29(SUPPL. 1):41–49, 2006.

[76] M. Smerup, J. Partridge, P. Agger, S. Ringgaard, M. Pedersen, S. Petersen, J. M. Hasenkam, P. Niederer, P. P. Lunkenheimer, and R. H. Anderson. A mathematical model of the mechanical link between shortening of the cardiomyocytes and systolic deformation of the left ventricular myocardium. *Technology and Health Care*, 21(1):63–79, 2013.

[77] Marieke Pluijmert, Tammo Delhaas, Adrian Flores de la Parra, Wilco Kroon, Frits W. Prinzen, and Peter H M Bovendeerd. Determinants of biventricular cardiac function: a mathematical model study on geometry and myofiber orientation. *Biomechanics and Modeling in Mechanobiology*, pages 1–9, 2016.

[78] Rafael Sebastian, Viviana Zimmerman, Daniel Romero, and Alejandro F. Frangi. Construction of a computational anatomical model of the peripheral cardiac conduction system. *IEEE Transactions on Biomedical Engineering*, 58(12 PART 2):3479–3482, 2011.

[79] B Sakmann and E Neher. Patch clamp techniques for studying ionic channels in excitable membranes. *Annu Rev Physiol*, 46:455–472, 1984.

[80] A L Hodgkin and A F Huxley. A quantitative description of membrane current and its application to conduction and excitation in nerve. 1952. *Bull Math Biol*, 52(1-2):23–25, 1990.

[81] C H Luo and Y Rudy. A dynamic model of the cardiac ventricular action potential. I. Simulations of ionic currents and concentration changes. *Circ Res*, 74(6):1071–1096, 6 1994.

[82] R L Winslow, J Rice, S Jafri, E Marbán, and B O'Rourke. Mechanisms of altered excitation-contraction coupling in canine tachycardia-induced heart failure, II: model studies. *Circ Res*, 84(5):571–586, 3 1999.

[83] A Nygren, C Fiset, L Firek, J W Clark, D S Lindblad, R B Clark, and W R Giles. Mathematical model of an adult human atrial cell: the role of K+ currents in repolarization. *Circ Res*, 82(1):63–81, 1998.

[84] Mary M Maleckar, Joseph L Greenstein, Wayne R Giles, and Natalia A Trayanova. K+ current changes account for the rate dependence of the action potential in the human atrial myocyte. *Am J Physiol Heart Circ Physiol*, 297(4):1398–410, 10 2009.

[85] R. Wilders, H. J. Jongsma, and A. C. van Ginneken. Pacemaker activity of the rabbit sinoatrial node. A comparison of mathematical models. *Biophysical Journal*, 60(5):1202–1216, 1991.

[86] D DiFrancesco and D Noble. A model of cardiac electrical activity incorporating ionic pumps and concentration changes. *Philos Trans R Soc Lond B Biol Sci*, 307(1133):353–398, 1985.

[87] Philip Stewart, Oleg V Aslanidi, Denis Noble, Penelope J Noble, Mark R Boyett, and Henggui Zhang. Mathematical models of the electrical action potential of Purkinje fibre cells. *Philos Trans A Math Phys Eng Sci*, 367(1896):2225–2255, 6 2009.

[88] K.H.W.J. ten Tusscher, D Noble, P J Noble, and A V Panfilov. A model for human ventricular tissue. *AJP - Heart and Circulatory Physiology*, 286(4):H1573–H1589, 2004.

[89] Thomas O'Hara, Laszlo Virag, Andras Varro, and Yoram Rudy. Simulation of the undiseased human cardiac ventricular action potential: Model formulation and experimental validation. *PLoS Computational Biology*, 7(5), 2011.

[90] Colleen C. Mitchell and David G. Schaeffer. A two-current model for the dynamics of cardiac membrane. *Bulletin of Mathematical Biology*, 65(5):767–793, 2003.

[91] Alfonso Bueno-Orovio, Elizabeth M. Cherry, and Flavio H. Fenton. Minimal model for human ventricular action potentials in tissue. *Journal of Theoretical Biology*, 253(3):544–560, 2008.

[92] P M Nielsen, I J Le Grice, B H Smaill, and P J Hunter. Mathematical model of geometry and fibrous structure of the heart. *Am J Physiol*, 260(4 Pt 2):1365–78, 1991.

[93] Mark Potse, Bruno Dubé, Alain Vinet, and Rene Cardinal. A comparison of monodomain and bidomain propagation models for the human heart. *Annual International Conference of the IEEE Engineering in Medicine and Biology - Proceedings*, 53(12):3895–3898, 2006.

[94] Chris Bradley, Andy Bowery, Randall Britten, Vincent Budelmann, Oscar Camara, Richard Christie, Andrew Cookson, Alejandro F Frangi, Thiranja Babarenda Gamage, Thomas Heidlauf, Sebastian Krittian, David Ladd, Caton Little, Kumar Mithraratne, Martyn Nash, David Nickerson, Poul Nielsen, Oyvind Nordbø, Stig Omholt, Ali Pashaei, David Paterson, Vijayaraghavan Rajagopal, Adam Reeve, Oliver Röhrle, Soroush Safaei, Rafael Sebastián, Martin Steghöfer, Tim Wu, Ting Yu, Heye Zhang, and Peter Hunter. OpenCMISS: a multi-physics & multi-scale computational infrastructure for the VPH/Physiome project. *Prog Biophys Mol Biol*, 107(1):32–47, 10 2011.

[95] Elvio A. Heidenreich, Jose M. Ferrero, Manuel Doblaré, and Jose F. Rodríguez. Adaptive Macro Finite Elements for the Numerical Solution of Monodomain Equations in Cardiac Electrophysiology. *Annals of Biomedical Engineering*, 38(7):2331–2345, 7 2010.

[96] M L Buist and A J Pullan. From cell to body surface: a fully coupled approach. *J Electrocardiol*, 34 Suppl:191–195, 2001.

[97] Ana Ferrer, Rafael Sebastian, Damian Sánchez-Quintana, Jose F. Rodríguez, Eduardo J. Godoy, Laura Martínez, and Javier Saiz. Detailed Anatomical and Electrophysiological Models of Human Atria and Torso for the Simulation of Atrial Activation. *Plos One*, 10(11):e0141573, 2015.

[98] Mary C MacLachlan, Joakim Sundnes, and Glenn Terje Lines. Simulation of ST segment changes during subendocardial ischemia using a realistic 3-D cardiac geometry. *IEEE Trans Biomed Eng*, 52(5):799–807, 5 2005.

[99] B Dubé, R M Gulrajani, M Lorange, A R LeBlanc, J Nasmith, and R A Nadeau. A computer heart model incorporating anisotropic propagation. IV. Simulation of regional myocardial ischemia. *J Electrocardiol*, 29(2):91–103, 1996.

[100] O Okazaki, Y Yamauchi, M Kashida, K Izumo, N Akatsuka, S Ohnishi, M Shoda, T Nirei, H Kasanuki, M Ebato, S Mashima, K Harumi, and D Wei. Possible mechanism of ECG features in patients with idiopathic ventricular fibrillation studied by heart model and computer simulation. *J Electrocardiol*, 30 Suppl:98–104, 1998.

[101] J E Burnes, B Taccardi, and Y Rudy. A noninvasive imaging modality for cardiac arrhythmias. *Circulation*, 102(17):2152–2158, 10 2000.

[102] Z Xu, R M Gulrajani, F Molin, M Lorange, B Dubé, P Savard, and R A Nadeau. A computer heart model incorporating anisotropic propagation. III. Simulation of ectopic beats. *J Electrocardiol*, 29(2):73–90, 1996.

[103] A J Pullan, L K Cheng, M P Nash, C P Bradley, and D J Paterson. Noninvasive electrical imaging of the heart: theory and model development. *Ann*

Biomed Eng, 29(10):817–836, 10 2001.

[104] David U J Keller, Frank M Weber, Gunnar Seemann, and Olaf Dössel. Ranking the influence of tissue conductivities on forward-calculated ECGs. *IEEE Trans Biomed Eng*, 57(7):1568–1576, 7 2010.

[105] Eduardo Jorge Godoy, Miguel Lozano, Ignacio García-Fernández, Ana Ferrer-Albero, Rob MacLeod, Javier Saiz, and Rafael Sebastian. Atrial fibrosis hampers non-invasive localization of atrial ectopic foci from multielectrode signals: A 3D Simulation Study. *Frontiers in Physiology*, 9(MAY), 2018.

[106] Louie Cardone-Noott, Alfonso Bueno-Orovio, Ana Mincholé, Nejib Zemzemi, and Blanca Rodriguez. Human ventricular activation sequence and the simulation of the electrocardiographic QRS complex and its variability in healthy and intraventricular block conditions. *EP Europace*, 18(suppl_4):iv4–iv15, 12 2016.

[107] Ana Mincholé and Blanca Rodriguez. Artificial intelligence for the electrocardiogram. *Nature Medicine*, 25(1):22–23, 2019.

[108] Aurore Lyon, Ana Mincholé, Juan Pablo Martínez, Pablo Laguna, and Blanca Rodriguez. Computational techniques for ECG analysis and interpretation in light of their contribution to medical advances. *Journal of the Royal Society Interface*, 15(138), 2018.

[109] Kei Ichiro Minami, Hiroshi Nakajima, and Takeshi Toyoshima. Real-time discrimination of ventricular tachyarrhythmia with fourier-transform neural network. *IEEE Transactions on Biomedical Engineering*, 46(2):179–185, 1999.

[110] Himanshu Gothwal, Silky Kedawat, and Rajesh Kumar. Cardiac arrhythmias detection in an ECG beat signal using fast fourier transform and artificial neural network. *Journal of Biomedical Science and Engineering*, 04(04):289–296, 2011.

[111] Yasin Kaya and Hseyin Pehlivan. Classification of Premature Ventricular Contraction in ECG. *International Journal of Advanced Computer Science and Applications*, 6(7):34–40, 2015.

[112] Ana Ferrer-Albero, Eduardo J Godoy, Miguel Lozano, Laura Martinez-Mateu, Felipe Atienza, Javier Saiz, and Rafael Sebastian. Non-invasive localization of atrial ectopic beats by using simulated body surface P-wave integral maps. *PLoS One*, 12(7):e0181263, 2017.

[113] Damian Sanchez-Quintana, Virginio Garcia-Martinez, and Juan M. Hurle. Myocardial Fiber Architecture in the Human Heart. *Cells Tissues Organs*, 138(4):352–358, 1990.

[114] Df Scollan, a Holmes, J Zhang, and Rl Winslow. Reconstruction of cardiac ventricular geometry and fiber orientation using magnetic resonance imaging. *Annals of biomedical Enigneering*, 28(8):934–944, 2000.

[115] P S Jouk, Y Usson, G Michalowicz, and L Grossi. Three-dimensional car-

tography of the pattern of the myofibres in the second trimester fetal human heart. *Anatomy and embryology*, 202(2):103–118, 2000.

[116] Anna Gonzalez-Tendero, Chong Zhang, Vedrana Balicevic, Ruben Cárdenes, Sven Loncaric, Constantine Butakoff, Bruno Paun, Anne Bonnin, Patricia Garcia-Cañadilla, Emma Muñoz-Moreno, Eduard Gratacós, Fatima Crispi, and Bart Bijnens. Whole heart detailed and quantitative anatomy, myofibre structure and vasculature from X-ray phase-contrast synchrotron radiation-based micro computed tomography. *European Heart Journal - Cardiovascular Imaging*, pages 732–741, 2017.

[117] Francois Varray, Iulia Mirea, Max Langer, Francoise Peyrin, Laurent Fanton, and Isabelle E. Magnin. Extraction of the 3D local orientation of myocytes in human cardiac tissue using X-ray phase-contrast micro-tomography and multi-scale analysis. *Medical Image Analysis*, 38:117–132, 2017.

[118] Robert S. Stephenson, Andrew Atkinson, Petros Kottas, Filip Perde, Fatemeh Jafarzadeh, Mike Bateman, Paul A. Iaizzo, Jichao Zhao, Henggui Zhang, Robert H. Anderson, Jonathan C. Jarvis, and Halina Dobrzynski. High resolution 3-Dimensional imaging of the human cardiac conduction system from microanatomy to mathematical modeling. *Scientific Reports*, 7(1):7188, 2017.

[119] Nicolas Toussaint, Christian T. Stoeck, Tobias Schaeffter, Sebastian Kozerke, Maxime Sermesant, and Philip G. Batchelor. In vivo human cardiac fibre architecture estimation using shape-based diffusion tensor processing. *Medical Image Analysis*, 17(8):1243–1255, 2013.

[120] Sonia Nielles-Vallespin, Choukri Mekkaoui, Peter Gatehouse, Timothy G. Reese, Jennifer Keegan, Pedro F. Ferreira, Steve Collins, Peter Speier, Thorsten Feiweier, Ranil De Silva, Marcel P. Jackowski, Dudley J. Pennell, David E. Sosnovik, and David Firmin. In vivo diffusion tensor MRI of the human heart: Reproducibility of breath-hold and navigator-based approaches. *Magnetic Resonance in Medicine*, 70(2):454–465, 2013.

[121] Constantin von Deuster, Eva Sammut, Liya Asner, David Nordsletten, Pablo Lamata, Christian T Stoeck, Sebastian Kozerke, and Reza Razavi. Studying Dynamic Myofiber Aggregate Reorientation in Dilated Cardiomyopathy Using In Vivo Magnetic Resonance Diffusion Tensor Imaging. *Circulation. Cardiovascular imaging*, 9(10):e005018, 2016.

[122] Jean Marc Peyrat, Maxime Sermesant, Xavier Pennec, Herve Delingette, Chenyang Xu, Elliot R. McVeigh, and Nicholas Ayache. A computational framework for the statistical analysis of cardiac diffusion tensors: Application to a small database of canine hearts. *IEEE Transactions on Medical Imaging*, 26(10):1500–1514, 2007.

[123] Herve Lombaert, Jean Marc Peyrat, Pierre Croisille, Stanislas Rapacchi, Laurent Fanton, Patrick Clarysse, Herve Delingette, and Nicholas Ayache. Statistical analysis of the human cardiac fiber architecture from DT-MRI. *Functional Imaging and Modeling of the Heart*, 6666 LNCS:171–179, 2011.

[124] Herve Lombaert, Jean Marc Peyrat, Pierre Croisille, Stanislas Rapacchi,

Laurent Fanton, Farida Cheriet, Patrick Clarysse, Isabelle Magnin, Herve Delingette, and Nicholas Ayache. Human atlas of the cardiac fiber architecture: Study on a healthy population. *IEEE Transactions on Medical Imaging*, 31(7):1436–1447, 2012.

[125] Karim Lekadir, Corne Hoogendoorn, Marco Pereanez, Xenia Alba, Ali Pashaei, and Alejandro F. Frangi. Statistical personalization of ventricular fiber orientation using shape predictors. *IEEE Transactions on Medical Imaging*, 33(4):882–890, 2014.

[126] P. M. Nielsen, I. J. Le Grice, B. H. Smaill, and P. J. Hunter. Mathematical model of geometry and fibrous structure of the heart. *The American journal of physiology*, 260(4 Pt 2):1365–1378, 1991.

[127] Jonathan Wong and Ellen Kuhl. Generating fibre orientation maps in human heart models using Poisson interpolation. *Computer methods in biomechanics and biomedical engineering*, 17(11):1217–26, 2012.

[128] Andreas Nagler, Michael Gee, and Wolfgang Wall. Personalization of Cardiac Fiber Orientations from Image Data Using the Unscented Kalman Filter. *FIMH*, pages 132–140, 2013.

[129] Peter Agger, Robert S. Stephenson, Halina Dobrzynski, Andrew Atkinson, Paul A. Iaizzo, Robert H. Anderson, Jonathan C. Jarvis, Sarah L. Allan, John B. Partridge, Jichao Zhao, Henggui Zhang, and David H. MacIver. Insights from echocardiography, magnetic resonance imaging, and microcomputed tomography relative to the mid-myocardial left ventricular echogenic zone. *Echocardiography*, 33(10):1546–1556, 2016.

[130] P Boettler, P Claus, L Herbots, M McLaughlin, J D'hooge, B Bijnens, S Y Ho, D Kececioglu, and G R Sutherland. New aspects of the ventricular septum and its function: an echocardiographic study. *Heart (British Cardiac Society)*, 91(10):1343–1348, 2005.

[131] Mladen J. Kocica, Antonio F. Corno, Francesc Carreras-Costa, Manel Ballester-Rodes, Mark C. Moghbel, Clotario N C Cueva, Vesna Lackovic, Vladimir I. Kanjuh, and Francisco Torrent-Guasp. The helical ventricular myocardial band: global, three-dimensional, functional architecture of the ventricular myocardium. *European Journal of Cardio-thoracic Surgery*, 29(SUPPL. 1), 2006.

[132] Omar Abouezzeddine, Mahmoud Suleiman, Traci Buescher, Suraj Kapa, Paul A. Friedman, Arshad Jahangir, Jennifer A. Mears, Dorothy J. Ladewig, Thomas M. Munger, Stephen C. Hammill, Douglas L. Packer, and Samuel J. Asirvatham. Relevance of endocavitary structures in ablation procedures for ventricular tachycardia. *Journal of Cardiovascular Electrophysiology*, 21(3):245–254, 2010.

[133] A. Crozier, C. M. Augustin, A. Neic, A. J. Prassl, M. Holler, T. E. Fastl, A. Hennemuth, K. Bredies, T. Kuehne, M. J. Bishop, S. A. Niederer, and G. Plank. Image-Based Personalization of Cardiac Anatomy for Coupled Electromechanical Modeling. *Annals of Biomedical Engineering*, 44(1):58–

70, 2016.

[134] A. Palit, G. A. Turley, S. K. Bhudia, R. Wellings, and M. A. Williams. Assigning Myocardial Fibre Orientation to a Computational Biventricular Human Heart Model. In James Goh, editor, *IFMBE Proceedings*, volume 43 of *IFMBE Proceedings*, pages 144–147, Cham, 2014. Springer International Publishing.

[135] Tomas Möller and Ben Trumbore. Fast, Minimum Storage Ray/Triangle Intersection. *Journal of Graphics Tools*, 2(1):21–28, 1997.

[136] Peter Agger, Satyan Lakshminrusimha, Christoffer Laustsen, Sylvia Gugino, Jesper R. Frandsen, Morten Smerup, Robert H. Anderson, Vibeke Hjortdal, and Robin H. Steinhorn. The myocardial architecture changes in persistent pulmonary hypertension of the newborn in an ovine animal model. *Pediatric Research*, 79(4):565–574, 4 2016.

[137] S Y Ho and P Nihoyannopoulos. Anatomy, echocardiography, and normal right ventricular dimensions. *Heart (British Cardiac Society)*, 92 Suppl 1(C):i2–i13, 2006.

[138] Paul P. Lunkenheimer, Peter Niederer, Damian Sanchez-Quintana, Margarita Murillo, and Morten Smerup. Models of ventricular structure and function reviewed for clinical cardiologists. *Journal of Cardiovascular Translational Research*, 6(2):176–186, 2013.

[139] Manuel D Cerqueira, Neil J Weissman, Vasken Dilsizian, Alice K Jacobs, Sanjiv Kaul, Warren K Laskey, Dudley J Pennell, John A Rumberger, Thomas Ryan, and Mario S Verani. Standardized Myocardial Segmentation and Nomenclature for Tomographic Imaging of the Heart. *Circulation*, 105:539–542, 2002.

[140] L. Zhong, L. Gobeawan, Y. Su, J.-L. Tan, D. Ghista, T. Chua, R.-S. Tan, and G. Kassab. Right ventricular regional wall curvedness and area strain in patients with repaired tetralogy of Fallot. *AJP: Heart and Circulatory Physiology*, 302(6):H1306–H1316, 2012.

[141] Colleen C Mitchell and David G Schaeffer. A two-current model for the dynamics of cardiac membrane. *Bulletin of mathematical biology*, 65(5):767–793, 9 2003.

[142] Hugo Talbot, Stphanie Marchesseau, Christian Duriez, Maxime Sermesant, Stphane Cotin, and Herv Delingette. Towards an interactive electromechanical model of the heart. *Interface focus*, 3(2):20120091, 2013.

[143] R. Sebastian, V. Zimmerman, F. Sukno, B. B. Bijnens, and A. F. Frangi. Cardiac modelling for pathophysiology research and clinical applications. The need for an automated pipeline. *IFMBE Proceedings*, 25(4):2207–2210, 2009.

[144] Dongdong Deng, Hermenegild Arevalo, Farhad Pashakhanloo, Adityo Prakosa, Hiroshi Ashikaga, Elliot McVeigh, Henry Halperin, and Natalia Trayanova. Accuracy of prediction of infarct-related arrhythmic circuits from image-based models reconstructed from low and high resolution MRI. *Frontiers in Physiology*, 6(OCT):1–12, 2015.

[145] Mark E. Josephson, Harvey L. Waxman, Michael E. Cain, Martin J. Gardner, and Alfred E. Buxton. Ventricular activation during ventricular endocardial pacing. II. Role of pace-mapping to localize origin of ventricular tachycardia. *The American Journal of Cardiology*, 50(1):11–22, 1982.

[146] Takumi Yamada, Naoki Yoshida, Yoshimasa Murakami, Taro Okada, Masahiro Muto, Toyoaki Murohara, Hugh T. McElderry, and G. Neal Kay. Electrocardiographic characteristics of ventricular arrhythmias originating from the junction of the left and right coronary sinuses of Valsalva in the aorta: The activation pattern as a rationale for the electrocardiographic characteristics. *Heart Rhythm*, 5(2):184–192, 2008.

[147] Shuaib Latif, Sanjay Dixit, and David J Callans. Ventricular Arrhythmias in Normal Hearts. *Cardiology clinics*, 26:367–380, 2008.

[148] Andres Enriquez, Federico Malavassi, Luis C. Saenz, Gregory Supple, Pasquale Santangeli, Francis E. Marchlinski, and Fermin C. Garcia. How to map and ablate left ventricular summit arrhythmias. *Heart Rhythm*, 14(1):141–148, 2017.

[149] Ruben Doste, David Soto-Iglesias, Gabriel Bernardino, Alejandro Alcaine, Rafael Sebastian, Sophie Giffard-Roisin, Maxime Sermesant, Antonio Berruezo, Damian Sanchez-Quintana, and Oscar Camara. A rule-based method to model myocardial fiber orientation in cardiac biventricular geometries with outflow tracts. *International Journal for Numerical Methods in Biomedical Engineering*, 35(4):e3185, 4 2019.

[150] Patrick M. Boyle, Tarek Zghaib, Sohail Zahid, Rheeda L. Ali, Dongdong Deng, William H. Franceschi, Joe B. Hakim, Michael J. Murphy, Adityo Prakosa, Stefan L. Zimmerman, Hiroshi Ashikaga, Joseph E. Marine, Aravindan Kolandaivelu, Saman Nazarian, David D. Spragg, Hugh Calkins, and Natalia A. Trayanova. Computationally guided personalized targeted ablation of persistent atrial fibrillation. *Nature Biomedical Engineering*, pages 1–10, 2019.

[151] Steven A. Niederer, Joost Lumens, and Natalia A. Trayanova. Computational models in cardiology. *Nature Reviews Cardiology*, 16(2):100–111, 2019.

[152] Jun Ichi Okada, Teruyoshi Sasaki, Takumi Washio, Hiroshi Yamashita, Taro Kariya, Yasushi Imai, Machiko Nakagawa, Yoshimasa Kadooka, Ryozo Nagai, Toshiaki Hisada, and Seiryo Sugiura. Patient Specific Simulation of Body Surface ECG using the Finite Element Method. *PACE - Pacing and Clinical Electrophysiology*, 36(3):309–321, 2013.

[153] Sophie Giffard-Roisin, Herve Delingette, Thomas Jackson, Jessica Webb, Lauren Fovargue, Jack Lee, Christopher A Rinaldi, Reza Razavi, Nicholas Ayache, and Maxime Sermesant. Transfer Learning From Simulations on a Reference Anatomy for ECGI in Personalized Cardiac Resynchronization Therapy. *IEEE Transactions on Biomedical Engineering*, 66(2):343–353, 2 2019.

[154] Nirmal Panthee, Jun-Ichi Okada, Takumi Washio, Youhei Mochizuki, Ryohei

Suzuki, Hidekazu Koyama, Minoru Ono, Toshiaki Hisada, and Seiryo Sugiura. Tailor-made heart simulation predicts the effect of cardiac resynchronization therapy in a canine model of heart failure. *Medical image analysis*, 31:46–62, 2016.

[155] Mohammed Alawad and Linwei Wang. Learning domain shift in simulated and clinical data: Localizing the origin of ventricular activation from 12-lead electrocardiograms. *IEEE Transactions on Medical Imaging*, 38(5):1172–1184, 2019.

[156] Andony Arrieula, Hubert Cochet, Pierre Jaïs, Michel Haïssaguerre, Mark Potse, Inria Bordeaux Sud-ouest, I H U Liryc, and Bordeaux Université. In-silico evaluation of an iterative pace-mapping technique to guide catheter ablation of ventricular ectopy. In *Computing in Cardiology (CinC).*, pages 1–4, 2019.

[157] William E. Lorensen and Harvey E. Cline. Marching cubes: A high resolution 3D surface construction algorithm. *Proceedings of the 14th annual conference on Computer graphics and interactive techniques - SIGGRAPH '87*, 21(4):163–169, 1987.

[158] Hang Si. TetGen, a Quality Tetrahedral Mesh Generator. *AMC Transactions on Mathematical Software*, 41(2):11, 2015.

[159] Peter Taggart, Peter MI Sutton, Tobias Opthof, Ruben Coronel, Richard Trimlett, Wilfred Pugsley, and Panny Kallis. Inhomogeneous transmural conduction during early ischaemia in patients with coronary artery disease. *Journal of Molecular and Cellular Cardiology*, 32(4):621–630, 2000.

[160] Jason Bayer, Anton J. Prassl, Ali Pashaei, Juan F. Gomez, Antonio Frontera, Aurel Neic, Gernot Plank, and Edward J. Vigmond. Universal ventricular coordinates: A generic framework for describing position within the heart and transferring data. *Medical Image Analysis*, 45(February):83–93, 2018.

[161] Laura Martinez-Mateu, Lucia Romero, Ana Ferrer-Albero, Rafael Sebastian, Jose F. Rodríguez Matas, Jose Jalife, Omer Berenfeld, and Javier Saiz. Factors affecting basket catheter detection of real and phantom rotors in the atria: A computational study. *PLOS Computational Biology*, 14(3):1–26, 3 2018.

[162] Micha Kania, Herv Rix, Magorzata Fereniec, Heriberto Zavala-Fernandez, Dariusz Janusek, Tomasz Mroczka, Gnter Stix, and Roman Maniewski. The effect of precordial lead displacement on ECG morphology. *Medical and Biological Engineering and Computing*, 52(2):109–119, 2014.

[163] David M. Corey, William P. Dunlap, and Michael J. Burke. Averaging Correlations: Expected Values and Bias in Combined Pearson r s and Fisher's z Transformations. *The Journal of General Psychology*, 125(3):245–261, 7 1998.

[164] Ana Mincholé, Ernesto Zacur, Rina Ariga, Vicente Grau, and Blanca Rodriguez. MRI-Based Computational Torso/Biventricular Multiscale Models to Investigate the Impact of Anatomical Variability on the ECG QRS Com-

plex. *Frontiers in Physiology*, 10(August), 2019.

[165] Yksel Özbay, Rahime Ceylan, and Bekir Karlik. A fuzzy clustering neural network architecture for classification of ECG arrhythmias. *Computers in Biology and Medicine*, 36(4):376–388, 2006.

[166] Martino Alessandrini, Bidisha Chakraborty, Brecht Heyde, Olivier Bernard, Mathieu De Craene, Maxime Sermesant, and Jan D'Hooge. Realistic Vendor-Specific Synthetic Ultrasound Data for Quality Assurance of 2-D Speckle Tracking Echocardiography: Simulation Pipeline and Open Access Database. *IEEE Transactions on Ultrasonics, Ferroelectrics, and Frequency Control*, 65(3):411–422, 2018.

[167] S. Rapaka, T. Mansi, B. Georgescu, M. Pop, G. A. Wright, A. Kamen, and Dorin Comaniciu. LBM-EP: Lattice-boltzmann method for fast cardiac electrophysiology simulation from 3D images. *Lecture Notes in Computer Science (including subseries Lecture Notes in Artificial Intelligence and Lecture Notes in Bioinformatics)*, 7511 LNCS:33–40, 2012.

[168] Eric Lluch, Ruben Doste, Sophie Giffard-Roisin, Alexandre This, Maxime Sermesant, Oscar Camara, Mathieu De Craene, and Hernan G. Morales. Smoothed particle hydrodynamics for electrophysiological modeling: An alternative to finite element methods. *Lecture Notes in Computer Science (including subseries Lecture Notes in Artificial Intelligence and Lecture Notes in Bioinformatics)*, 10263 LNCS:333–343, 2017.

[169] Ting Yang, Long Yu, Qi Jin, Liqun Wu, and Bin He. Localization of Origins of Premature Ventricular Contraction by Means of Convolutional Neural Network from 12-lead ECG. *IEEE Transactions on Biomedical Engineering*, 9294(c), 2017.

[170] Fabian Pedregosa, Vincent Michel, Olivier Grisel, Mathieu Blondel, Peter Prettenhofer, Ron Weiss, Jake Vanderplas, David Cournapeau, Fabian Pedregosa, Gal Varoquaux, Alexandre Gramfort, Bertrand Thirion, Olivier Grisel, Vincent Dubourg, Alexandre Passos, Matthieu Brucher, Matthieu Perrot, and Edouard Duchesnay. Scikit-learn: Machine Learning in Python. *Journal of Machine Learning Research*, 12:2825–2830, 2011.

[171] Lars Buitinck, Gilles Louppe, Mathieu Blondel, Fabian Pedregosa, Andreas Mueller, Olivier Grisel, Vlad Niculae, Peter Prettenhofer, Alexandre Gramfort, Jaques Grobler, Robert Layton, Jake Vanderplas, Arnaud Joly, Brian Holt, and Gal Varoquaux. API design for machine learning software: experiences from the scikit-learn project. 9 2013.

[172] Tin Kam Ho. The random subspace method for constructing decision forests. *IEEE Transactions on Pattern Analysis and Machine Intelligence*, 20(8):832–844, 1998.

[173] Trevor Hastie, Robert Tibshirani, and Jerome Friedman. The Elements of Statistical Learning. *Springer Series in Statistics*, 2009.

[174] Emina Alickovic and Abdulhamit Subasi. Medical Decision Support System for Diagnosis of Heart Arrhythmia using DWT and Random Forests

Classifier. *J Med Syst*, 40(4):108, 2016.

[175] Krzysztof Gajowniczek, Iga Grzegorczyk, and Tomasz Z\k abkowski. Reducing False Arrhythmia Alarms Using Different Methods of Probability and Class Assignment in Random Forest Learning Methods. *Sensors (Basel)*, 19(7), 2019.

[176] Max Gordon and Cranos Williams. PVC Detection Using a Convolutional Autoencoder and Random Forest Classifier. *Pac Symp Biocomput*, 24:42–53, 2019.

[177] Pasquale Vergara, Wendy S Tzou, Roderick Tung, Chiara Brombin, Alessandro Nonis, Marmar Vaseghi, David S Frankel, Luigi Di Biase, Usha Tedrow, Nilesh Mathuria, Shiro Nakahara, Venkat Tholakanahalli, T Jared Bunch, J Peter Weiss, Timm Dickfeld, Dhanunjaya Lakireddy, J David Burkhardt, Pasquale Santangeli, David Callans, Andrea Natale, Francis Marchlinski, William G Stevenson, Kalyanam Shivkumar, William H Sauer, and Paolo Della Bella. Predictive Score for Identifying Survival and Recurrence Risk Profiles in Patients Undergoing Ventricular Tachycardia Ablation. *Circ Arrhythm Electrophysiol*, 11(12):e006730, 2018.

[178] Qiao Li, Cadathur Rajagopalan, and Gari D Clifford. Ventricular fibrillation and tachycardia classification using a machine learning approach. *IEEE Trans Biomed Eng*, 61(6):1607–1613, 6 2014.

[179] Xiaochen Tang, Ziwei Ma, Qisong Hu, and Wei Tang. A Real-time Arrhythmia Heartbeats Classification Algorithm using Parallel Delta Modulations and Rotated Linear-Kernel Support Vector Machines. *IEEE Trans Biomed Eng*, 7 2019.

[180] Rocio Cabrera Lozoya, Benjamin Berte, Hubert Cochet, Pierre Jais, Nicholas Ayache, and Maxime Sermesant. Model-Based Feature Augmentation for Cardiac Ablation Target Learning From Images. *IEEE Trans Biomed Eng*, 66(1):30–40, 2019.

[181] Qin Qin, Jianqing Li, Li Zhang, Yinggao Yue, and Chengyu Liu. Combining Low-dimensional Wavelet Features and Support Vector Machine for Arrhythmia Beat Classification. *Sci Rep*, 7(1):6067, 2017.

[182] Teuvo Kohonen. Self-Organized Formation of Topologically Correct Feature Maps. *Biological Cybernetics*, 69:59–69, 1982.

[183] Alfredo Rosado-Muñoz, Jose M Martinez-Martinez, Pablo Escandell-Montero, and Emilio Soria-Olivas. Visual data mining with self-organising maps for ventricular fibrillation analysis. *Comput Methods Programs Biomed*, 111(2):269–279, 2013.

[184] M L Talbi and A Charef. PVC discrimination using the QRS power spectrum and self-organizing maps. *Comput Methods Programs Biomed*, 94(3):223–231, 6 2009.

[185] Hiroyuki Kinoshita, Makoto Yoshizawa, Masashi Inagaki, Kazunori Uemura, Masaru Sugimachi, and Kenji Sunagawa. Development of an algorithm for detection of fatal cardiac arrhythmia for implantable cardioverter-defibrillator

using a self-organizing map. *Conf Proc IEEE Eng Med Biol Soc*, 1:4370–4373, 2006.

[186] Henry Okola Nyongesa Birgitta Dresp-Langley John Mwangi Wandeto, Birgitta Dresp-langley, John Mwangi Wandeto, and Henry Okola Nyongesa. Using the quantization error from Self Organizing Map (SOM) output for fast detection of critical variations in image time series. *From Data to Decision*, 2(Issue 1):1–32, 2018.

[187] Sergio Sanchez-Martinez, Nicolas Duchateau, Tamas Erdei, Alan G. Fraser, Bart H. Bijnens, and Gemma Piella. Characterization of myocardial motion patterns by unsupervised multiple kernel learning. *Medical Image Analysis*, 35:70–82, 2017.

[188] Sima Soheilykhah, Ali Sheikhani, Alireza Ghorbani Sharif, and Mohammad M. Daevaeiha. Localization of premature ventricular contraction foci in normal individuals based on multichannel electrocardiogram signals processing. *SpringerPlus*, 2(1):1–7, 2013.

[189] Irvin Teh, Darryl McClymont, Rebecca A. B. Burton, Mahon L. Maguire, Hannah J. Whittington, Craig A. Lygate, Peter Kohl, and Jrgen E. Schneider. Resolving Fine Cardiac Structures in Rats with High-Resolution Diffusion Tensor Imaging. *Scientific Reports*, 6(April):30573, 2016.

Curriculum Vitae

Rubén Doste Beltrán received his B.Sc. degree in Physics from the University of Barcelona in 2012 and his M.Sc. degree in Biomedical Engineering from the University of Barcelona and the Polytechnic University of Catalonia in 2014. He joined PhySense research group (Universitat Pompeu Fabra) and started his Ph.D. under the supervision of Dr. Oscar Camara and Dr. Rafael Sebastian in 2015. His work is focused on the development of personalized computational models for the *in silico* study of new strategies for ablation of ventricular tachycardia, integrating richer multimodal data in the simulations.

Publications

Journal papers

1. **Doste, R.**, Sebastian, R., Gomez, J.F., et al. In silico pace-mapping: prediction of left vs right outflow tract origin in idiopathic ventricular arrhythmias with patient-specific electrophysiological simulations. [Submitted].
2. **Doste, R.**, Soto-Iglesias, D., Bernardino, G., et al. A rulebased method to model myocardial fiber orientation in cardiac biventricular geometries with outflow tracts. Int J Numer Meth Biomed Engng. 2019; 35:e3185.
3. Santiago, A., Aguado-Sierra, J., Zavala-Ake, M., **Doste, R.**, et al. Fully coupled fluidelectromechanical model of the human heart for supercomputers. Int J Numer Meth Biomed Engng. 2018; 34:e3140.

Peer-reviewed conference papers

1. **R Doste**, M Lozano, JF Gomez, A Alcaine, L Mont, A Berruezo, O Camara, R Sebastian, Predicting the Origin of Outflow Tract Ventricular Arrhythmias Using Machine Learning Techniques Trained with Patient-Specific Electrophysiological Simulations. Proceedings of the XLVI International Conference on Computing in Cardiology. Singapore, 2019
2. Sacco F., **Doste, R.**, Bederian, C., Iles, T.L., Paul, P.I., Houzeaux, G., Vazquez, M., Camara, O., Butakoff, C., Aguado-Sierra J. The effect of gender and endocardial detail on biventricular anatomically normal human heart electrophysiology. CompBioMed Conference 2019
3. Nuñez-Garcia M., Bernardino G., **Doste R.**, Zhao J., Camara O., Butakoff C. Standard Quasi-Conformal Flattening of the Right and Left Atria. In: Coudire Y., Ozenne V., Vigmond E., Zemzemi N. (eds) Functional Imaging and Modeling of the Heart. FIMH 2019. Lecture Notes in Computer Science, vol 11504. Springer, Cham

4. Lluch E. **Doste R**, Giffard-Rosisin S, et al. (2017) Smoothed Particle Hydrodynamics for Electrophysiological Modeling: An Alternative to Finite Element Methods. In: Pop M., Wright G. (eds) Functional Imaging and Modelling of the Heart. FIMH 2017. Lecture Notes in Computer Science, vol 10263. Springer, Cham
5. **Doste R**. et al. (2017) A Rule-Based Method to Model Myocardial Fiber Orientation for Simulating Ventricular Outflow Tract Arrhythmias. In: Pop M., Wright G. (eds) Functional Imaging and Modelling of the Heart. FIMH 2017. Lecture Notes in Computer Science, vol 10263. Springer, Cham
6. **Doste, R.**, Soto-Iglesias, D., Bernardino, G., et al. A rule-based method to model myocardial fiber orientation in cardiac biventricular geometries including the outflow tracts. Proceedings of the 5th International Conference on Mathematical and Computational Biomedical Engineering (CMBE), P. Nithiarasu and A.Robertson (Eds.), Pittsburgh, US, 2017.

Conference abstracts

1. **Doste, R.**, Sacco, F., Iazzo, P.A., Iles, T.L., Butakoff, C., Aguado-Sierra J., Camara, O. A rule based method for assigning fiber information to heart complex structures. Proceedings of the VPH Conference, Zaragoza, Spain, 2018
2. Sacco F., **Doste, R.**, Calmet, H., Iles, T.L., Iazzo, P.A., Houzeaux, G., Vazquez, M., Camara, O., Butakoff, C., Aguado-Sierra J. Electrophysiology simulations of female and male human ventricles: influence of gender phenotype and endocardial anatomy on signal propagation Biophysical Society 2018
3. **R Doste**, D Soto-Iglesias, A Alcaine, S Giffard-Roisin, M Sermesant, A Berruezo, O Camara, P457 Prediction of the site of origin in outflow tract ventricular arrhythmias with electrophysiological simulations, EP Europace, Volume 20, Issue suppl_1, March 2018, Page i90
4. **Doste, R.**, et al. "Non-invasive virtual prediction of site of origin in outflow tract ventricular arrhythmias with a patient-specific computational model." European Heart Journal. Vol. 38. Great Claredon St, Oxford OX2 6DP, England: Oxford Univ Press, 2017.